Title
Miniature Ion Thruster Characterization via Discharge Plasma, Plume, and Mission Analyses

Author
Samples, Stephen Anthony

Publication Date
2021

Peer reviewed|Thesis/dissertation

UNIVERSITY OF CALIFORNIA

Los Angeles

Miniature Ion Thruster Characterization via Discharge Plasma, Plume, and Mission Analyses

A dissertation submitted in partial satisfaction
of the requirements for the degree
Doctor of Philosophy in Aerospace Engineering

by

Stephen Anthony Samples

2021

ABSTRACT OF THE DISSERTATION

Miniature Ion Thruster Characterization via Discharge Plasma, Plume, and Mission Analyses

by

Stephen Anthony Samples
Doctor of Philosophy in Aerospace Engineering
University of California, Los Angeles, 2021
Professor Richard E. Wirz, Chair

The Miniature Xenon Ion (MiXI) thruster is a 3 cm DC ion thruster developed as low-power, high efficiency micro-propulsion. This work focuses on the further development of the MiXI thruster into a viable propulsion technology and investigates the capabilities of MiXI as primary propulsion on CubeSat missions. First, we set the stage for this work by investigating the viability of high ΔV small spacecraft missions with high efficiency, high impulse propulsion, and explore the sensitivities of mission capabilities to thruster properties and performance. One important conclusion is that in the CubeSat form-factor, high impulse micropropulsion enables high ΔV missions of several km/s with payloads of multiple U volume and multiple kg mass, however these parameters are very sensitive to thruster parameters such as I_{sp}, total efficiency, and neutralizer cathode performance. An ion thruster model is then developed to investigate key aspects of miniature DC ion thruster discharge and thruster performance using simplified descriptions of the plasma behavior to explore a wide range of the thruster design space. Results from this model provide clear boundaries to miniature ion thruster performance while also providing clear pathways for effectively im-

proving thruster design for increased mission capabilities. The results from the model guide an experimental effort to experimentally investigate the 3-ring and Axial Ring-Cusp Hybrid (ARCH) discharge designs for the MiXI thruster. A small plume diagnostics suite consisting of Faraday, emissive, and ExB probes was developed and used to probe the MiXI(ARCH) plume. While no doubly charged ions were detected in the beam at the operating point measured, measurements agree with prior computational work and show a beam flatness of 0.6, divergence of 5°, and plume potential of 4.5 V. Later, MiXI(ARCH) was operated with a miniature discharge hollow cathode. Finally, using lessons learned from cathode integration, computational, and analytical modeling, a refined miniature hollow cathode design was developed to further improve discharge and thruster efficiency. Through experimental and analytical investigation, mission studies, and further development of critical aspects of the thruster, this work shows that the MiXI thruster is an attractive propulsion option for high efficiency, high specific impulse micropropulsion.

The dissertation of Stephen Anthony Samples is approved.

Rohit Shastry

Dan M. Goebel

Artur R. Davoyan

Troy A. Carter

Ann R. Karagozian

Richard E. Wirz, Committee Chair

University of California, Los Angeles

2021

TABLE OF CONTENTS

List of Figures

List of Tables

ACKNOWLEDGMENTS

Throughout my graduate career, I have received support from a variety of people in ways both personal and professional. I would like to thank NASA's NSTRF program for funding my graduate career, and giving me the freedom to pursue the research I was most interested in. I would like to thank my graduate advisor, Professor Richard Wirz, for guiding me throughout the entire process, and who helped me to focus my thinking onto the first-principles physics of my work. Advice from others, including Dr. Rohit Shastry and Professor Dan Goebel has also been invaluable. My fellow UCLA PSPL students have been a constant source of entertainment, advice, rubber ducky talks, and camaraderie the six years I have been a part of the group. My Mother, Father, and siblings made me into who I am today, and ensured that I was given the best possible chance to succeed. And Chelsea, who has gone through the last decade with me, and has helped me in so many ways: proofreading my terrible writing, distracting me with adventures when I'm having difficult times, listening to me and helping me practice talks, interviews, and more, and supporting and loving me throughout.

VITA

2012 - 2015	Engineering Intern, United Launch Alliance. Interned summers of 2012 - 2015 at ULA in the Factory Support, Advanced Programs, Propulsion Components, and Trajectory and Performance groups.
2014	B.S. (Aerospace Engineering), Auburn University.
2015	Advanced Propulsion Intern, NASA Marshall Space Flight Center, Spring 2015.
2015 - 2017	Research Assistant, UCLA Plasma and Space Propulsion Lab, UCLA.
2017 - 2020	Teaching Assistant Winter 2017 and Course Administrator Summer 2020, MAE 161B Intro to Space Technology.
2017	M.S. (Aerospace Engineering), UCLA.
2017 - 2021	NSTRF Fellow, UCLA Plasma and Space Propulsion Lab, UCLA. Spent summers of 2018 at NASA Glenn and 2019 at JPL as an NSTRF Visiting Technologist.

PUBLICATIONS

Parametric Analysis of High Delta-V CubeSat Missions with a Miniature Ion Thruster. Stephen Samples and Richard Wirz, Journal of Spacecraft and Rockets 2021 58:3, 754-763

Comment on 'Jet propulsion by microwave air plasma in the atmosphere'. Peter Wright, Stephen Samples, Nolan Uchizono, and Richard Wirz. AIP Advances 10, 099101 (2020)

Tunable reflectionless absorption of electromagnetic waves in a plasma-metamaterial composite structure. Nolan Uchizono, Stephen Samples, and Richard Wirz. 2020 Plasma Sources Sci. Technol. 29 085009

Development of the MiXI Thruster with the ARCH Discharge. Stephen Samples and Richard Wirz. 2020 Plasma Res. Express 2 025008

CHAPTER 1

Introduction

1.1 Space Travel and Electric Propulsion

Rockets eject propellant at high velocities to generate thrust for spacecraft orbital maneuvers, attitude control, and more. The initial momentum of a spacecraft of mass m and its differential unit of propellant mass dm is the total mass times the initial velocity V. The final momentum of the system after propellant ejection is the mass of the spacecraft times the new velocity $V + dV$, and the ejected propellant mass times the ejection velocity in the lab frame $V - v_e$. Momentum in these two instances is constant:

$$(m + dm)V = m(V + dV) + dm(V - v_e) \tag{1.1}$$

Rearranging and integrating, this results in the Tsiolkovsky Rocket Equation:

$$\Delta V = v_e ln \frac{m_i}{m_f} \tag{1.2}$$

The change in velocity, or ΔV, of a burn with some initial mass m_i and final mass m_f is directly proportional to the exhaust velocity v_e of the propellant. By increasing the exhaust velocity of a particular maneuver, one may either increase the possible ΔV with the given propellant, or decrease the mass fraction m_i/m_f. I_{sp} is commonly referred to instead of exhaust velocity, which in a steady-state system is simply the exhaust velocity divided by standard gravitational acceleration or $I_{sp} = v_e/g$. Decreasing the mass fraction corresponds

to either decreasing the propellant and thus wet mass for a given payload, or increasing the payload mass for a given propellant mass.

There are several propulsion technologies which operate on the principle of rocket propulsion, which can largely be divided into two categories: chemical and electric propulsion (EP). Chemical propulsion generates a high pressure gas to accelerate through a nozzle by increasing temperature through combustion. The energy for chemical propulsion ultimately comes from chemical bonds within the propellant itself. Because the energy to accelerate the propellant is stored within the propellant itself, it is straightforward to increase the power of the engine by increasing mass flow. The specific power which drives exhaust velocity, however, is limited to that of the available chemical bonds within the propellant and can only be altered by changing propellants, and has an upper limit of around 500 s. As such, chemical propulsion is often said to be high thrust, low I_{sp} propulsion.

Electric propulsion, conversely, is typically higher I_{sp} but lower thrust than chemical propulsion. There is a large variety of electric propulsion sub-technologies, but the connecting thread is that they all impart energy into the propellant through electrical power rather than chemical. As such, the energy going into the propellant is decoupled from the chemical properties of the propellant, and is instead dependent on the spacecraft power system. Specific power input into the power system is readily altered, allowing for variable and high I_{sp}, but increasing power through increasing mass flow rate quickly reaches the upper limit of what modern power systems can deliver.

Figure 1.1 illustrates the benefit of electric propulsion for high impulse missions, showing the calculated propellant fraction required for different I_{sp} and ΔV values. The knee in the curve is the region where increasing gains in I_{sp} result in diminishing returns of decreased propellant mass, and this knee is at higher I_{sp} for higher impulse missions. For example, an 8 km/s burn requires a propellant mass fraction of 25 with 250 s I_{sp}, but only 0.31 with 3000 s. While electric propulsion is unable to provide the thrust required to launch vehicles into space from the surface of the Earth, in applications such as station keeping, in-space

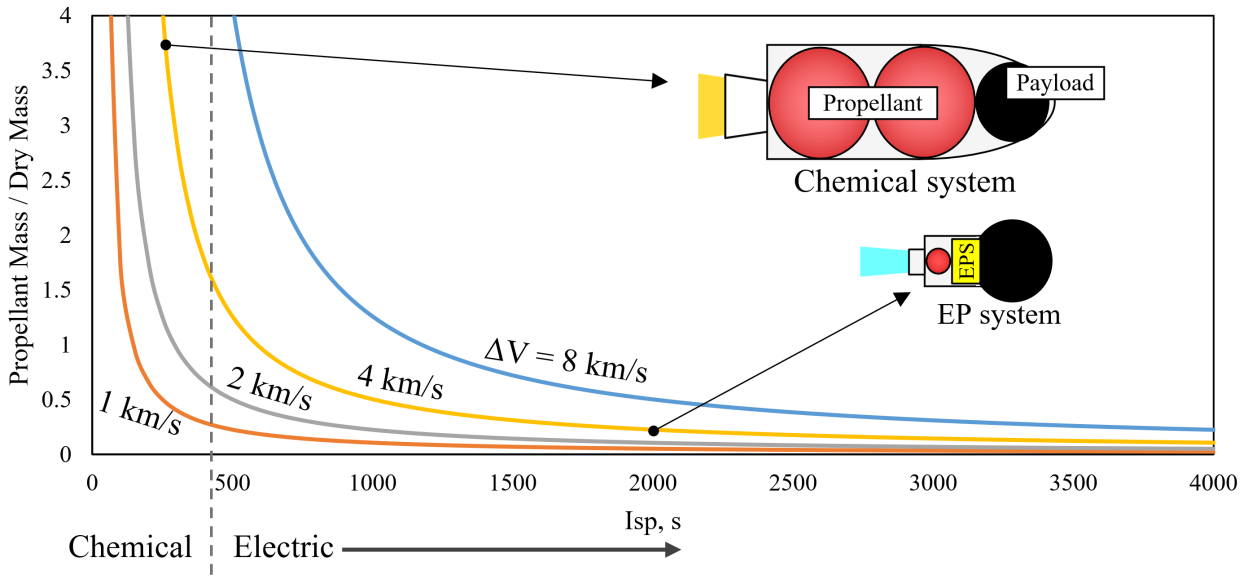

Figure 1.1: Propellant mass fraction as a function of required ΔV and thruster I_{sp}. Chemical propulsion systems with lower I_{sp} require significantly more propellant for the same mission than typical electric thrusters.

transfers, drag reduction, and attitude control where low thrust is permissible, EP provides significant propellant mass reduction. Due to the low thrust of EP, it requires long duration burns, whereas chemical propulsion is typically short duration and said to be "impulsive". For the same , chemical propulsion will have much shorter burn duration, and EP will have significantly reduced propellant requirements.

1.2 Ion Thrusters

Gridded Ion Engines, otherwise known as Ion Thrusters, are one type of EP which use high velocity ions to produce thrust. They are differentiated from other forms of electric propulsion through the use of a series of grids for propellant acceleration, clearly seen in Figure 1.2. A schematic detailing the operation and major components of ion thrusters is given in Figure 1.3. Propellant is injected into the discharge chamber through injection sites and the discharge cathode, creating a large neutral population. The discharge cathode

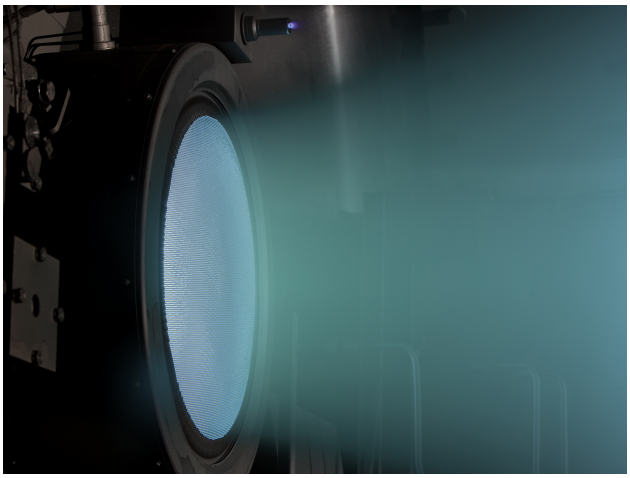

Figure 1.2: NASA's Evolutionary Xenon Thruster (NEXT) used on the Double Asteroid Redirect Test (DART) mission. [NASA]

provides a source of high energy primary electrons, which are electrically attracted to the anode and travel through the neutral gas across the discharge chamber. Magnetic fields mirror the particles and reflect primaries from the anode. These primary electrons bounce around the discharge chamber ionizing neutrals, generating a plasma which then may also further generate ions through ionization collisions between plasma electrons and neutrals. The resultant plasma is a combination of electrons and ionized propellant atoms, and is confined by the magnetic field lines blocking electrons' path to the anode. The discharge is sustained by the discharge power supply, and contained between the anode and the ion optic grids. To produce thrust, the entire plasma is biased up to beam potential on the order of 400-4000 V by a beam power supply, and the plasma ions are accelerated into ion beams by the ion optic grids. These grids repel electrons both within and without the discharge to keep them segregated between the discharge and space, and use electric fields to accelerate and focus the ion beams. The velocity of the resultant ion beam is readily ascertained through conservation of energy between electrical potential and kinetic energy:

$$v_e = \sqrt{\frac{2q\phi}{M}} \tag{1.3}$$

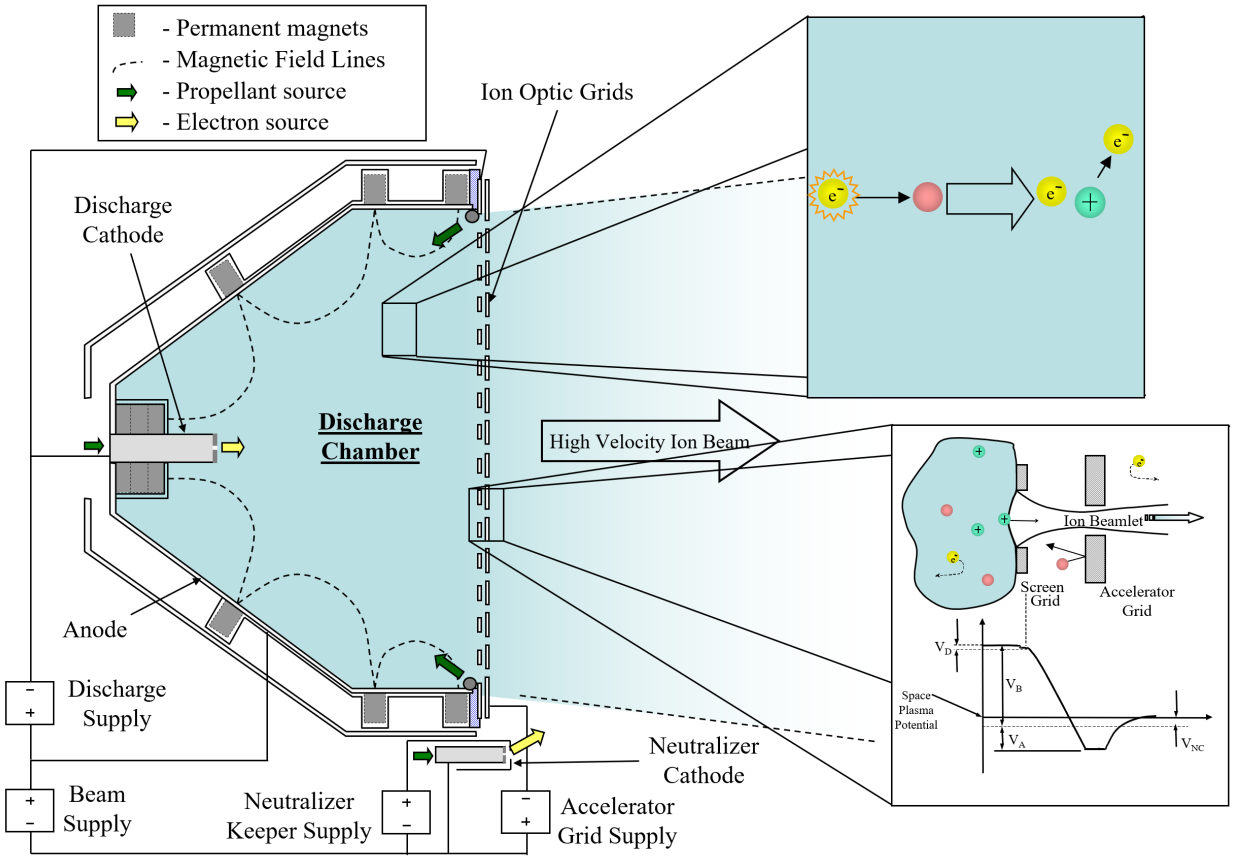

Figure 1.3: Ion thruster operational schematic from Wirz [1].

The velocity of propellant v_e in an ion thruster is simply a function of ion properties such as mass M, charge q and the accelerating voltage ϕ. The thrust, I_{sp}, and specific power of the thruster is as such decoupled from the chemical energy within propellant bonds, and electrical power rather than chemical power is used to propel the ions. Because the beam consists of only ions, there is a net current away from the thruster. To prevent spacecraft charging and to complete the circuit with the beam power supply, a neutralizer cathode is used. Similar to the discharge cathode, this cathode provides electrons to space (or a vacuum chamber) to balance the current coming from the ion thruster and to maintain a low potential between spacecraft ground and space. To prevent electrons travelling from the neutralizer or space through the optics into the discharge chamber and creating spurious beam current, an accelerator grid is located on the outside of the optics and is biased negatively relative to

space potential in order to repel electrons.

1.2.1 Miniature Ion Engines

The Miniature Xenon Ion Thruster was first reported in 2001 [7] as a testbed for evaluating discharge magnetic field configurations in a 3 cm diameter form factor. From 2000 to 2005 the original "MiXI" with the 3-Ring discharge topology [8], shown in Figure 1.4, was developed and demonstrated with beam extraction and shown to have high efficiency at 72% propellant efficiency and 444 W/A using filament cathodes and neglecting heater losses. This performance estimate was based on the behavior of conventionally-sized ion thrusters (25 cm and above) where hollow cathodes are self-heated and require negligible power. For a discussion on ion thruster performance parameters see Section 2.1. A computational plasma code, DC-ION, was also developed to investigate internal plasma processes. [9, 10, 11, 12, 13, 5, 14] In 2018 Dankongkakul and Wirz developed the Axial Ring-Cusp Hybrid (ARCH) discharge, a unique discharge which combined elements of Kaufman [15], ring-cusp, and electrostatic discharges [16] to obtain a discharge loss of 180 W/A and propellant utilization of 82% with simulated beam extraction, filament cathodes, and cathode losses neglected [17]. Figure 1.5 details the two discharges. MiXI(3-Ring) has three ring-cusps with anode-potential cusp terminations providing confinement of the plasma, whereas MiXI(ARCH) has two ring-cusps at the rear of the discharge with cathode-potential cusp terminations, and a near-axial magnetic field at the anode. Computational modeling and experimental investigation suggest that the efficiency increase ARCH sees over the original 3-ring discharge is due to increased confinement of primary electrons [5, 17]. The work presented here picks up after the development of the ARCH discharge.

Figure 1.4: The original MiXI(3-Ring) thruster.

1.2.2 Miniature Hollow Cathodes and Electron Sources

Hollow cathodes are electron sources which, similarly to filament cathodes, rely on thermionic emission of electrons to sustain a plasma discharge. A diagram of a typical cathode is given in Figure 1.6. Hollow cathodes commonly consist of four main components: a tubular body which houses the emitter and provides mechanical and electrical connection to the spacecraft, a low work function material to serve as electron emitter called the insert, an orifice, and a heater. The aspect ratio of cathode orifices varies, ranging from extremely high aspect ratio orifices which greatly restrict gas flow, to low aspect ratios which are simply open tubes. The electrical connection to the cathode body (electrically connected to the insert) is called cathode common, which provides electrons to the cathode, which supplies these electrons to the plasma via the electron-emitting insert. There are three main electrodes in a hollow cathode discharge, the cathode body, a keeper, and an anode. The keeper is positively biased relative to the cathode stem, ignites the initial cathode discharge and pulls enough current to heat the cathode and sustain the plasma when the anode is not pulling enough current.

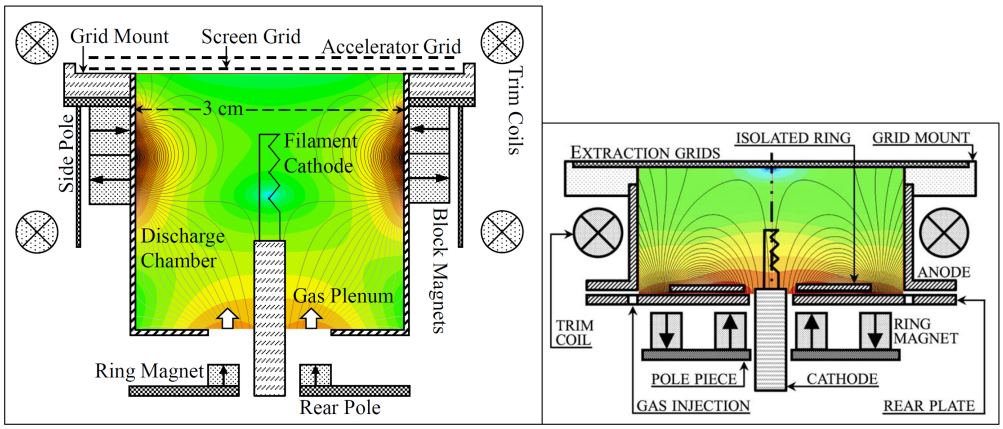

Figure 1.5: The 3-Ring and ARCH MiXI discharges.

When both the keeper and anode are pulling current, it is said to be in triode mode. When the anode pulls enough current that the keeper discharge is unnecessary, the cathode is said to be in diode mode.

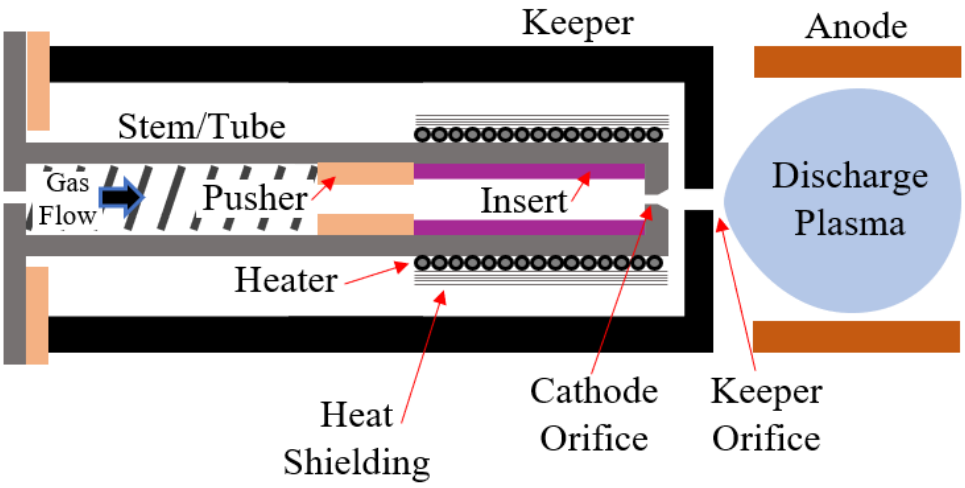

Figure 1.6: A typical hollow cathode.

There are a few miniature hollow cathodes in the literature at the current and power levels required for the MiXI thruster. Domonkos in 1999 [18] performed a study measuring the operating properties of several miniature hollow cathode designs, with different orifice diameters and spacings. After this parametric study, a new miniature cathode was designed

to incorporate lessons learned. Domonkos's SC.012 cathode was designed for 100 - 300 W Hall-effect thrusters, and featured a 0.13 mm diameter by 0.5 mm long orifice, and open keeper with 2.3 mm orifice diameter. At 1.5 A discharge current, the cathode operated stably down to 0.6 sccm, and at 0.5 A the cathode operated down to 1 sccm. Puchkov in 2017 developed a small cathode which operates between 0.15 - 0.8 sccm and 0 - 0.3 A with under 10 W keeper power [19]. This cathode was a Type C cathode due to its low current density at the orifice, and employed a vacuum gap between the emitter and stem to increase thermal isolation. Both of these cathodes had barium oxide inserts, which are common in small cathodes due to its low work function. Recent miniature cathodes have also utilized LaB6 inserts, which trades higher temperature operation for a more chemically robust insert. The MaSMi hollow cathode assembly utilizes a small LaB6 insert for operation down to 1 A discharge current and 1 sccm flow, and was demonstrated to successfully operate over 25,000 heaterless ignition cycles by Becatti et al [20]. The SITAEL HC1 low-current cathode[21] is designed to operate between 0.3 - 1 A and 0.8 - 2 sccm xenon, and has been demonstrated at 1 sccm and 1 A coupled with the HT100 hall-effect thruster.

1.3 Dissertation Motivations and Overview

There are a number of miniature (<1 kW) electric propulsion options, including Field-Emission Electric Propulsion (FEEP) and mini Radio-Frequency (RF) ion engines, but none match the high efficiency capabilities of larger scale DC ion thrusters. Previous development of MiXI and the ARCH discharge indicated that large-scale efficiencies may be possible for micro-EP, but high-efficiency miniature DC ion thrusters have not been matured past TRL 3-4. To improve the feasibility of high impulse, small-scale missions, this research focuses on further determination of the expected in-flight performance of MiXI, and developing the technologies needed for flight.

These dissertation objectives are influenced by a NASA Space Technology Research Fel-

lowship for the development of MiXI. Chapter 2 presents a basic overview of ion thruster performance calculations which are used in later sections, and the outline of an analytical model used for ARCH discharge modeling. In Chapter 3, a mission study is performed using performance numbers from the filament characterization. Here mission sensitivities to MiXI performance and neutralizer properties are investigated, which inform further cathode development. In Chapter 4, MiXI with the ARCH discharge and filament cathodes is characterized, and the analytical model is used to investigate the data. Miniature hollow cathodes are also integrated with the MiXI thruster, and undergo initial characterization. Chapter 6 covers efforts to develop improved cathodes for the MiXI thruster. Finally, Chapter 5 covers the development and verification of a small plume diagnostics package for future MiXI testing.

CHAPTER 2

Miniature DC Ion Thruster Plasma Discharge Theory

This chapter begins with a discussion of the major ion thruster performance parameters, including both direct measurements using voltages and currents, and indirect measurements using plume diagnostics. Then, a simple single-cell ion thruster discharge model to predict thruster performance is introduced and the relevant major physics are outlined. Finally, the major performance parameters for an E×B probe, to be used for MiXI plume diagnostics, are derived.

2.1 Ion Thruster Performance

Propellant utilization, η_p, is the fraction of propellant atoms which are ejected as beam ions, as opposed to escaping through the grids as neutral atoms. Discharge loss, ε_B, is the discharge power required to generate one amp of beam current I_b (or equivalently the energy needed to ionize one beam atom). These are given as:

$$\eta_p = \frac{I_b}{e\dot{m}_o/M_i + I_b} \tag{2.1}$$

$$\varepsilon_B = \frac{P_d}{I_b} = \frac{V_d I_d + V_s I_s + V_{bp} I_{bp} + V_a I_a}{I_b} \tag{2.2}$$

Where $\dot{m}_o$ is the neutral flux through the grids, e is the electron charge, I_d is discharge current, I_{bp} is backplate current, I_s is the screen grid current, and I_a is accelerator grid

current. V is the voltage of the corresponding supplies for each of the electrodes. Propellant utilization is affected by two main factors: ion flux and neutral flux through the extraction plane and out of the discharge. Ion flux through the grids is described by the grid ion optics and plasma diffusion in the region just upstream of the grid plane. The flow of neutrals escaping the discharge is estimated by thermal flux through the grids Γ_o over some grid area A_g with neutral transparency T_a and Clausing factor η_c:

$$Q = \Gamma_o A_g \Phi_o = \frac{n_o v_o}{4} A_g T_a \eta_c \tag{2.3}$$

The mean particle speed, v_o, is a function of temperature such that:

$$Q = \frac{n_o \sqrt{8kT_o}}{4\sqrt{M\pi}} A_g T_a \eta_c \propto \sqrt{T} \tag{2.4}$$

n_o and T_o are the neutral density and temperature, M is the neutral particle mass, and k is Boltzmann's constant. Equation 2.4 indicates that the neutral flux is proportional to the square root of neutral temperature. The electrical efficiency of the discharge, η_e, is the ratio of beam power to total power (in the case of filament cathodes, the filament heater power is neglected as future cathodes are assumed to be self-heated):

$$\eta_e = \frac{I_b V_b}{\sum P} \tag{2.5}$$

Total efficiency of the thruster η_t is then calculated as:

$$\eta_t = \eta_p \eta_e \gamma^2 \tag{2.6}$$

The value of γ in Equation 2.6 is calculated using the thruster plume's double-ion ratio

and thrust divergence [22]:

$$\gamma = \alpha F_t \tag{2.7}$$

$$\alpha = \frac{1 + .707\frac{I^{++}}{I^{+}}}{1 + \frac{I^{++}}{I^{+}}} \tag{2.8}$$

$$F_t = cos(\theta) \tag{2.9}$$

I^+ and I^{++} are the total current due to singly-charged and doubly-charged ions. θ is the average divergence half-angle of the beam, and is determined as a current-weighted average of the divergence angle at different radial positions in the beam. In the filament study, γ is assumed to be 1 to compare with earlier works [1, 23]. Future characterization will determine the actual value for the MiXI thruster.

2.2 Ideal Ion Thruster Scaling Relations

Initial investigations into the physics of ion thruster discharges can rely on simple assumptions and idealized equations to determine the scaling relations between ion thruster properties and both internal discharge parameters and performance. To gain this analytical understanding of the fundamental trends in ion thruster performance, a simplified, ideal ion thruster model is developed similar to Section 4.2 of [22], but with added simplifications and further scaling analysis.

There are four main loss mechanisms within the discharge of an ideal ion thruster: ionization P^+, excitation P^*, electron current to the anode P_{ea}, and ion current to the grids P_i. Each of these is comprised of some current I and potential U or ε. The first two mechanisms represent energy being dissipated to ionize and excite propellant neutrals. The last

two represent energy being convected from the discharge to the boundaries.

$$P_{loss} = I^+U^+ + I^*U^* + I_{ea}\varepsilon_{ea} + I_i\varepsilon_i \tag{2.10}$$

In an ideal thruster, ions are generated via ionization of neutral gas and then conveyed without loss to the grid extraction plane, $I^+ = I_i = I_{ae}$. Given that energy must be conserved in the system:

$$P_{in} = I^*U^* + I_i(U^+ + \varepsilon_{ea} + \varepsilon_i) \tag{2.11}$$

The excitation rate is product of the chamber volume V, the neutral density n_o, the plasma density n_e, and the excitation reaction rate $\langle\sigma^* v_e\rangle$:

$$I^* = V n_o e n_e \langle\sigma^* v_e\rangle \tag{2.12}$$

The neutral density is given by Eq. 2.25. The ion current to the extraction plane is simply the beam current divided by the grid ion transparency I_b/T_i. The plasma density in Eq. 2.12 can be put in terms of beam current through Eq. 2.26. Plugging these in and dividing by I_b to obtain the discharge loss yields:

$$\varepsilon = \frac{4I_b V U^*}{0.6 T_i T_o v_o A_g^2 e \eta_c} \frac{1-\eta_p}{\eta_p} \frac{\langle\sigma^* v_e\rangle}{\sqrt{kT_e/M}} + \frac{1}{T_i}(U^+ + \varepsilon_{ea} + \varepsilon_i) \tag{2.13}$$

V is the volume of the discharge chamber, T_e is the electron temperature, T_o and v_o are the neutral temperature and velocity, A_g is the grid area, η_c is the grid clausing factor, and η_p is the propellant utilization. Similarly to Equations 2.47 and 2.48, ions leaving the volume drop through the presheath potential $T_e/2$ and the sheath potential ϕ, and electrons hitting

the anode go through an effective potential of $2T_e + \phi$:

$$\varepsilon_{ea} = 2T_e + \phi \tag{2.14}$$

$$\varepsilon_i = 0.5T_e + \phi \tag{2.15}$$

An estimate for the plasma potential can be calculated by noting that the electron current to the anode and the ion current to the grids is equal:

$$I_i = I_{ae} \Rightarrow 0.6en_eA_g\sqrt{kT_e/M} = \frac{1}{4}\sqrt{\frac{8kT_e}{\pi m}}en_eA_ae^{-e\phi/kT_e} \tag{2.16}$$

$$\phi = T_eln\left[1.2\frac{A_a}{A_g}\sqrt{2\frac{M}{\pi m}}\right] \tag{2.17}$$

Plugging these in yields a full equation for the discharge loss of an ideal ion thruster as a function of propellant utilization and electron temperature:

$$\varepsilon = \frac{4I_bVU^*}{0.6A_gT_iT_ov_oA_g^2e\eta_c}\frac{1-\eta_p}{\eta_p}\frac{\langle\sigma^* v_e\rangle}{\sqrt{kT_e/M}} + \frac{U^+}{T_i} + \frac{T_e}{T_i}(2ln\left[1.2\frac{A_a}{A_g}\sqrt{2\frac{M}{\pi m}}\right] + 2.5)) \tag{2.18}$$

T_e cannot be analytically solved for as a function of η_p, however it can be solved computationally to assess trends within the larger equation for ϵ. Knowing that the ion loss to the grids and the ionization rate are equal yields:

$$I_i = I^+ \Rightarrow 0.6en_iA_gv_i = n_on_eVe\langle\sigma^+ v_e\rangle \tag{2.19}$$

Plugging in Equations 2.25 and 2.26 and rearranging:

$$\frac{4I_bV}{0.6A_g^2v_oeT_o\eta_c}\frac{1-\eta_p}{\eta_p} = \frac{\sqrt{kT_e/M}}{\langle\sigma^+v_e\rangle} \tag{2.20}$$

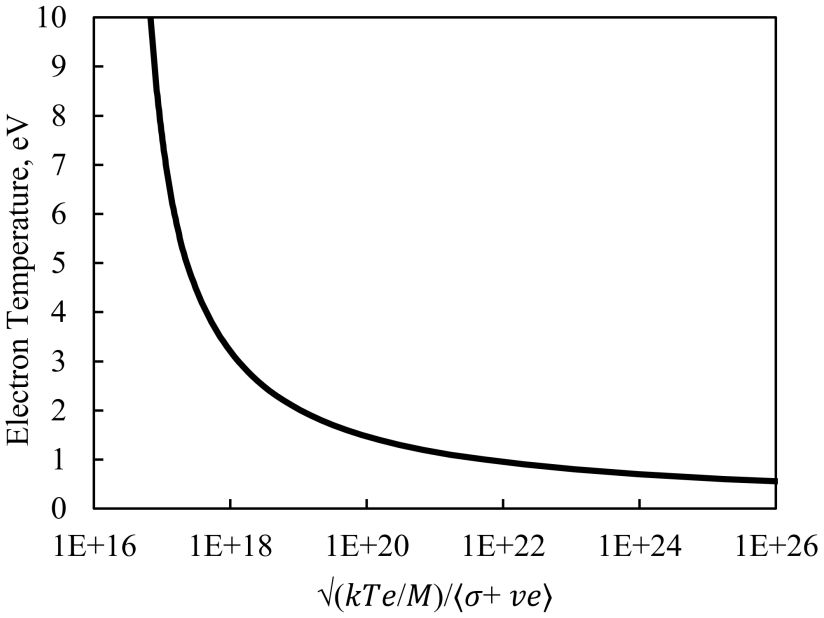

Figure 2.1: Relationship between RHS of Eq. 2.20 and electron temperature.

The RHS of Eq. 2.20 is purely a function of electron temperature and plasma species properties. These can be computed assuming a Maxwellian electron population using fits of Rapp ionization values given in [22] Appendix C, shown in Figure 2.1.

2.3 Non-Ideal Ion Thruster Control Volume Model

While an idealized model is useful for gaining understanding of the fundamental relationships between thruster properties and performance, the assumption of ideal operation make it difficult to apply to a realistic scenario and compare with experimental data. To develop a more physical model, the physics of the ideal ion thruster model are fleshed out to develop a non-ideal analytical ion thruster model. An analytical discharge model similar to that of

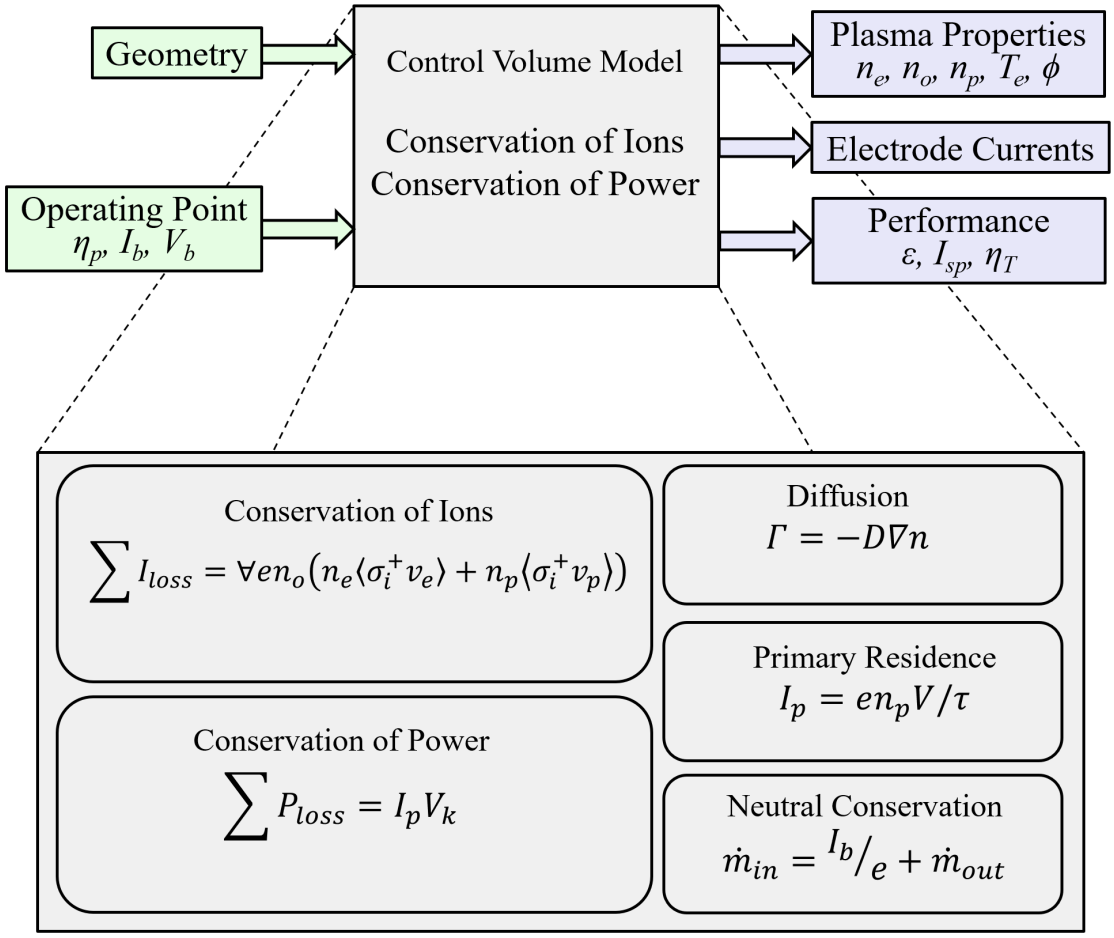

Figure 2.2: Diagram depicting the inputs, outputs, and relevant physics for the analytical ion thruster model.

Goebel, Wirz, and Katz [3] was used to investigate internal loss mechanisms in the thruster and explain the experimentally observed trends. The model simultaneously solves for electron temperature T_e and presheath potential drop ϕ through conservation of ions and power in the discharge. Inputs to the model include thruster geometry, magnetic field strengths, discharge voltage, beam current, and propellant utilization. Outputs include plasma density, plasma temperature, electrode currents, and power losses. These outputs may then be used to calculate thruster performance parameters such as total efficiency and discharge loss. A diagram detailing the major physics, inputs, and outputs is shown in Figure 2.2. This model is differentiated from that of [3] in two ways: the inclusion of cross-field electron diffusion

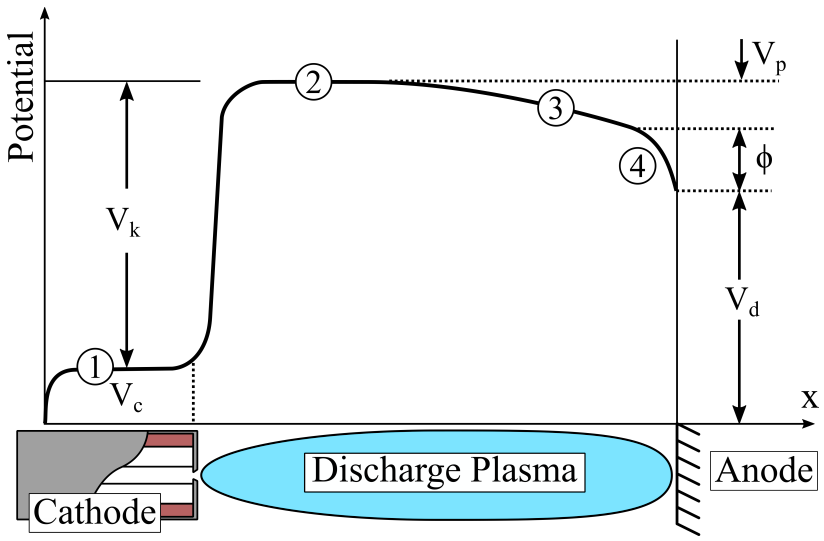

Figure 2.3: Potential in various positions across the thruster, from cathode to anode. There are several regions of interest: 1. Cathode insert plasma, where electrons are emitted from the thermionic surface to generate a dense plasma 2. The bulk plasma, where the bulk of ionization occurs 3. The presheath, which accelerates ions towards the sheath and 4. The plasma wall sheath.

specific to the ARCH geometry and the zero-finding solution method.

Conservation of ions in the discharge requires that the generation rate of ions by primary and plasma ionization be equal to the loss rate of ions to the boundaries. This may be written as some function of the givens, the electron temperature, and the sheath potential:

$$V n_o e(n_e \langle \sigma^+ v_e \rangle + n_p \langle \sigma^+ v_p \rangle) = \sum I_i = f(T_e, \phi) \tag{2.21}$$

V is the is the discharge chamber volume, n_e is plasma density, σ^+ is the ionization crossection, v_e and v_p are the secondary and primary electron velocities, and I_i is some ion loss current. The conservation of power in the discharge requires that the input power to the discharge from primary current I_p be equal to the power dissipated within the plasma and at the boundaries. This may also be written as a function of electron temperature and sheath potential:

$$I_p V_k = \sum P_{loss} = g(T_e, \phi) \tag{2.22}$$

V_k is the primary electron voltage gain, shown in Figure 2.3, and P_{loss} is some power dissipation term. A custom MATLAB function was written which accepts electron temperature and sheath potential as inputs, and outputs the conservation function errors as a vector. This function was then used with the MATLAB "lsqnonlin" optimization tool to solve for ϕ and T_e such that the conservation equations are satisfied:

$$\begin{bmatrix} I_{err} \\ P_{err} \end{bmatrix} = \begin{bmatrix} V n_o e(n_e \langle \sigma_i^+ v_e \rangle + n_p \langle \sigma_i^+ v_p \rangle) - \sum I_i \\ I_p V_k - \sum P_{loss} \end{bmatrix} = f(T_e, \phi) = 0 \tag{2.23}$$

The following sections discuss the relevant equations for solving for the variables within the conservation equations, given some geometry, magnetic field configuration, beam current, propellant utilization, and guess for electron temperature and sheath potential.

2.3.1 Chamber Neutral density

Neutral flux out of the grids in terms of neutral density and temperature is given by Equation 2.3. Neutral flux out of the grids is also related to the propellant utilization and beam current:

$$Q = I_b \frac{1 - \eta_p}{\eta_p} \tag{2.24}$$

After combining Equations 2.3 and 2.24 and rearranging, the neutral density in the chamber is:

$$n_o = \frac{4 I_b}{v_o A_g T_a \eta_c e} \frac{1 - \eta_p}{\eta_p} \tag{2.25}$$

2.3.1.1 Plasma Density

The beam current through the grids is assumed to be one-sided Bohm flux. Rearranging and solving for plasma density similarly to the above derivation for neutral density and solving

for plasma density yields:

$$n_e = \frac{I_b}{0.6\sqrt{\frac{kT_e}{M}}A_g T_s} \tag{2.26}$$

2.3.2 Ion Current

Ion current to the screen grids I_s is calculated using the beam current and grid ion transparency, given the definition of grid transparency of $T_s = I_b/(I_b + I_s)$:

$$I_s = I_b \frac{1 - T_s}{T_s} \tag{2.27}$$

Ion current to the rear plates is calculated assuming Bohm current to a finite loss area with characteristic length of the hybrid leak width [24] $r_{hl} = 4\sqrt{r_{le} r_{li}}$, which is a function of the electron gyroradius r_{le} and ion gyroradius r_{li}. The MiXI(ARCH) geometry results in two cusps at the rear plate, one central point cusp and one ring-cusp. The central loss-area is a circle with a radius equal to the hybrid loss width. The loss-area of the ring-cusp is a planar ring with diameter set by the cusp location and width equal to the hybrid loss width. Depending on the diameter of the central cusp, the loss area may encompass the cathode, keeper, and backplate.

Ion current to the intercusp ring I_{ici} is calculated assuming cross-field ambipolar diffusion identical to [3]:

$$v_i^2 + \frac{el}{\mu_e M}(1 + \mu_e^2 B^2 - \frac{\nu_{ei}}{\nu_e})v_i - \frac{eT_e}{M} = 0 \tag{2.28}$$

Solving for the ion velocity v_i determines the ion current flowing across the magnetic field lines as a function of magnetic field strength B, electron mobility μ_e, electron-ion collision rate ν_{ei}, total electron collision rate ν_e, diffusion length scale l, electron temperature T_e, and ion mass M. Length scales may be assumed to be a characteristic length of the device such as magnet spacing, a folding distance measured from probe data, or an arbitrary value for data-fitting. In this work, the diffusion length scale was assumed to be the chamber radius.

Ion current to the anode is assumed to be gradient-based diffusion with a diffusion coefficient D_{eff} equal to a weighted average of the diffusion coefficients for classical cross-field diffusion of ions, D_i, and electrons D_e. This is used rather than ambipolar diffusion because the ambipolar assumption requires that electron and ion velocities are the same, resulting in no net current flow. Electrons are assumed to be near-Bohm diffusion, resulting in a higher current than ambipolar, and as such the retarding E-field developed during ambipolar diffusion may be altered. Ion and electron classical cross-field diffusion coefficients adequately bound the range of possible values, so a weighted average was used. A value of $D_{eff} = 0.1D_e + 0.9D_i$ was found to qualitatively match data.

2.3.3 Electron Current

Electron current is assumed to be negligible to all cathode-biased surfaces. The intercusp ring is floating, so electron current to the intercusp ring is $I_{ice} = I_{ici}$. Electron current to the anode, I_{ae}, is calculated assuming gradient-based cross-field diffusion with an ionization-based mixing of classical and Bohm coefficients:

$$I_{ae} = (k_{mix}D_b + (1 - k_{mix})D_c)\nabla n_e \tag{2.29}$$

$$k_{mix} = \gamma_{nc}\frac{\nu_{ei}}{\nu_{en} + \gamma_{nc}\nu_{ei}} \tag{2.30}$$

ν_{ei} and ν_{en} are the electron-ion and electron-neutral collision rates respectively. The mixing parameter k_{mix} is similar to the ionization-based mixing in DC-ION, and as in past works γ_{nc} is assumed to be 0.2 [1, 14]. The discharge current is found using a current balance at the anode and is equal to $I_d = I_{ae} - I_{ai} - I_b$.

2.3.4 Primary Density

The primary electron density in the chamber is calculated using a residence time approach, which assumes that the primary electron current out of the cathode I_p is related to the primary density n_p and a characteristic loss time τ by:

$$I_p = \frac{n_p e V}{\tau} \tag{2.31}$$

The primary electron characteristic residence time is calculated as the geometric mean of three separate loss times, including losses to collisions, losses to anode surfaces, and losses to Spitzer relaxation:

$$\tau = \left(\frac{1}{\tau_c} + \frac{1}{\tau_a} + \frac{1}{\tau_s} \right)^{-1} \tag{2.32}$$

The loss time due to losses to anode surfaces, τ_a is given as:

$$\tau_a = \frac{V}{(1 - R_p) v_p A_p} \tag{2.33}$$

The primary loss area A_p is reduced by a reflection coefficient R_p to account for electrostatic reflection of primaries at cathode cusps. v_p, the average velocity of primary electrons, is calculated using the primary acceleration voltage: $V_k = V_d - V_c$. The loss time due to collisions τ_c includes ionization and excitation collisions with neutrals:

$$\tau_c = \frac{1}{n_o v_p (\sigma^* + \sigma^+)} \tag{2.34}$$

σ_* is the excitation cross section for xenon at the primary electron energy. The Spitzer slowing time τ_s [25] is given as:

$$\tau_s = \frac{\omega}{2 A_D l_f^2 G(l_f \omega)} \tag{2.35}$$

G(x) is tabulated, and the intermediate variables are given as:

$$l_f = \sqrt{\frac{m}{2kT_e}} \tag{2.36}$$

$$\omega = \sqrt{\frac{2v_p}{m}} \tag{2.37}$$

$$A_D = \frac{8\pi e^4 n_e ln(\Lambda)}{m^2} \tag{2.38}$$

$$ln\Lambda = 23 - ln(n_e^{1/2}/T_e^{3/2}) \tag{2.39}$$

From these, the mean loss time for primary electrons can be calculated. The primary electron current from the cathode is simply equal to the discharge current lessened by ion current to cathode surfaces:

$$I_p = I_d - I_{ci} - I_{bpi} - I_s \tag{2.40}$$

I_{ci} is ion current flowing back to the cathode and I_{bpi} is the ion current to the backplate.

2.3.5 Ionization Rates

Ionization rates for the LHS of the ion conservation equation are calculated using Rapp ionization cross-sections [26] for xenon. Primary electrons are assumed to be monoenergetic, so the reaction rate is:

$$\langle \sigma^+ v_p \rangle = \sigma^+(v_p) v_p \tag{2.41}$$

Plasma electrons are assumed to be non-monoenergetic, so the reaction rate is the convolution of the plasma speed distribution function and ionization cross sections:

$$\langle \sigma^+ v_e \rangle = \int_0^\infty \sigma^+(v_e) f(v_e) v_e dv \tag{2.42}$$

The electron energy distribution function f is assumed to be Maxwellian, and the results are tabulated in a look-up table for speedier operation.

2.3.6 Power Loss

Power loss from the discharge is classified into two groups: volume dissipation and boundary deposition. Power dissipated into the plasma due to excitations and ionizations can be calculated similarly to ionization rates:

$$P^+ = U^+ I^+ \tag{2.43}$$

$$P^* = U^* I^* \tag{2.44}$$

The ionization rate I^+ is the RHS of the ion conservation equation. The excitation rate I^* is calculated identically to ionization, but with excitation cross sections instead of ionization:

$$I^* = n_o V e (n_p \langle \sigma^* v_p \rangle + n_e \langle \sigma^* v_e \rangle) \tag{2.45}$$

Power leaving the discharge via boundaries (either through beam extraction or energy flux to walls) is categorized into three groups: ion current to cathode surfaces P_{ci}, ion current to anode surfaces P_{ai}, or electron current to anode surfaces P_{ae}. For ion current, power deposited is simply the voltage drop from plasma potential to the electrode times current.

Electron power deposited into anode surfaces is derived in [3].

$$P_{ci} = (V_p + V_d + \phi) \sum_x I_{xi} \tag{2.46}$$

$$P_{ai} = (V_p + \phi) \sum_x I_{xi} \tag{2.47}$$

$$P_{ae} = (2T_e + \phi) \sum_x I_{xe} \tag{2.48}$$

2.4 E×B Probe Theory

E×B probes, or Wein Filters [27], are devices which use crossed electric and magnetic fields to measure the current density in an ion beam as a function of the ion velocity. They operate by magnetically filtering out all ions but those with a particular velocity, and measuring the resulting beam current. A diagram of an ExB probe along with the typical electrical setup is given in Figure 5.8. Their fundamental principle of operation is the Lorentz force equation:

$$\vec{F} = q(\vec{E} + \vec{V} \times \vec{B}) \tag{2.49}$$

In a field where electric and magnetic fields are crossed such that the force due to $q\vec{E}$ and $q\vec{V} \times \vec{B}$ are opposite, there exists a velocity at which the two forces will cancel out, and the net force on the particle will be zero:

$$V = E/B \tag{2.50}$$

In an E×B probe, the magnetic field is usually constant and generated by either permanent magnets or electromagnets. The electric field is generated by a set of parallel plates on

either side of the particle's trajectory. The selected velocity can then be altered by changing the voltage across these plates. Particles are first passed through a collimator to limit the angle at which ions are accepted, then passed through the E×B section to be deflected based off of their velocity and the present fields, then allowed to drift field-free through what is known as the drift tube, passed through a discriminator orifice which blocks out sufficiently off-axis particles, and into a collector cup.

2.4.1 Application in Ion Thrusters

Ion thruster discharges produce both singly and doubly ionized ions, where the doubly charged ions are a source of inefficiency due to their higher charge-to-mass ratio (see Equation 2.7). Both species are accelerated out of the thruster via the beam, at a velocity related to their charge and mass:

$$V = \sqrt{\frac{2q\phi}{M}} \tag{2.51}$$

Doubly charged ions are accelerated to a velocity a factor of $\sqrt{2}$ greater than that of single charged ions, and thus the relative populations of each can be measured using a velocity filter. Combined with current density as determined by a Faraday probe or Retarding Potential Analyzer (RPA), this can be used to determine both the local and total double ion current ratio. This ratio, $\frac{J^{++}}{J^{+}}$, is then used to determine the thrust correction factor discussed in Sec. 2.1.

2.4.2 Analytical Estimation of E×B Output

To aid in the design of new probes, analytical relations for the expected output of an E×B probe as a function of geometry and other properties are needed. Figure 2.4 depicts the geometry of a simplified E×B probe. The collimator consists of two orifices of diameter d_c a distance l_c apart. The maximum angle from axial that an ion can enter at and still pass

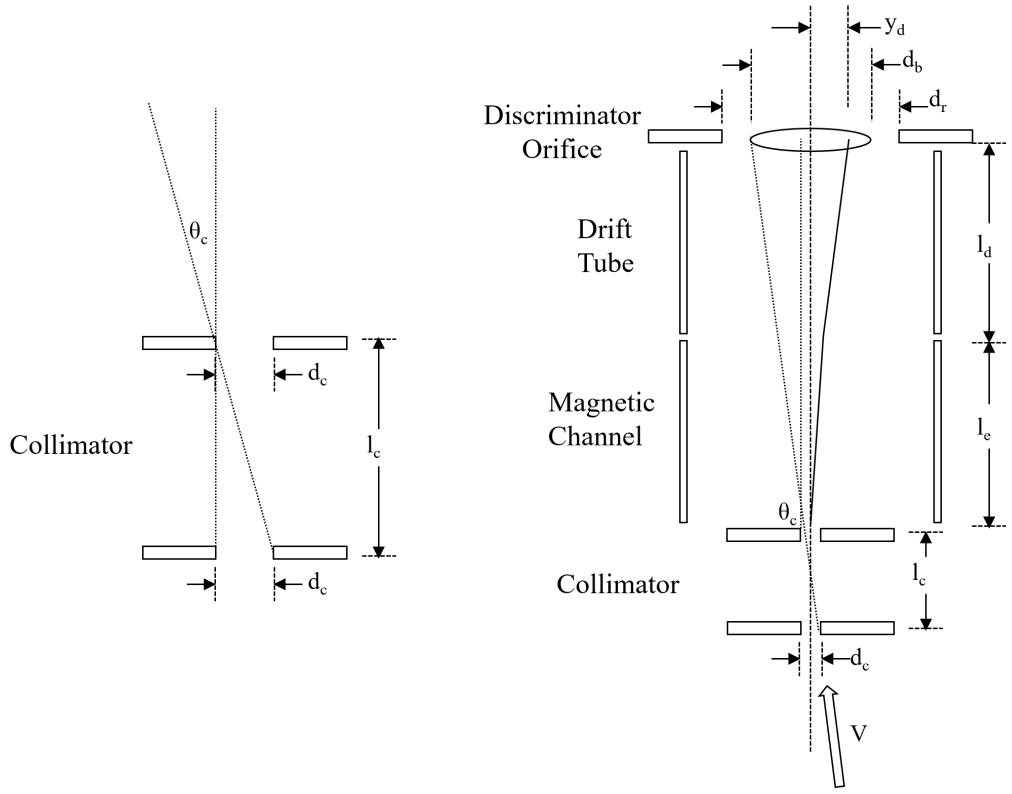

Figure 2.4: Diagram of a typical E×B probe. Ions enter the probe collimator at the bottom.

through is the acceptance angle θ_c, and is calculated as:

$$\theta_c = tan^{-1}(d_c/l_c) \tag{2.52}$$

Assuming the slight angle of off-axis ions does not cause significantly different EM forces than that on the centerline, the undeflected beam width at the rear discriminator is a straightforward calculation:

$$d_b = d_c + 2(l_d + l_e)tan(\theta_c) \tag{2.53}$$

For simplicity, the particles are assumed to experience uniform force in the E×B region, which has perfectly uniform crossed fields with no fringing or edge effects, and forces on the

ions are perfectly radial. In this scenario, the radial distance deflected after the particle has exited the E×B section is:

$$y_{d1} = \frac{F}{2M} t_1^2 \tag{2.54}$$

where t_1 is the residence time in the E×B section. After the drift tube, the total deflection of the beam centerline is (noting that the residence times are simply related to the probe geometry and ion velocity i.e. $t_1 = l_e/V$ and $t_2 = l_d/V$):

$$y_d = y_{d1} + \frac{F}{M} t_1 t_2 = \frac{F}{MV^2}(\tfrac{1}{2} l_e^2 + l_e l_d) \tag{2.55}$$

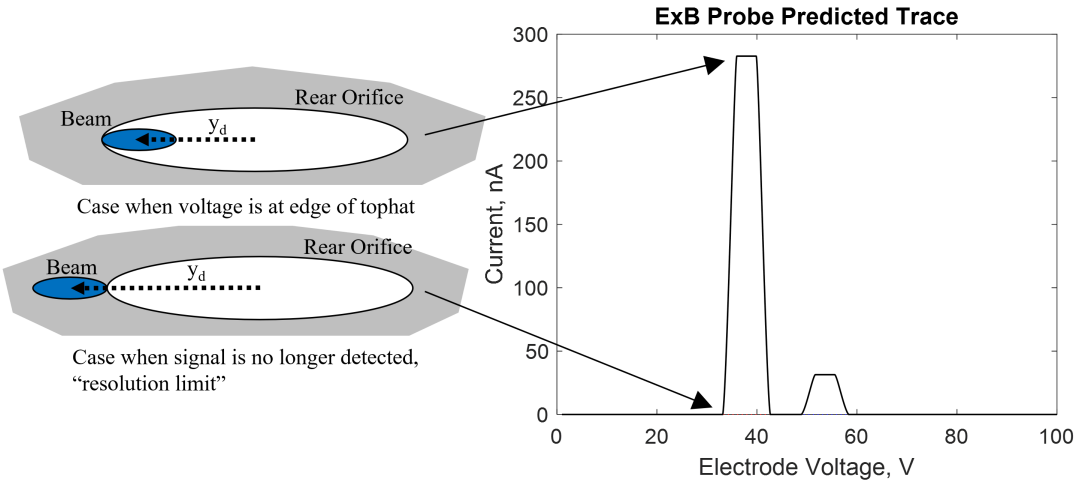

Figure 2.5: Physical causes of the tophat and signal width in an E×B probe trace. Predicted E×B probe trace with 90% singly charged ions and 10% doubly charged ions, calculated using Eq. 2.55 and the calculated intersection area between a uniform deflected beam and rear orifice.

If the rear discriminator orifice is larger than the beam diameter at that point, $d_r > d_b$, then a slight beam deflection will not change the amount of current going into the collector cup. This results in a "top-hat" feature on the plot of collected current vs. electrode voltage. This is depicted in Figure 2.5. The edge of the top-hat can be defined as the point when

the beam begins to impinge on the rear orifice, or $y_d = r_r - r_b$ ($r_r = d_r/2$, $r_b = d_b/2$, and $r_c = d_c/2$). Plugging in this along with the scalar form of Eq. 2.49 yields:

$$q(E - VB) = MV^2 \frac{r_r - r_c - (l_e + l_d)tan(\theta)}{\frac{1}{2}l_e^2 + l_e l_d} \tag{2.56}$$

Let the E field where the beam is undeflected be E_0. Note that at this E field, $q(E_0 - VB) = 0$. Subtracting this from the previous equation and solving for $\phi - \phi_0$ (where $\phi = Ed_e$ is the voltage across the electrodes):

$$\phi - \phi_0 = \frac{d_e MV^2}{q} \frac{r_r - r_c - (l_e + l_d)tan(\theta)}{\frac{1}{2}l_e^2 + l_e l_d} \tag{2.57}$$

This is the half-width of the flat top in the E×B signal trace. There are two ways this equation can be altered. First, by solving as a function of the center potential of the signal. Secondly, as a function of the ion thruster beam potential. Noting Equation 2.50, the first can be obtained:

$$\Delta\phi = \frac{2M\phi_0^2}{qdB^2} \frac{r_r - r_c - (l_e + l_d)tan(\theta)}{\frac{1}{2}l_e^2 + l_e l_d} \tag{2.58}$$

Plugging in Equation 2.51 to 2.57, you can solve for the tophat width as a function of the thruster beam potential ϕ_b:

$$\Delta\phi = 4\phi_b d \frac{r_r - r_c - (l_e + l_d)tan(\theta)}{\frac{1}{2}l_e^2 + l_e l_d} \tag{2.59}$$

The edge of the signal, or the point where the beam is fully impinging on the rear discriminator plate, can be described by $y_d = r_r + r_b$. The previous solution is readily altered by inspection.

$$\Delta\phi = 4\phi_b d \frac{r_r + r_c + (l_e + l_d)tan(\theta)}{\frac{1}{2}l_e^2 + l_e l_d} \tag{2.60}$$

CHAPTER 3

Discharge Performance Impacts on Space Mission Capabilities

This chapter presents a mission capability study for the MiXI thruster. Using the 6U CubeSat form-factor, the potential of MiXI as primary propulsion for high-impulse miniature satellite missions is explored. A baseline CubeSat mission is developed using the thruster for primary propulsion, and the sensitivities of the mission to inputs such as payload mass and volume, thruster I_{sp} and total efficiency, and neutralizer required power and flow are ascertained through parametric analyses.

3.1 Introduction

CubeSats are a class of standardized miniature satellites consisting of 1.33 kg 10 x 10 x 10 cm units or "U"s [28, 29, 30] developed as a platform to provide low-cost access to space. Typical sizes range from 1-3U, although 6 and 12U sized CubeSats have been flown successfully. These satellites leverage increasing densification of electronics and communication equipment to perform tasks previously limited to the realm of much larger spacecraft, ranging from NASA science missions [31] to Earth observation [32]. An in-depth review of CubeSat capabilities as well as a survey of current and planned CubeSat missions was conducted by Poghosyan and Golkar [33]. As secondary payloads or "rideshares", CubeSats are typically deployed in a Low Earth Orbit (LEO) between 500 and 2000 km in altitude. High impulse propulsion enables transfer to different orbits, giving CubeSats more flexibility in rideshare

options. Propulsion also enables single-launch constellation deployment, with craft deploying from one launch vehicle and transferring to individual stations. Several lunar CubeSat missions have been proposed, including the Lunar IceCube mission as a secondary payload on EM-1. There are a number of papers studying low-thrust transfers from LEO to Lunar orbit [34], requiring between 3 and 6 km/s ΔV. Interplanetary missions are the most ambitious class of mission proposed for CubeSats, requiring large ΔV and long lifetimes on the order of 10s of km/s and decades respectively. Recreating missions such as Dawn [35] may reap benefits in cost and development time, although they require CubeSat components with longer lifetimes to withstand several years in transit.

To date, most CubeSat missions have lacked on-board propulsion modules, remaining in their deployed orbit and relying on atmospheric drag to eventually deorbit. While there are some low-impulse propulsion modules available for CubeSats for attitude control and station keeping, few high ΔV CubeSat missions have been flown or are under development, mainly due to a previous lack of low-power, high I_{sp} propulsion. Recently, options such as electrospray thrusters, JAXA's μ-1, Busek's BIT-3, and the Miniature Xenon Ion (MiXI) thruster have emerged, promising CubeSat-class propulsion options with higher efficiencies and I_{sp} than currently available. As these technologies mature, mission planners require assessments of mission capabilities utilizing these new technologies, and development engineers require direction as to the optimal course for further development. To achieve this, we have developed a first-order approximation for a 6U CubeSat utilizing the MiXI thruster, and used this model to both determine mission capabilities in the 6U CubeSat form-factor and the sensitivity of these capabilities to design parameters such as payload requirements and propulsion system properties.

3.2 First-Order Design Methodology for Developing a CubeSat

To assess the capability of the CubeSat platform for high ΔV missions, a notional craft was designed around a 6U chassis and a low power, high efficiency ion engine, the MiXI thruster [36, 1]. Initially, the mass-optimal I_{sp} of a CubeSat mission was explored as a function of system parameters, and then a craft mass and power budget were developed based off of both previous works and commercial off the shelf (COTS) components. The design was then used as a baseline for several parametric studies to assess sensitivity to different design variables. The design process for this study was similar to [37, 38], and is summarized here.

3.2.1 Optimal Mission I_{sp}

When designing a high ΔV mission, selection of the propulsion system is critical. In the mission design phase there are several propulsion options available with a variety of thrusts, total impulse capability, and I_{sp}. A propulsion system's I_{sp} determines the required propellant mass ratio for any given mission ΔV, determined through the rocket equation:

$$m_{wet} = m_{dry} e^{\frac{\Delta V}{g I_{sp}}} \tag{3.1}$$

This relationship shows that propellant mass decreases exponentially with increasing system I_{sp}. However, increasing I_{sp} for an electric propulsion system increases required power, and thus electrical power system (EPS) and solar array mass, for a given thrust. A simple analysis following [22] shows that there is an optimal I_{sp} which balances minimizing propellant mass with minimizing power requirements. The thrust of a propulsion system is given by:

$$T = \frac{2\eta_t P_t}{I_{sp} g} \tag{3.2}$$

Rearranging, and noting that the mass of a craft's thruster-related power system can be

calculated using its specific power, $m_{EPS} = P/\alpha$:

$$m_{eps} = \frac{TI_{sp}g}{2\eta_t\alpha} \tag{3.3}$$

Assuming a fixed dry spacecraft mass (excluding the EPS mass), the spacecraft wet mass and "payload ratio" (ratio of fixed bus mass to wet mass, PF) can be calculated:

$$m_{wet} = (m_{EPS} + m_{fixed})\frac{m_{wet}}{m_{dry}} = (\frac{TI_{sp}g}{2\eta_t\alpha} + m_{fixed})e^{\frac{\Delta V}{gI_{sp}}} \tag{3.4}$$

$$PF = \frac{m_{fixed}}{m_{wet}} = \frac{m_{fixed}}{(\frac{TI_{sp}g}{2\eta_t\alpha} + m_{fixed})e^{\frac{\Delta V}{gI_{sp}}}} \tag{3.5}$$

For any craft fixed mass, thruster thrust and efficiency, there is an optimal I_{sp} which maximizes the payload ratio for a single burn. This can be found analytically by differentiating Eq. 3.5 or using software plotting tools. This analysis is limited to a single maneuver and single throttle point, and only optimizes for maximal payload ratio, not taking into account other important mission features such as thrust-to-mass ratio, burn and transit duration, craft complexity, etc.

3.2.2 Electrical Power System

An EPS is required to process power from the solar arrays into usable power for the bus and payload, and to store energy for eclipse operations. To properly size the EPS batteries, an eclipse power budget and orbital information is needed. An approximate battery mass is given by:

$$m_{batt} = \frac{P_e t_e}{DoD\eta_{batt}\rho_{batt}} \tag{3.6}$$

and the required battery charger power to complete the power budget is given by:

$$P_{charge} = \frac{P_e T_e}{DoD \eta_{batt} \eta_{charge} T_d} \tag{3.7}$$

The total allocated bus power will include the maximum expected bus power for all subsystems, including battery chargers, any inefficiencies, and a margin and contingency. The power required from the solar arrays is then given by $P_{SA} = P_{Bus}/\eta_{EPS}$. The required mass and area for the solar panels are then calculated. End-of-life solar array power output per unit area and array mass are calculated using:

$$\sigma_{SA} = I_s \eta_{SC} \eta_{packing} (1 - D)^{ML} cos(\theta) \tag{3.8}$$

$$m_{SA} = \frac{P_{SA}}{\alpha_{SA}} \tag{3.9}$$

3.2.3 CubeSat bus

The CubeSat bus, including command and data handling (CDH), communications (COMM), and attitude determination and control (ADCS) are assumed to be COTS, and are held constant within this analysis. Within the EPS, the power processing board is constant, while the battery and solar panel masses vary according to Sec. 3.2.2. There are several COTS CubeSat component manufacturers and sellers with flight heritage including Pumpkin, ISIS, CubeSatShop, and others.

3.2.4 Propulsion

The propulsion subsystem includes the thruster, tankage, and the power processing unit (PPU) for converting bus power to power usable by the thruster. For a given dry mass, ΔV, and I_{sp}, the required propellant mass ratio can be calculated using Equation 3.1. Current

best estimate (CBE) propellant mass is calculated using the allocated dry mass.

3.2.4.1 Tankage

Tankage mass is assumed to be between 10 - 20% of allocated propellant mass with plumbing a further 10 - 20% of tankage mass. These values are included in the dry mass but are a function of the propellant mass, so the propellant mass and resulting dry mass are solved iteratively. Tankage volume is calculated using two spherical tanks for small volumes and using two cylindrical tanks with hemispherical caps when required tank volume exceeds that of a spherical tank with radius of 4.5 cm. Xenon is stored at 100 bar, resulting in a density of 1744 kg/m^3 [39, 40].

3.2.4.2 Thruster

The I_{sp}, thrust, and input power are typically givens of the thruster system, and are related to total thruster efficiency through Equation 3.2. For electric propulsion, total thruster efficiency is given by:

$$\eta_t = \frac{T^2}{2\dot{m}_t P_t} \tag{3.10}$$

From these, the massflow of the propulsion system may be calculated.

3.2.4.3 Burn Time

Required maneuver burn time is calculated as the total required propellant divided by the thruster massflow rate, $t_{burn} = m_p/\dot{m}$. Using Equations 3.1, 3.2, and 3.10, the burn time may be calculated as a function of craft dry mass, maneuver ΔV, I_{sp}, total efficiency, and

thruster power:

$$t_{burn} = \frac{m_{dry} g^2 I_{sp}^2}{2\eta_t P_t}(e^{\frac{\Delta V}{gI_{sp}}} - 1) \tag{3.11}$$

3.2.4.4 Effect of Neutralizer Cathodes

Several types of electric propulsion require the use of a neutralizer cathode to prevent spacecraft charging, which uses additional power and (typically) propellant flow. The selection of a neutralizer cathode will thus affect the thruster system's total efficiency and I_{sp}. Calculating the effect of neutralizer cathode operating parameters on thruster system efficiency and I_{sp} requires more in-depth knowledge of the thruster, including the beam voltage, V_b, the discharge loss ϵ, and the neutralizer-free propellant utilization η_p. Ion thruster total efficiency is given as the product of the electrical and propellant efficiencies and a thrust correction factor γ:

$$\eta_t = \eta_E \eta_{p,eff} \gamma^2 \tag{3.12}$$

The thrust correction factor is discussed in Section 2.1, but is typically close to 1 and is neglected here. The electrical efficiency is the ratio of beam power to total power:

$$\eta_E = \frac{j_b V_b}{P_t} \tag{3.13}$$

Total thruster power is the sum of the beam power, discharge power, and neutralizer power:

$$P_t = j_b(V_b + \epsilon) + P_n \tag{3.14}$$

Discharge power is calculated in Equation 3.14 using the discharge loss ϵ, which is the

discharge power cost to generate one amp of beam current. Given some total power, neutralizer power, discharge loss, and thruster beam voltage, the beam current and electrical efficiency may be calculated. The effective propellant efficiency is the ratio of beam massflow to total massflow:

$$\eta_{p,eff} = \frac{M_i j_b / q}{\dot{m}_d + \dot{m}_n} \tag{3.15}$$

Where the discharge massflow $\dot{m}_d$ can be calculated using the beam current and the neutralizer-free propellant utilization via $\dot{m}_d = M_i j_b/(q\eta_p)$. Equations 3.12-3.15 may be solved computationally for $\eta_{T_eff} = f(\dot{m}_n, P_n)$, or analytically using the expression:

$$\eta_T = \frac{j_b^2 V_b}{Pq(\frac{j_b}{q\eta_p} + \dot{m}_n)} \tag{3.16}$$

Where the beam current is given as:

$$j_b = \frac{P - P_n}{V_b + \epsilon} \tag{3.17}$$

The effective I_{sp} of a thruster ($I_{sp,eff}$) with a given neutralizer-free I_{sp} and some neutralizer flow $\dot{m}_n$ is given as:

$$I_{sp,eff} = I_{sp}\frac{\dot{m}_d}{\dot{m}_d + \dot{m}_n} \tag{3.18}$$

These effective values of I_{sp} and η_T may then be used to calculate maneuver burn time and wet mass as a function of neutralizer cathode parameters.

3.2.5 Payload Volume

Available payload volume within the chassis is calculated by subtracting bus and tankage volume from the total available volume (6U). Bus volume is assumed to be 1U. The tankage

is split into two tanks which grow from the aft of the craft, so payload volume consists of the volume between the tanks and the bus in the front of the craft.

3.3 Optimal Mission I_{sp} and Propulsion Technology Selection

To determine the mass-optimal I_{sp} for a high ΔV CubeSat mission, a fixed non-EPS dry mass of 10kg was assumed and the results calculated for a range of thrust, ΔV, and efficiency values. Some representative cases are shown in Figure 3.1. This analysis suggests that very high I_{sp} is beneficial to future high ΔV CubeSat missions, even at low thruster efficiencies and EPS specific masses. One limitation of this analysis is that it optimizes for payload mass ratio, without taking into account other limitations of high-I_{sp} propulsion such as increased required burn duration. There are a variety of propulsion technologies possible for CubeSats, although few are designed for high impulse, low-power operation have been matured to high TRL. Table 3.1 lists small spacecraft propulsion options taken from [41]. The TRL listed is the highest value present in the technology category including higher power versions for full-scale spacecraft, and does not necessarily imply that the low-power CubeSat versions are mature. Several high I_{sp} propulsion options are shown detailing regions of applicability in terms of I_{sp}, power level, and thrust in Figure 3.2, adapted from [38]. For high ΔV at CubeSat power levels (10 - 50 W), ion engines are a good choice for primary propulsion. In this study, the Miniature Xenon Ion thruster is the selected propulsion technology.

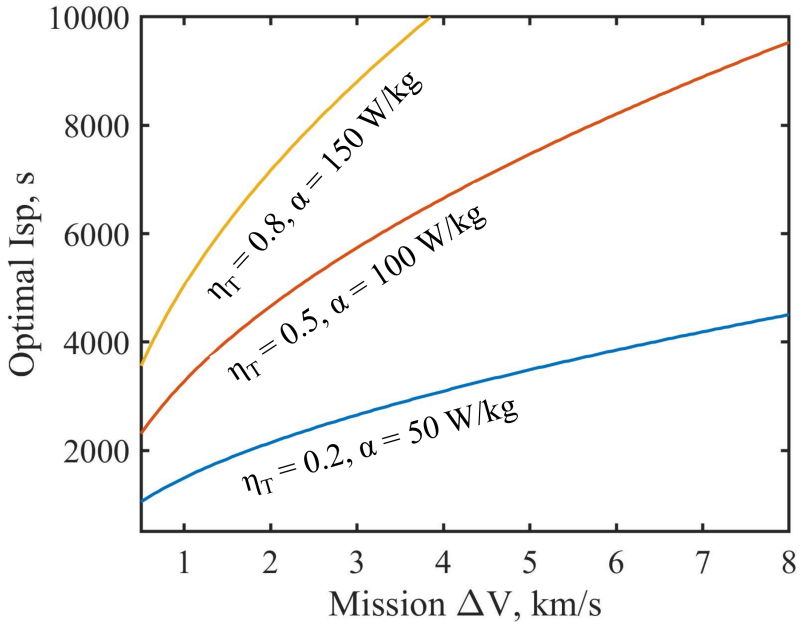

Figure 3.1: Optimum I_{sp} as a function of ΔV for varying values of η_t and α. Highly efficient craft have higher optimal $I_{sp}s$ due to lower EPS mass for a given power, and lower power requirement for a given I_{sp} and thrust.

Table 3.1: CubeSat Propulsion Technologies.

Technology	Thrust	I_{sp}, s	TRL
Hydrazine	0.5 - 4 N	150-250	TRL 6
Cold Gas	10 mN - 10 N	65 - 70	GN2/Butane TRL 9
Non-toxic Propulsion	0.1 - 27 N	220 - 250	HAN TRL 8, ADN TRL 6
PPTs and Vac. Arc Thrusters	1-1300 μN	500 - 3000	Teflon TRL 8, Titanium TRL 7
Electrospray Propulsion	10-120 μN	500 - 5000	TRL 6
Hall Effect Thrusters	10 - 50 mN	1000 - 2000	Xenon TRL 8, Iodine TRL 4
Ion Engines	1 - 10 mN	1000 - 3500	Xenon TRL 8, Iodine TRL 4
Solar Sails	0.25 - 0.6 mN	N/A	TRL 6 ($85m^2$), TRL 7 ($35m^2$)

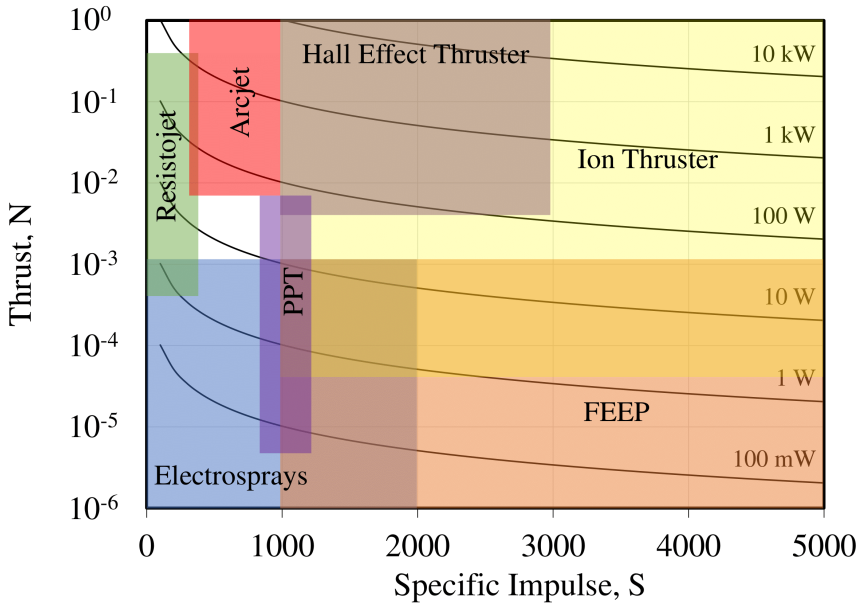

Figure 3.2: Constant power curves with I_{sp} and thrust, with various propulsion technologies' areas of operation overlaid. In the 2000+s, 1 - 100 W range, ion thrusters are the ideal choice.

3.4 Notional Mission and Craft

The principles outlined in Section 3.2, [37], and [38] were used to design a notional 6U CubeSat for a 3,000 m/s ΔV mission, originating in a 600 km LEO orbit with a 4 kg 15 W payload. This payload is significantly larger than other CubeSat missions, including the Lunar IceCube [42] at 2kg, 7W, 1.5U. Using primarily COTS components, the craft uses technology that is either currently available or has near-term availability. All values of mass and power requirements, whether derived or from manufacturer specifications, have a 20% contingency and 15% margin with the exception of the payload values which are given as allocated values. The relations in [37, 38] and Section 3.2 were then input into a Microsoft Excel workbook, and the resulting total spacecraft mass, burn time, and payload volume were solved through Excel's iterative solver. The resulting craft, henceforth generically referred to as the 6U MiXI CubeSat, has a dry mass of 11.3 kg including a 4 kg 3U payload, and a wet mass of 12.9 kg. The approximate required burn time to achieve 3 km/s ΔV is 50 weeks. The power and mass budgets are presented in Tables 3.2 and 3.3, respectively.

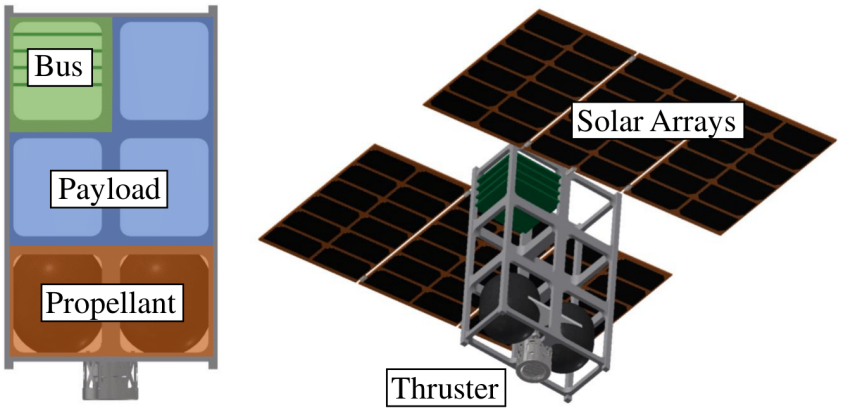

Figure 3.3: Notional CAD of 6U MiXI CubeSat detailing basic craft layout.

Table 3.2: 6U MiXI CubeSat Allocated Power Budget

		Cruise Phase Power (W)		Science Phase Power (W)	
Subsystem	Component	Day	Eclipse	Day	Eclipse
Propulsion					
	MiXI Thruster	30	0	0	0
	PPU	3.3	0	0	0
	Gimbal	2	0	0	0
	HC Heater	0	10	0	0
Structure					
	SA Gimbals	2	0	2	0
Power					
	Board	0.1	0.1	0.1	0.1
	Battery Charger	7	0	7	0
ADCS					
	Int. ADCS Board	1	0	1	0
Thermal		0	0	0	0
CDH					
	CDH Board	0.4	0.4	0.4	0.4
COMM					
	COMM Board	1.7	1.7	1.7	1.7
Payload		0	0	15	15
20% Cgy.		9.5	2.6	2.5	0.6
15% Mgn.		8.5	2.4	2.2	0.6
Totals		65.6	14.4	31.8	19.4

3.4.1 Propulsion

The Miniature Xenon Ion thruster (shown in Figure 1.4) was selected for this mission, a highly efficient thruster with thruster-only (excluding effects of the neutralizer cathode, discussed in Section 3.5.4) performance of 3080 s I_{sp}, 30 W input power, 1.2 mN thrust [43, 17]. A PPU efficiency of 90% is assumed. The thruster is outboard, gimbaled on a 150 g, 2 W gimbal. A propellantless neutralizer cathode is assumed with a specific heating of 40 W/A. The type of neutralizer cathode for the MiXI thruster is an open question. Propellantless cathodes, such as field-emission cathodes, are attractive due to no propellant use and very low required power, but are currently immature and have unproven lifetimes. Oxide-coated brush

Table 3.3: 6U MiXI CubeSat Allocated Mass Budget

Subsystem	Component	Unit Mass (kg)	Qty	Total Mass (kg)
Propulsion				
	MiXI Thruster	0.1	1	0.1
	PPU	0.1	1	0.1
	Gimbal	0.15	1	0.15
	Tank	0.1	2	0.21
	Plumbing & Flow Control	0.24	1	0.24
	Propellant	1.2	1	1.2
Structure				
	Primary Structure	1.1	1	1.1
	SA Gimbals	0.14	2	0.28
	10x10cm Panels	0.05	22	1.1
	Brackets	0.005	30	0.15
Power				
	Board	0.1	1	0.1
	Battery	0.11	1	0.11
	Solar Panels	0.34	2	0.68
ADCS				
	Int. ADCS Board	0.62	1	0.62
Thermal				
CDH				
	CDH Board	0.1	1	0.1
COMM				
	COMM Board	0.1	1	0.1
	Antenna	0.1	1	0.1
20% Cgy.				1.3
15% Mgn.				1.2
Payload		4	1	4
Total				12.9

cathodes suffer from space-charge limiting effects, and have been superseded by thermionic hollow cathodes. Hollow cathodes are the standard electron emitter for mid and high-power electric propulsion, as they are robust and efficient, however they operate poorly below 1 sccm flow and 1 A discharge current [18]. With the increasing use of low-power electric propulsion more development is occurring in this realm of low-power hollow cathodes with several approaching the needed flow and current levels needed for the MiXI thruster [21, 20],

and with future development hollow cathodes may meet the low power and flow requirements for MiXI discharge and neutralizer cathodes.

Tankage mass fraction was assumed to be 15% with plumbing contributing an additional 20% of tank mass. While commercial high pressure xenon storage has not yet been developed for CubeSats, this value may be reasonable as it results in a more conservative tankage mass than linearly scaling current low-volume 690 bar tanks such as the General Dynamics 220133-1. Xenon is stored with a density of 1774 kg/m^3 at 100 Bar [44, 40]. The volume occupied by the tanks is calculated by calculating the total length of the tanks, which are short rings 1 cm in length and 9 cm wide with hemispherical caps on either end. The propellant management system values are taken from a system developed by Collard, Sheehan, and Gallimore [44] for the CubeSat Ambipolar Thruster. Because the tank pressure is greater than 1 bar, the thruster is outboard, and the wet mass is greater than 12 kg, a CubeSat specification waiver is required. The thruster can be moved to an in-board configuration to retain compatibility with 6U PPODs which do not have the "tunacan" space, at a payload volume penalty of ˜1U. An additional consideration is that this would also cause more thruster waste heat to be deposited into the structure, increasing overall craft temperature.

3.4.2 Electrical Power System

The EPS requires 10 W-hr battery storage capacity to power essential components and a 10 W hollow cathode heater during eclipse (˜30 min). Peak power processing capability is required to be 66 W, which is within the capability of current CubeSat EPSs like those from BlueCanyon Tech or Pumpkin Aerospace. Current COTS deployable panels are capable of generating the required power, including the Blue Canyon Tech 6U-H Triple Wing Solar Array and the MMA eHAWK. To calculate required solar panel mass, an array specific power of 120 W/kg was used [45].

3.4.3 Structure

A COTS 6U CubeSat structure from ISIS was selected [46]. The mass of side panels and additional structure was taken from earlier works [37]. Small single axis gimbals are used to control the solar array orientation, with assumed 1 W power and 20% SA mass each. This results in a more conservative estimate than commercial offerings such as the Honeybee CubeSat SADA [47].

3.4.4 Other Subsystems

The Structure, Communications and Command and Data Handling subsystems are out of scope of this analysis, other than having required masses and powers. The COMM system values are based off of the ISIS duplex module [48], and the CDH values are based off of the ISIS on board computer [49]. For deep-space applications, a full link-budget analysis is required to assess the viability of current CubeSat communications boards. The ADCS subsystem is a CubeADCS 3-axis integrated system containing hardware for both attitude determination and control. The total momentum storage capability is greater than the required amount needed to spin the craft up to one full rotation per orbit (for a constant prograde burn). Future analyses are needed to determine compatibility with science mission requirements of slew rate, pointing accuracy, etc, and must take into account the gimbaled MiXI thruster for momentum dumping.

3.4.5 Inclination Change Capability

Potential inclination change for a low-thrust spiral trajectory is given as a function of maneuver ΔV and orbit in Figure 3.4, calculated using the Edelbaum equation. High ΔV capability enables large changes in inclination, for missions such as single-launch constellations and flexible earth observation missions.

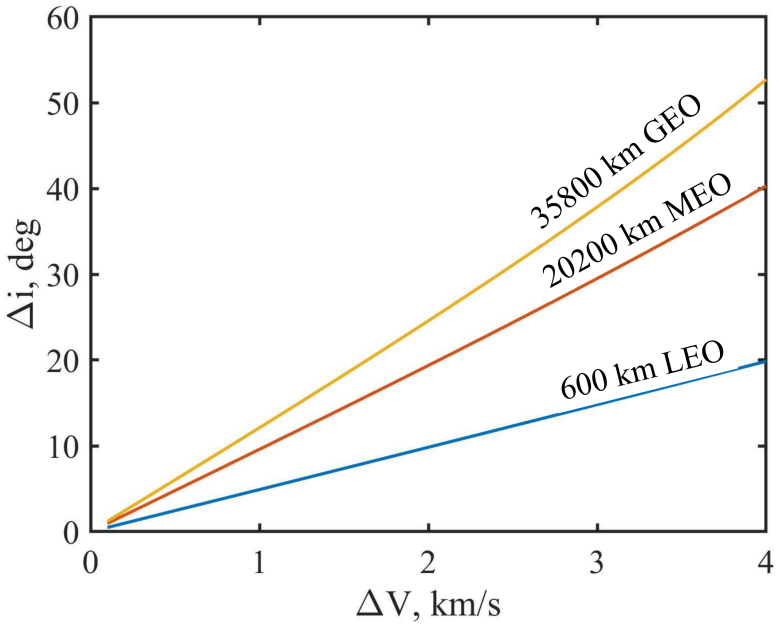

Figure 3.4: Inclination change capability as a function of ΔV for various circular orbits.

3.5 Discussion of Results

3.5.1 Payload Volume and Wet Mass as Function of ΔV

A parametric analysis of the 6U craft design was performed to assess the sensitivity of the craft design to input mission parameters such as required ΔV, payload mass, bus mass, and thruster properties. These analyses were performed using Microsoft Visual Basic to step through input parameters and extract calculated results from an Excel workbook. The available payload volume and wet mass for a variety of craft dry masses as a function of required ΔV were calculated, shown in Figure 3.5. Craft dry mass, which includes the craft bus, payload, and tankage, is used rather than payload mass to retain utility with alternate bus configurations which have a different mass than that of this particular configuration. Note that the wet mass plot only includes configurations corresponding to payload volumes greater than zero. For a given required ΔV, increasing dry mass decreases available payload volume, and increases wet mass. For a set payload volume, increasing craft dry mass

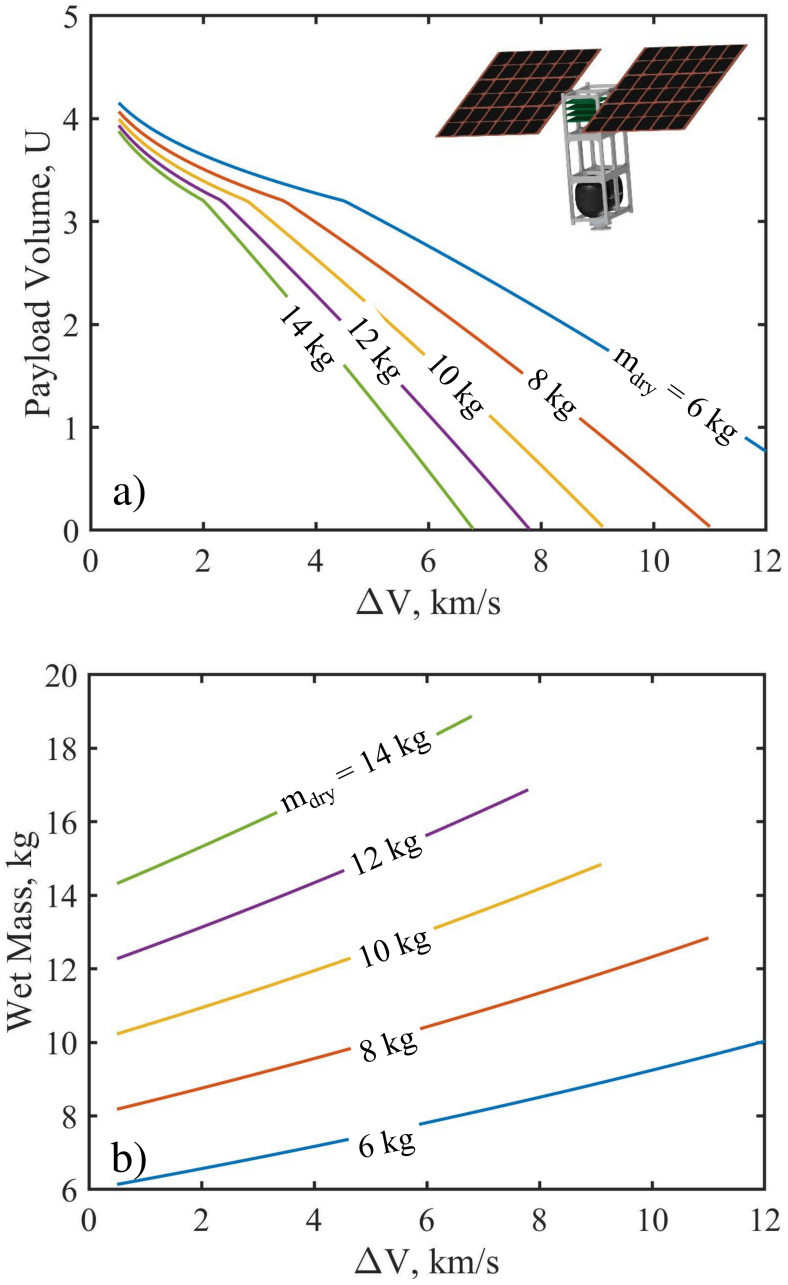

Figure 3.5: Payload volume and wet mass for a variety of craft dry masses as a function of ΔV. Craft bus mass is approximately 7.3kg. Tankage mass changes along curves, but has a small effect.

decreases maximum achievable ΔV. For the bus + payload mass of 11.3 kg, the maximum ΔV for a 0.5U payload volume is 8.2 km/s, although this is sensitive to assumed bus volume

(1U in this study). The 6U MiXI CubeSat, with no payload, is capable of 10.9 km/s ΔV. The results are similar to that of [37], including the bend in Figure 3.5 due to the initially spherical tanks transitioning to cylindrical as the volume exceeds that of a sphere 4.5 cm in radius.

3.5.2 ΔV Capability as a Function of Payload Volume and Mass

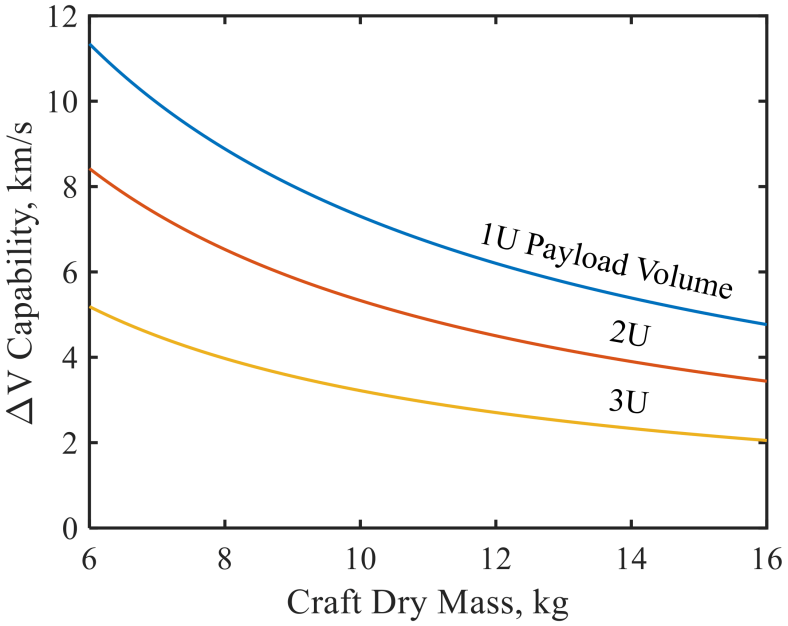

Figure 3.6: Maximum ΔV capability for a variety of payload volume curves as a function of craft dry mass, which is the bus mass + payload mass. Required burn time to achieve the maximum possible ΔV is constant along each curve, and is 2.24 yr for 1U, 1.58 yr for 2U, and 0.92 yr for 3U.

To determine capability as a function of payload requirements, a parametric analysis was performed to calculate the maximum ΔV capability for various payload volumes and masses. This was calculated by determining the volume available for propellant tanks at a given payload and bus volume, calculating the maximum possible propellant mass, and using Equation 3.1 to calculate the maximum possible ΔV. Results are presented in Figure 3.6 for a generalized craft dry mass. To get payload mass for the XPC craft, subtract 7.3

kg. With only the 7.3 kg bus, the craft is capable of up to 9 km/s for a 1U payload volume, 6.9 km/s for a 2U payload, and 4.3 km/s for a 3U payload. Maximum possible ΔV is more sensitive to payload volume than mass, with a 1 kg 3U payload resulting in the same max ΔV capability as a 12 kg, 1U payload. Note that although the ΔV capability is similar between these payloads, burn time is not. Due to the constant massflow of the thruster, and the same propellant mass with constant payload volume, burn time remains constant as a function of payload volume. Burn times in this case are 2.24 yr, 1.58 yr, and 0.92 yr for a 1, 2, and 3U payloads respectively.

3.5.3 Thruster Performance Analysis

To assess the sensitivity of craft performance to thruster parameters, two sensitivity analyses were performed with the original 6U MiXI CubeSat as a baseline. First, the required burn time for a 3 km/s and 6 km/s ΔV maneuver as a function of thruster efficiency and I_{sp} were calculated, presented in Figure 3.7. This analysis assumes craft dry mass to be that of the original study, along with a 4 kg payload. With increasing efficiency, burn times decrease due to increasing thrust. Increasing I_{sp} increases burn time, due to a decreasing thrust with increasing I_{sp} (and constant input power). The second analysis was the craft wet mass as a function of thruster I_{sp} for a variety of mission ΔVs. This also assumes the original bus with a 4 kg payload, resulting in an 10.9 kg dry mass excluding tankage and plumbing, which is a function of propellant mass. Wet mass is not considered to be dependant on thruster efficiency, which only affects thrust per unit power. Note that payload volume is not constant in this analysis, changing with ΔV requirement and thruster I_{sp}. The result of this analysis is presented in Figure 3.8. This analysis results in a simple exponential relationship between I_{sp} and wet mass due to the Rocket Equation: wet mass decreases with increasing I_{sp} and increases with required ΔV.

Figures 3.7 and 3.8 are useful when taken together in determining the tradeoffs between I_{sp}, total efficiency, wet mass, and burn time. For a 4 kg payload, a 3 km/s maneuver with

the MiXI thruster will require a burn time of slightly less than 11 months, and a wet mass of 12.9 kg. As seen in Figure 3.7, increasing the MiXI thruster's efficiency from 59% to that of larger thrusters (∼70%) will decrease burn duration by 16%, or 4 months for a 6 km/s maneuver. Of the trade parameters considered, I_{sp} is readily alterable, whereas total efficiency is typically maximized and set during the design process. Increasing I_{sp} decreases wet mass, but in turn decreases thrust which in turn increases burn time. This results in a tradeoff between burn time and wet mass, which for some missions may result in lower I_{sp} propulsion being more favorable. For example, the previous 16% reduction in burn time for a 6 km/s maneuver may also be accomplished with no efficiency improvements by dropping the I_{sp} to 2470 s with a weight penalty of 1.4 kg, as seen by tracing the difference in wet mass for a 6km/s burn between 3000 and 2470s I_{sp} in Figure 3.8.

3.5.4 Effect of Neutralizer Cathode Selection

To assess the sensitivity of mission capability to neutralizer cathode selection, required burn time and wet mass were calculated as a function of neutralizer flow and power and are presented in Figure 3.9. As can be seen in Figure 3.9, mission burn time is more sensitive to neutralizer power, while wet mass is sensitive to neutralizer flow. The primary effect of increased neutralizer massflow is a reduction in effective I_{sp}, which increases wet mass. This effect may be ameliorated through increased I_{sp} operation, where there may be some optimum value balancing low propellant mass with higher thrust operation. Increased neutralizer power reduces power available to the thruster, decreasing thrust and increasing burn time. Cathodes requiring above 0.7 sccm do not result in feasible mission solutions for a 3000 m/s burn, because the effective I_{sp} is strongly affected by neutralizer flow and becomes too low when neutralizer flow is above 0.7 sccm. At low I_{sp}, the required propellant volume is in excess of the 5U available within the chassis, thus resulting in an infeasible design. This effect may be lessened by utilizing higher thruster power, so that the relative magnitude of neutralizer power is decreased. Several candidate neutralizer cathodes and their resulting

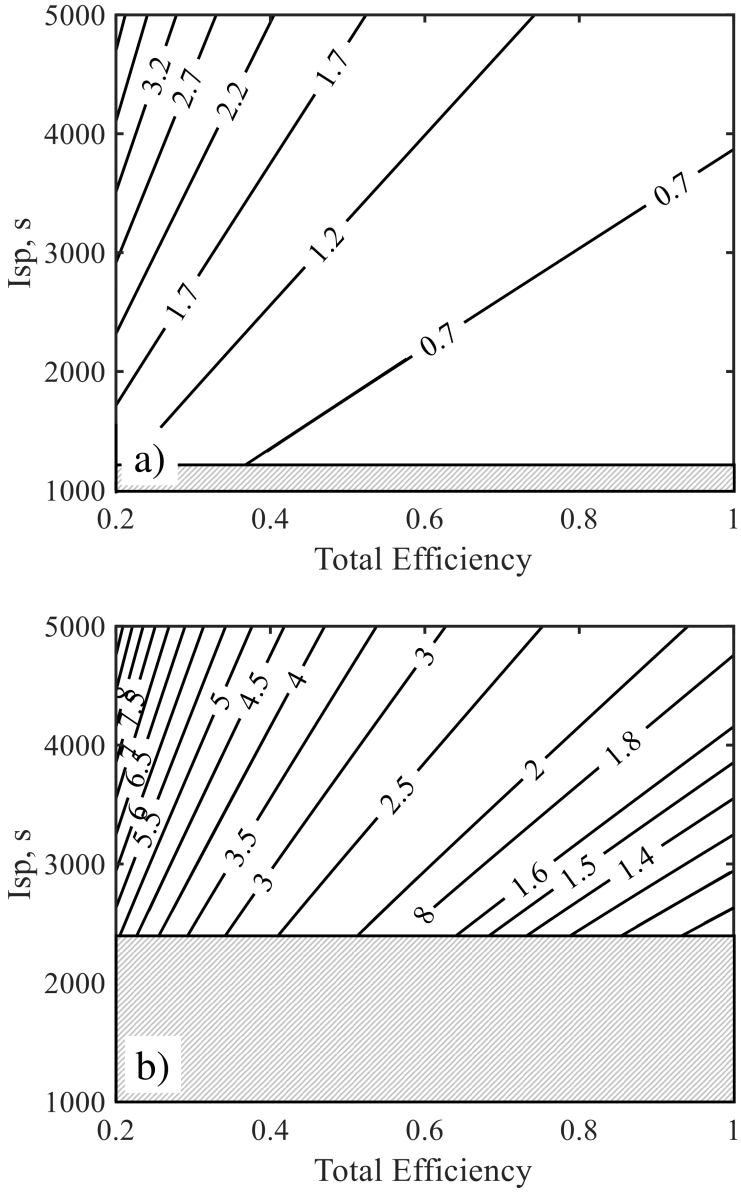

Figure 3.7: Required burn time in years as a function of I_{sp} and total thruster efficiency for the 6U MiXI CubeSat and a 4 kg payload for a) 3km/s and b) 6 km/s ΔV. Grey sections denote parameters which result in an infeasible craft configuration, with propellant volumes exceeding the available amount.

mission performances are presented in Table 3.4 for a 1.6 km/s ΔV burn, selected so that all options return feasible solutions (positive payload space). A filament brush cathode returns the best performing craft, with a burn time of 6 months and 11.9 kg dry mass. A miniature

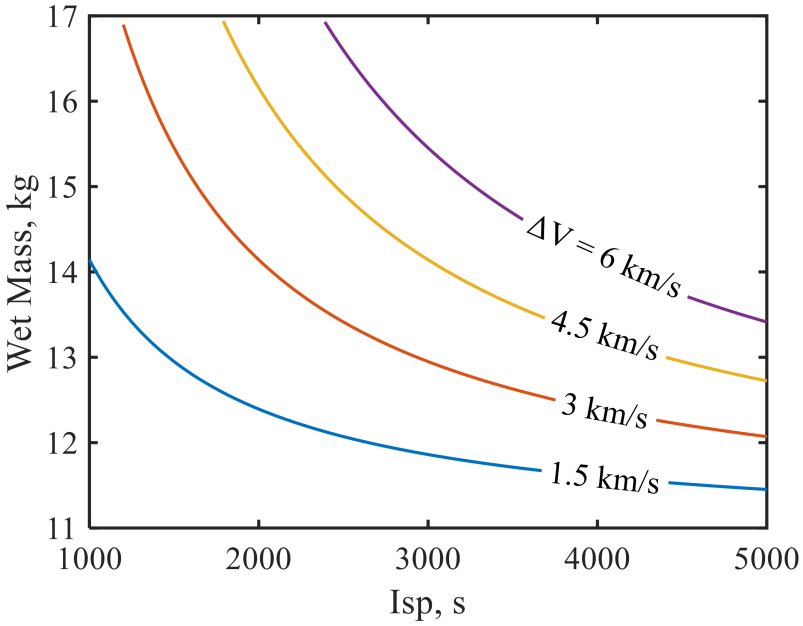

Figure 3.8: Craft wet mass as a function of I_{sp} and maneuver ΔV for the 6U MiXI CubeSat and a 4 kg payload. At above 17 kg wet mass, propellant tank volume is larger than that of the available space inside the craft.

hollow cathode as described by Domonkos [18] results in a craft wet mass of 17 kg due to a high flow requirement of 1 sccm. Note that 17 kg wet mass is the upper limit of this craft design, with almost all available volume taken up by propellant.

Table 3.4: 6U MiXI CubeSat mission performance for $\Delta V = 1.6$ km/s with various neutralizer cathodes.

Ref	Technology	Required Flow, sccm	Additional Power, W	Burn Duration, yr	Wet Mass, kg
[18]	DC Hollow	1	11	0.92	17.0
[50]	Microwave	0.11	9	0.70	12.3
[51]	Filament Brush	0	1	0.49	11.9

3.5.5 Implications for MiXI Development

The results of this study have several implications for future MiXI development. As shown in Section 3.5.3, the introduction of a low-I_{sp} throttle level significantly improves burn time

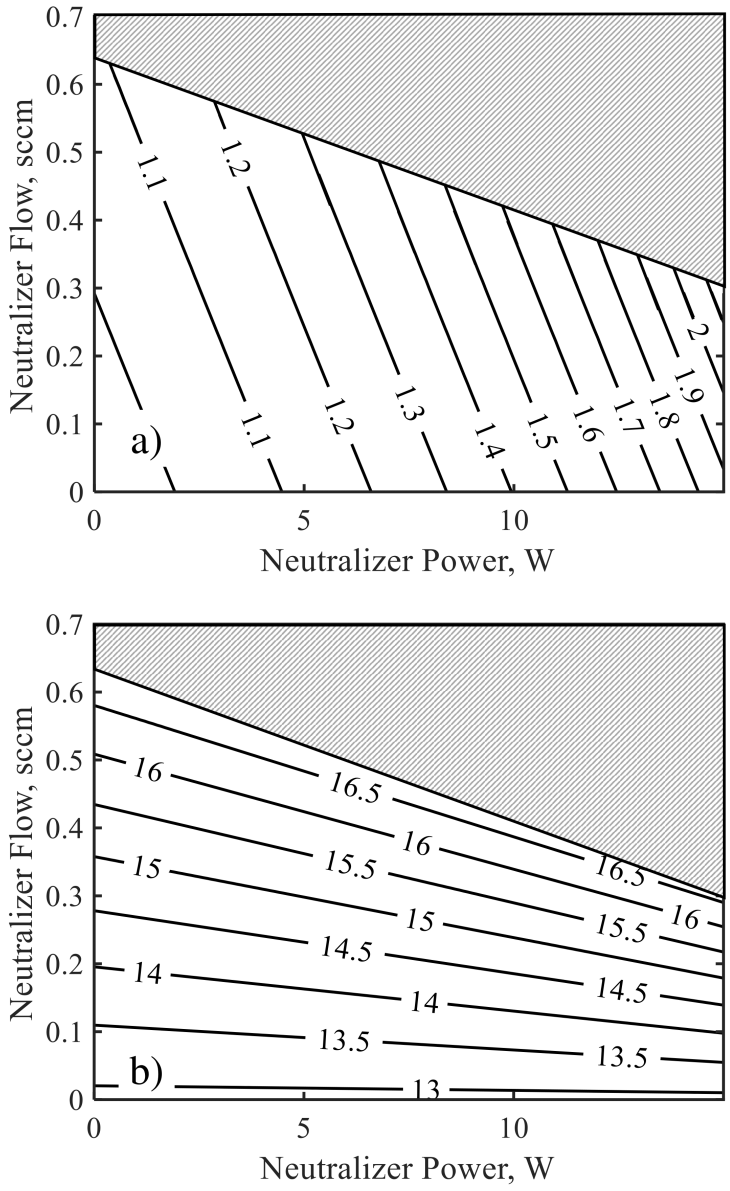

Figure 3.9: Required burn time and wet mass as a function of neutralizer cathode properties for a 3 km/s burn with the 6U MiXI CubeSat and a 4 kg payload.

for a small mass penalty. While an actual mission development program will likely optimize the trajectory with multiple burns rather than the simple burn, this analysis still suggests that for some burns, a low I_{sp} throttle level will be beneficial. Current MiXI operation has been characterized at 0.5 sccm, but for constant power and lower I_{sp} operation higher flow

values may be used. As shown in [43], the MiXI discharge is more efficient at higher flow values up to 0.8 sccm. This may compensate for the expected loss in electrical efficiency at lower beam voltages.

The sensitivity of mission capabilities to neutralizer properties is critical, as detailed in Section 3.5.4. For a 3 km/s ΔV mission, a neutralizer flow of just 0.7 sccm reduced system I_{sp} to the point of being unusable. Current development focuses on implementing a miniature hollow cathode for the discharge, and future development will include development and characterization of a MiXI-sized tantalum brush neutralizer cathode, including verification of acceptable lifetimes for future MiXI primary propulsion missions.

3.6 Conclusion

Using simple relations for calculating propellant and EPS mass, it was shown that the optimal I_{sp} for a 3000 m/s CubeSat mission is between 2000 s and 5000 s for realistic system efficiencies and specific powers, demonstrating the utility of miniature ion thrusters and other high I_{sp}, low power propulsion technologies for CubeSats. A high-impulse 6U CubeSat was presented, utilizing the 30 W MiXI thruster to enable missions with more than 10 km/s ΔV with no payload, up to 9 km/s with a 1 U payload, and up to 4.3 km/s with a 3 U payload.

One notional mission with a 3000 m/s ΔV and a 4 kg, 3U payload, resulted in a mission wet mass of 12.9 kg and burn duration of 11 months. Parametric studies show that this mission configuration is sensitive to thruster I_{sp} and total efficiency, with a 10% increase in thruster efficiency resulting in a 16% decrease in mission burn time. This decrease in burn time was also shown to be possible by decreasing I_{sp}, although at a 1.4 kg mass penalty. Parametric studies of neutralizer cathode properties show that the neutralizer cathode selection is critical, with required neutralizer flow affecting craft wet mass and neutralizer power strongly affecting mission required burn time. Neutralizer cathode flow decreases the effective system I_{sp}, and decreases the maximum potential ΔV for a given

payload, with 0.7 sccm being the maximum feasible value for the notional 3 km/s mission. As a solution to the low power and flow requirements for CubeSat neutralizer cathodes, brush cathodes may be suitable for shorter duration missions, although more life testing of low-current neutralizer brush neutralizer cathodes is needed. The advent of low-power, high-efficiency electric propulsion enables an impressive range of high impulse CubeSat missions, opening up a breadth of new opportunities for the diminutive craft.

CHAPTER 4

Miniature Discharge Performance Characterization and Simulation

In this chapter, the MiXI thruster is characterized with filament cathodes for discharge and neutralizer across a range of propellant flow rates, discharge voltages, and anode aspect ratios. The analytical control-volume model described in Section 2.3 is then used to investigate the obtained data, return internal loss mechanisms, and explore processes which drive the stability and efficiency of the thruster.

4.1 Analytical Investigation into Ion Thruster Miniaturization

As noted in Section 4.3, past miniaturization of ion thrusters has resulted in less efficient devices than past, larger thrusters. To investigate this historical trend, it is instructive to construct a "bare-bones" simplified analytical model to determine if these efficiency losses are merely engineering issues, or rooted in the inherent physics of plasma discharges. The relationship between discharge loss ε and thruster properties was derived in Section 2.2:

$$\varepsilon = \frac{4 I_b V U^*}{0.6 A_g T_i T_o A_g^2 e \eta_c} \frac{1-\eta_p}{\eta_p} \frac{\langle \sigma^* v_e \rangle}{\sqrt{k T_e / M}} + \frac{U^+}{T_i} + \frac{T_e}{T_i}(2ln\left[1.2 \frac{A_a}{A_g}\sqrt{2\frac{M}{\pi m}}\right] + 2.5)) \tag{4.1}$$

For a fixed propellant utilization and electron temperature, several relationships are evident. The discharge loss is inversely proportional to the ion transparency T_i, i.e. the ratio

of beam current to current into the extraction plane. Increasing beam current increases discharge loss (at least for a fixed electron temperature, as will be discussed below), and there are several variables, V, A_g, and A_a, which are functions of thruster size. Allowing each of these to be some value k times a length scale r to the appropriate power, and substituting in $I_b = j_b r^2$, results in the following equation:

$$\varepsilon = \frac{k_1 j_b r U^*}{0.6 T_i T_o e \eta_c} \frac{1-\eta_p}{\eta_p} \frac{\langle \sigma^* v_e \rangle}{\sqrt{kT_e/M}} + \frac{U^+}{T_i} + \frac{T_e}{T_i}(2ln\left[k_2\sqrt{2\frac{M}{\pi m}}\right] + 2.5)) \tag{4.2}$$

It would appear that the discharge loss will increase with increasing thruster radius, but electron temperature and the reactivity $\langle \sigma^* v_e \rangle$ are functions of radius which subvert intuition. Electron temperature is a function of propellant utilisation through the relationship in Eq. 2.20:

$$\frac{4 I_b V}{0.6 A_g^2 v_o e T_o \eta_c} \frac{1-\eta_p}{\eta_p} = \frac{\sqrt{kT_e/M}}{\langle \sigma^+ v_e \rangle} \tag{4.3}$$

The RHS of Eq. 4.3 is a function of electron temperature only, shown in Figure 2.1. With increasing value of the RHS, the electron temperature decreases. For a set propellant utilization η_p, it can be seen that electron temperature will decrease with increasing beam current I_b, and increase with increasing grid optical transparency T_o, grid Clausing factor η_c, and neutral thermal speed v_o. From Equation 4.1, it can be shown that increased electron temperature increases both the first and third term, increasing discharge loss (the factor $\langle \sigma^* v_e \rangle / \sqrt{kT_e/M}$ increases with increasing T_e). Performing a similar scaling analysis here gives the electron temperature trend as a function of thruster properties:

$$j_b r \frac{1-\eta_p}{\eta_p} \propto \frac{\sqrt{kT_e/M}}{\langle \sigma^+ v_e \rangle} \tag{4.4}$$

From Eq. 4.4 and Fig. 2.1, it can be seen that increasing thruster radius or beam current density will, for a given propellant utilization, decrease the electron temperature. Several

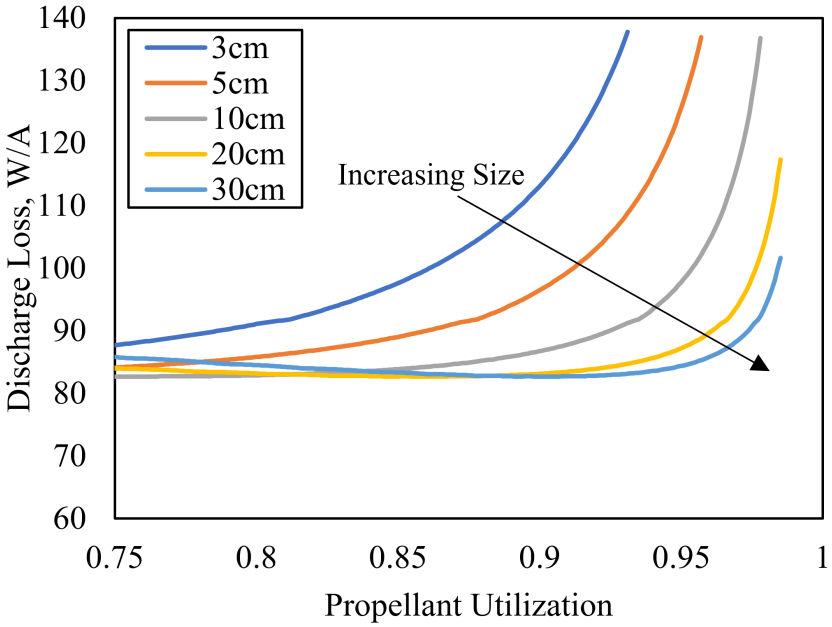

(a) Discharge Loss

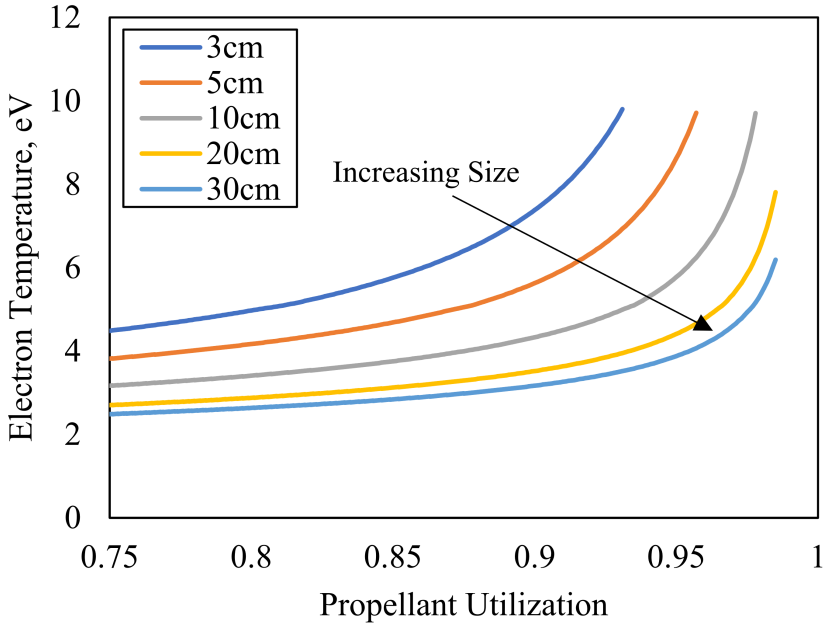

(b) Total Efficiency

Figure 4.1: Discharge loss and electron temperature as a function of propellant utilization with varying thruster radius at a fixed beam current density.

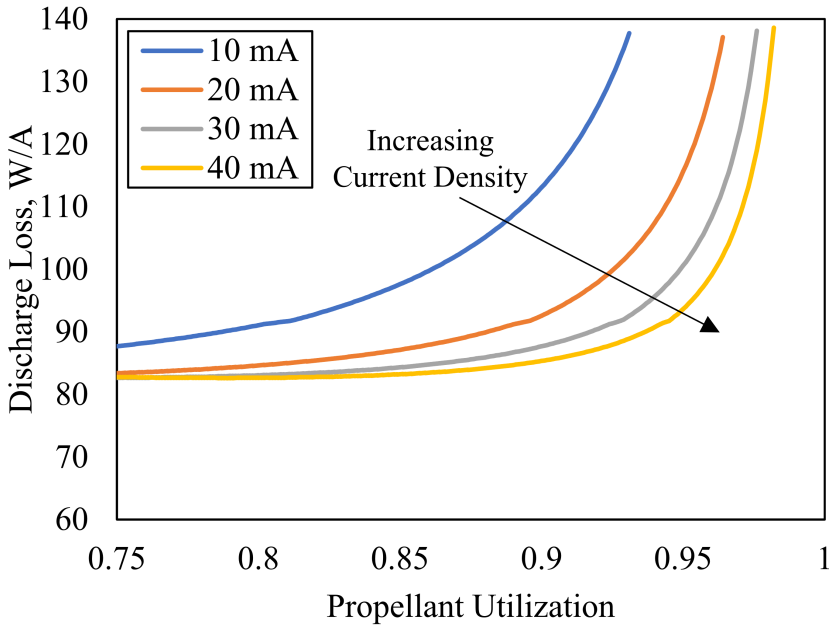

(a) Discharge Loss

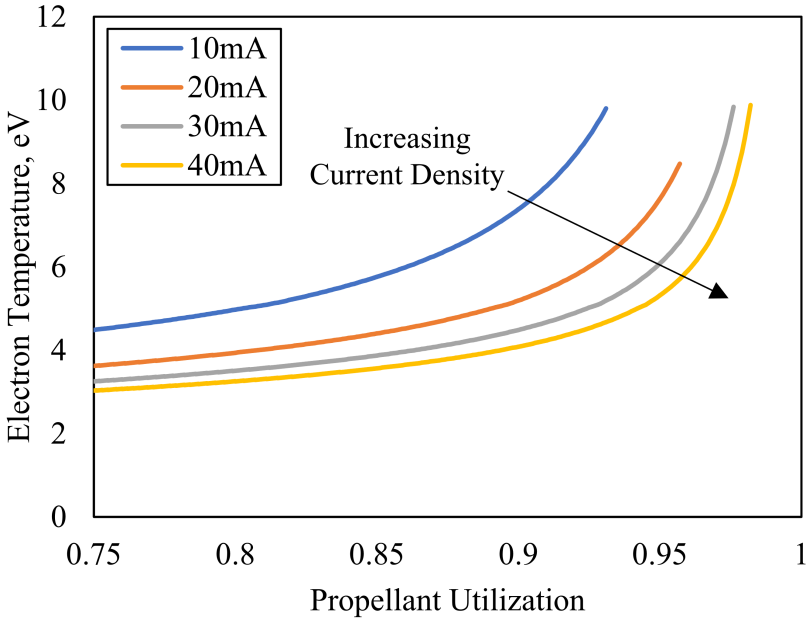

(b) Total Efficiency

Figure 4.2: Discharge loss and electron temperature as a function of propellant utilization with varying thruster beam current at a fixed 3 cm size.

plots of discharge loss were computed with varying beam current density and thruster size to quantify the magnitude of this dependency, shown in Figures 4.1 and 4.2. Even though in Eq. 4.2 the first term of discharge loss increases with increasing radius, decreasing electron temperature overpowers this, resulting in decreasing discharge loss with increasing thruster radius. This is the same with current density, increasing current density decreases discharge loss.

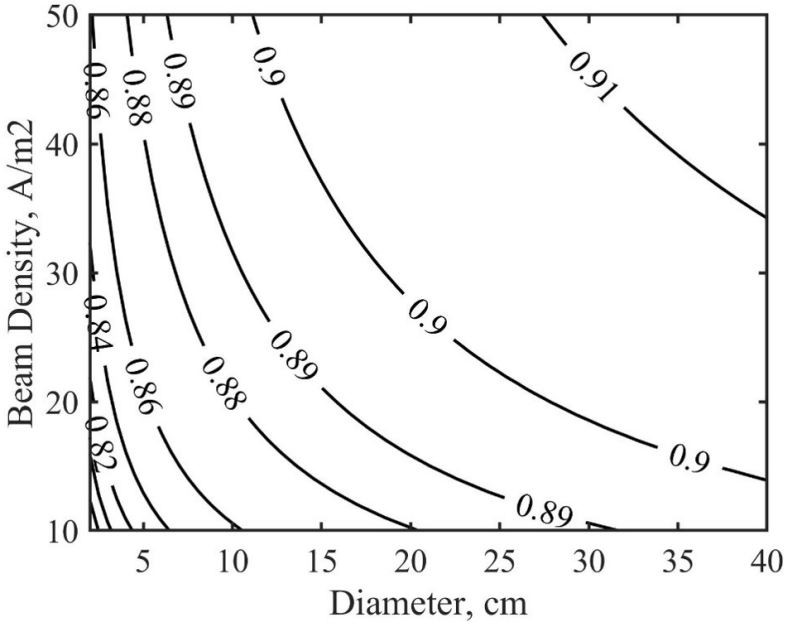

Figure 4.3: Neutralizer-free peak total efficiency of an ideal ion thruster at 1kV beam potential with varying beam density and grid diameter.

From these relations it is apparent that miniaturization of ion thrusters will result in higher discharge loss (and thus, lower efficiency) primarily due to an increase in electron temperature. This increase in discharge loss may be ameliorated by increased beam current density. To quantify this tradeoff, the peak efficiency for a thruster with a 1 kV beam has been calculated for varying values of grid radius and current density, shown in Figure 4.3. While increasing beam current density can compensate for losses due to miniaturization, for extensive miniaturization (e.g. from 30 cm to 3 cm), it is unlikely that current density can be increased to the extent needed. It should be noted, however, that the total efficiency loss

for an ideal thruster due to miniaturization is only on the order of a few percent, and that there is significant room for improvement before miniature thrusters reach this fundamental upper limit of efficiency.

4.2 Miniature Ion Thruster Testing Facility

4.2.1 Thruster Control and Measurement Electronics Rack

Ion thrusters require a relatively complicated power system, including several power supplies and additional control circuitry, to operate. A diagram of the MiXI thruster with filament cathodes is shown in Figure 4.6, which includes 6 power supplies for functions such as heating filaments, operating the discharge, biasing the accel grid and backplate, and biasing the thruster relative to the the neutralizer common. All of these power supplies are floating, i.e the inputs are not ground-referenced. As such, the power supplies' outputs must be internally floating, or the entire supply must be isolated from ground via isolation transformers. Control of floated power supplies can be performed either manually by using high-voltage isolated knobs, or via computer control through isolated digital or analog control signals. Measuring signals from the thruster requires isolation as well, as several signal sources are floated up to beam potential and are not ground-referenced. These signals are typically measured by floated multimeters and recorded by hand, or through high-voltage isolated differential inputs on a computer-controlled DAQ.

Previous testing and development of the MiXI thruster used a set of three Opto-22 DAQs with several high-voltage isolated analog in, out, and digital relay modules, connected to a computer via an isolated RS-232 interface. Initial characterization was performed with this system, but limitations in speed and software interface led to a redesign of the MiXI control and measurement electronics rack. A new system was developed using a National Instruments DAQ for native Labview integration, with all high voltage isolation occurring within a set of signal conditioning boxes. These conditioning boxes consisted of two 10-channel

motherboards with swappable isolation cards to provide either analog input (at 1x, 10x, and 100x gain), analog output, thermocouple input, or digital input signals using isolation amplifiers or optocouplers. All measurements involving high-voltage floated power supplies or components were routed through the floater boxes to provide up to 1.5kV isolation. Power supply control was achieved through analog outputs on the DAQ, routed through the floater box to analog control points on the Sorensen and Glassman power supplies. Power supply outputs were routed through a MiXI interface board, where a series of shunts and voltage dividers measure the signals going to the thruster. Sensing lines were not used, but at the low currents expected voltage drop across cabling is minimal.

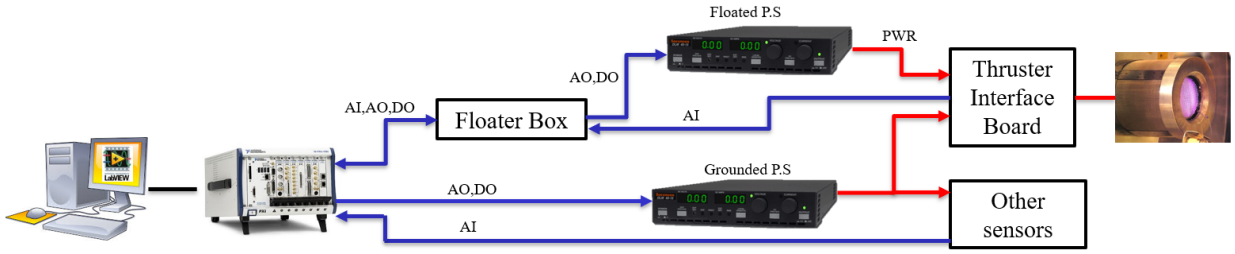

Figure 4.4: Simple diagram of MiXI control and power supply rack.

An automatic recycle system was implemented using a flip-flip circuit which measured current through a shunt and compared it to some predetermined reference current. If the accelerator grid current exceeded a threshold, the system interrupts the enable lines for the accel and beam power supplies. The recycle state is sent to Labview via a digital pin, and the system can be reset by an input pin once the recycle procedure is completed.

4.2.2 LabView Control Software

The thruster power supply control and measurement rack was controlled by a Labview VI, which performs power supply control, signal measurement, data recording, as well as automatic recycle cutback routines. The VI is based on a Queued Message Handler architecture to enable expansion and prevent issues with race conditions sometimes experienced with

Figure 4.5: HV isolation "Floater" box. Two such boxes with red digital out, blue analog out, and green (not pictured) analog in cards form the core of the MiXI control and measurement rack.

simple loop VIs.

4.3 MiXI(ARCH) Performance Characterization with Beam Extraction and Filament Cathodes

The objective of this work was to obtain beam extraction for the MiXI thruster while using the ARCH discharge, and identify pathways for further improving performance. The MiXI thruster and it's associated discharges is described in Sec. . Filament cathodes were used to maintain commonality with previous works [23, 52, 1], and for ease of testing. This experimental campaign was a parallel effort with computational work presented by Li et al. [53], using DC-ION to computationally investigate the discharge processes within the MiXI(ARCH) thruster.

4.3.1 Experimental Setup

Testing was conducted at the UCLA Plasma & Space Propulsion Lab's MiXI Test Facility. The 20" diameter by 36" tall bell-jar chamber is equipped with a 7" cryopump which allows for a base pressure of 2×10^{-6} Torr and an operational pressure of 5×10^{-5} Torr with 0.5 sccm Xe flow. A thermocouple is located on the outer anode holder ring to measure thruster temperature. Figure 4.6 shows the power supply configuration for the thruster, including the backplate power supply switch, which is used to bias the backplate positive to cathode common for startup, and negative for operation. This is necessary because the ARCH discharge design provides no direct paths for primary electrons to connect to the anode, and relies on the more collisional plasma electrons to carry current across field lines. Current measurements were obtained using calibrated shunt resistors rather than output readouts of power supplies for accuracy. A 4 mm diameter unshielded molybdenum Faraday probe was used 11 mm above the accelerator grid for verifying the beam current as measured by the shunt resistor. The probe was biased to -60 V, corrected for iSEE yield at 1 kV, and swept across the plume using a Velmex stage to measure beam current density across the plume. The current density was then fit to a symmetric profile and integrated radially to

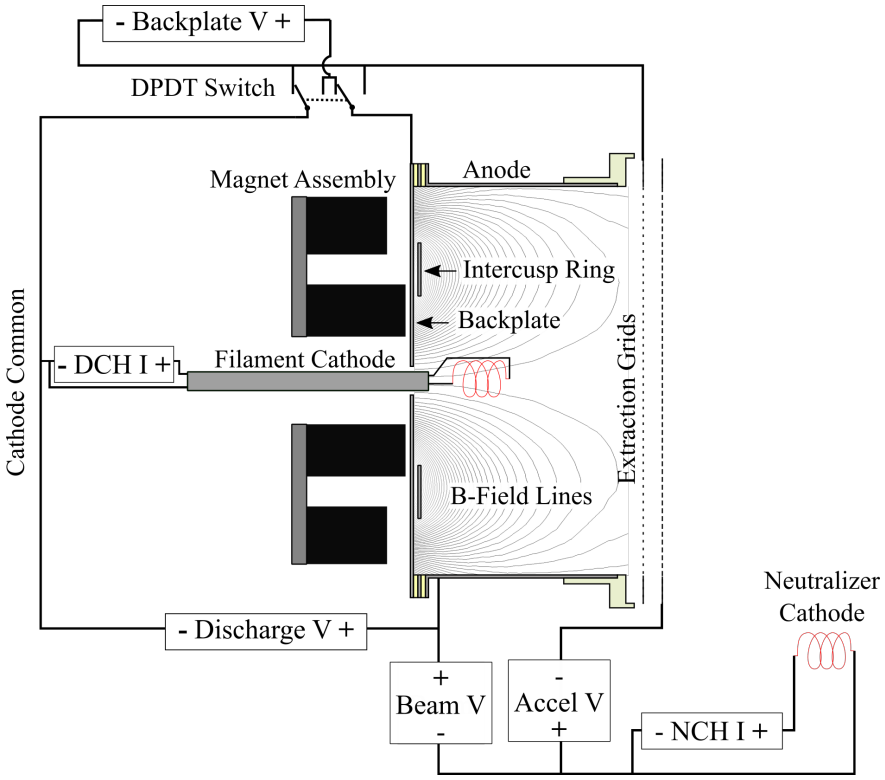

Figure 4.6: MiXI(ARCH) electrical diagram detailing power supply connections to electrodes. The DPDT relay is used to bias the backplate above cathode common as a secondary anode for discharge ignition.

compute total beam current I_b. This measurement agreed with shunt-measured values to within 10%. The thruster was operated using 0.005" tungsten filaments for the discharge and neutralizer cathodes. The discharge current I_d was controlled by changing the filament heater current at a constant discharge voltage.

4.3.2 Operation

For beam extraction, the thruster was operated at a beam voltage V_b of 1 kV, accelerator voltage V_a of 50 V, a discharge voltage V_d of 25 V, and with the backplate and screen grid biases (V_{bp} and V_s) set to 10 V below cathode common. Accelerator voltage was high enough such that neither further increases nor minor decreases decreased beam current, i.e. there is voltage margin. Xenon gas was injected into the discharge chamber through injection holes

at the outside edge of the backplate. To obtain propellant utilization, the flow reported by the Apex mass flow controllers (which assume 25 °C, 14.969 psia STP) was converted to effective current in mA, similar to the calculation in Appendix B of Goebel and Katz [22]. The MiXI thruster was initially run cold, sweeping from a discharge current of ∼300 mA down until the propellant utilization reached below 30%. The thruster was then left on until it reached thermal steady state, and further datapoints were taken. Hot and cold conditions were examined to determine performance trends. In flight, better thermal management and a hollow cathode will be used which will likely generate significantly less heat than a thermally unoptimized filament cathode (18 - 25 W). The thruster was run at constant gas flow rather than at constant beam current, so the discharge curves presented are not those typically reported for ion thruster performance. While constant gas flow curves are not reported as commonly as constant beam current, they still give insight into the thruster's total achievable efficiency. During this cold sweep the thruster would increase from the ambient temperature of 25 °C to ∼100 °C due to the setup's high thermal insulation and heat injected by the filament and discharge. Once the thruster reached thermal steady state between 300 and 380 °C, more performance curves were measured to determine sensitivity to various operating parameters such as gas flow and electrode voltages. The magnets' aft position and their detachment from the aft backplate results in significantly lower magnet temperatures than the anode, therefore, magnet temperatures were sufficiently cool such that demagnetization was not observed during the tests presented here.

4.3.3 Beam Extraction Results and Comparison with Past Works

Results obtained for MiXI(ARCH) with beam extraction are presented in Figures 4.7(a) and 4.7(b) along with data for the MiXI(3-Ring) configuration [1, 23] and simulated beam extraction (Sim Beam) data for MiXI(ARCH) [52]. The MiXI(ARCH) thruster achieves a maximum efficiency of 59% at 23.7 mA with 0.5 sccm xenon, 1 kV beam potential, and a cold thruster, with a discharge loss and propellant utilization of 226 W/A and 0.72 respectively.

This is slightly greater efficiency than the previously reported MiXI(3-Ring) performance of 56% at 28.3 mA, but less than that of the MiXI(ARCH) configuration with simulated beam extraction, which predicts greater than 60% at 24 mA beam current. MiXI(ARCH) with beam extraction has a lower discharge loss at the knee of the curve than MiXI(3-Ring), but at a lower propellant utilization. As discussed in [52], variations in plasma properties at the extraction plane between simulated and actual beam extraction with the ARCH discharge may violate assumptions typically made for simulated beam extraction [54]. A discussion on the effects of thruster total efficiency and other parameters on a high ΔV CubeSat mission may be found in Sec. 3.4.

4.3.4 Performance Trends with Propellant Flow Rate

Performance plots for a variety of flow rates are presented in Figure 4.8. Performance was characterized at thermal steady state with the standard 0.5 aspect ratio anode. Higher flow rates correspond to higher maximum achievable efficiencies, with MiXI(ARCH) at thermal steady state (320 °C) achieving 53% efficiency at 0.8 sccm versus 45% for 0.5 sccm. At 0.4 sccm, the discharge was unstable when pulling beam in the standard configuration and therefore required the backplate to be used as a secondary anode biased 10 V above cathode common, resulting in high discharge losses. This indicates that the total efficiency of MiXI(ARCH) may continue to increase at higher power levels, suggesting that the ARCH discharge may further increase efficiency in the 30-60 W range, but may be limited for lower powers.

4.3.5 Performance Trends with Anode Aspect Ratio

Discharge chambers with aspect ratios of 0.4, 0.5, and 0.75 were manufactured and characterized to determine the influence of anode area on discharge performance. Aspect ratio is defined as the discharge chamber height over the diameter, which is held constant. Dis-

charge loss and efficiency curves were obtained at 0.5 sccm propellant flow, thermal steady state, and 25 V discharge voltage, and are presented in Figure 4.9. As seen in Figure 4.9(b), the shorter anode performs at a higher efficiency than the longer anodes, but requires slow ramping of beam voltage over several minutes (approximately 200 V / minute) and only operated reliably above 0.5 sccm. A reduced plasma volume may increase sensitivity to sudden boundary condition changes, leading to unstable operation. Lengthening the anode increased stable operation but resulted in decreased efficiency. This increase in stability is expected because lengthening the discharge chamber increases anode area, trading efficiency for stability by preventing impedance shift instabilities from overconfinment of the plasma [3]. The present results demonstrate the commonly observed tradeoff between efficiency and stability for small DC ion thrusters [8].

4.3.6 Performance Trends with Discharge Voltage

MiXI was operated at varying discharge voltages to determine the effect of discharge voltage on overall efficiency. Data was taken with the standard MiXI aspect ratio of 0.5, with 0.5 sccm input propellant flow and thermal steady state unless otherwise noted. Results are presented in Figure 4.10. Increased discharge voltage did not increase efficiency at lower propellant utilization, but rather shifted the knee of the discharge curve to the right, increasing maximum achievable propellant utilization. This trend was also seen with decreasing temperature, where decreasing temperature at 25 V from 350 °C to 100 °C increased maximum efficiency from 45% to 59%, while increasing voltage from 25 V to 35 V increased peak efficiency from 45% to 54%. Future spacecraft integration will need to consider the temperature effect on efficiency when performing thermal analyses, as thruster temperature has a strong effect on efficiency. If the thruster temperature can be lowered to below 100 °C through appropriate thermal management or cooling fins, efficiency may be even further improved.

4.3.6.1 Anode Temperature

In terms of total efficiency, lowering discharge chamber wall temperature increases propellant efficiency because of lowered neutral flux out of the grids at a set neutral density. Using Equation 2.4, neutral mass flow out of the grids is proportional to $T^{1/2}$. From ambient to a 350 °C thermal steady state the neutral loss increases by 40% assuming a constant neutral density in the chamber. The effect of neutral diffusion on propellant utilization can be estimated using the input propellant flow and expected neutral diffusion. Assuming a 0.5 sccm input, 5% grid neutral transparency, and 5e19 m^{-3} neutral density, a temperature increase from 25 °C to 350 °C corresponds to a neutral outflow increase from 0.15 to 0.2 sccm, or a decrease in propellant utilization of 12%. Thus, the decrease in propellant utilization at higher temperatures can be explained by an increased neutral diffusion through the grids. With a filament cathode, a significant portion of the power deposited in the discharge chamber (up to 75%) is due to the filament heater, which is expected to be minimized with future, thermally optimized hollow cathodes. This is the reason the cold temperature is reported as the peak efficiency rather than the thermal steady state value.

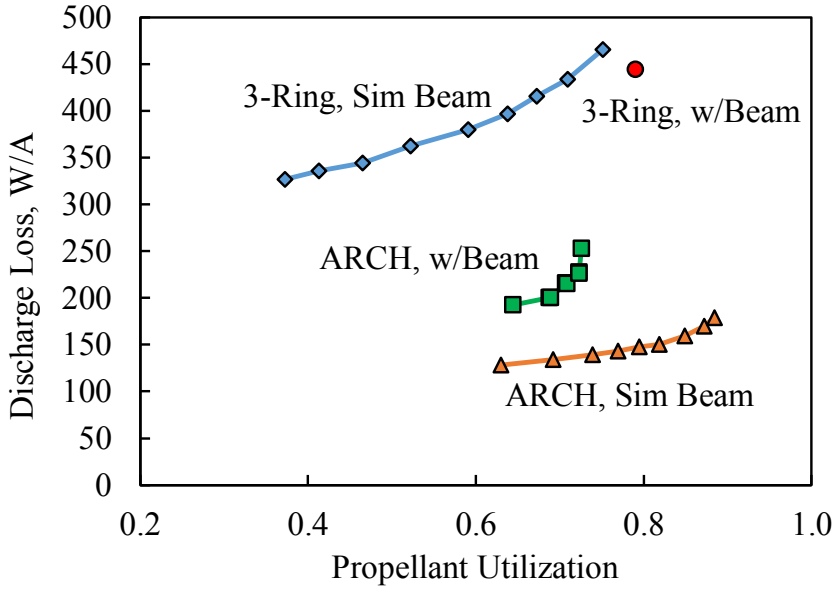

(a) Discharge Loss

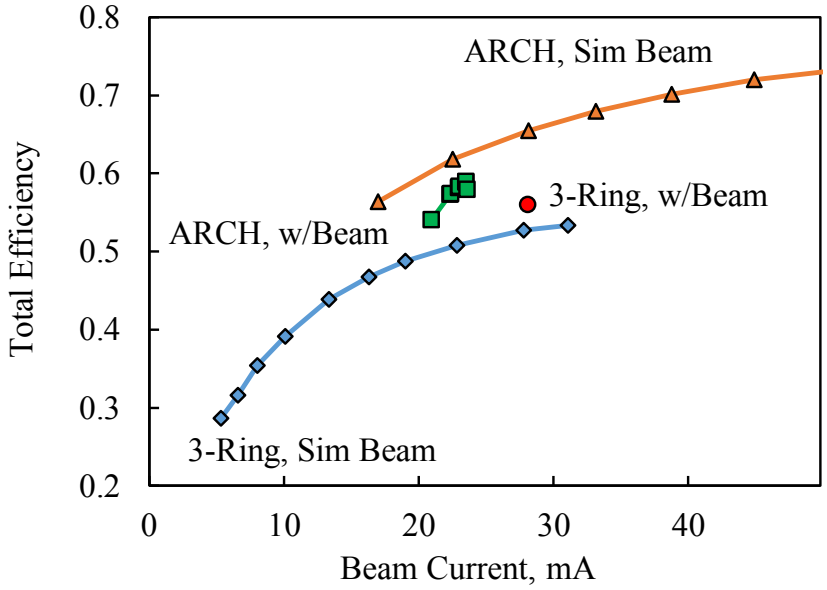

(b) Total Efficiency

Figure 4.7: Discharge loss and total efficiency as a function of propellant utilization and beam current for MiXI ARCH and 3-Ring discharges with both simulated beam extraction and beam extraction. Beam extraction curves were taken with constant 0.5 sccm flow and 1 kV beam voltage.

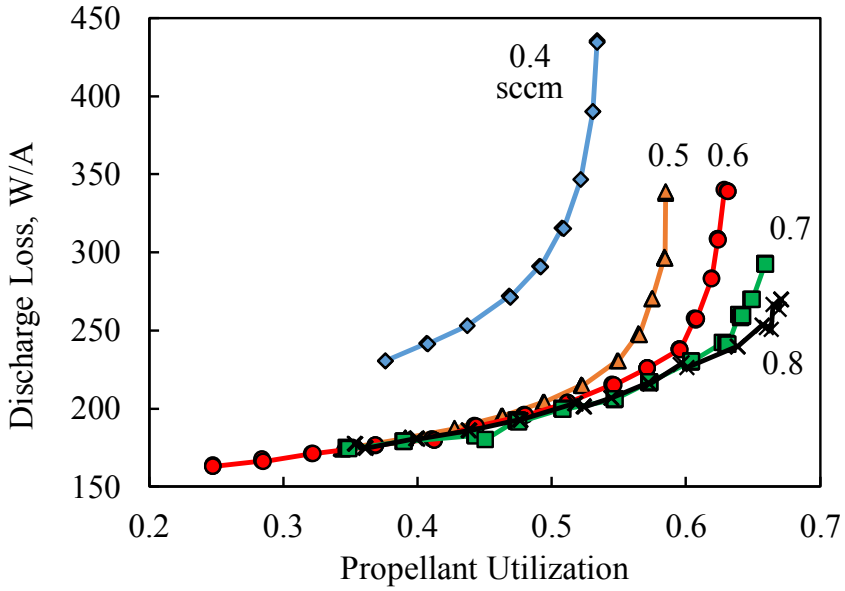

(a) Discharge Loss

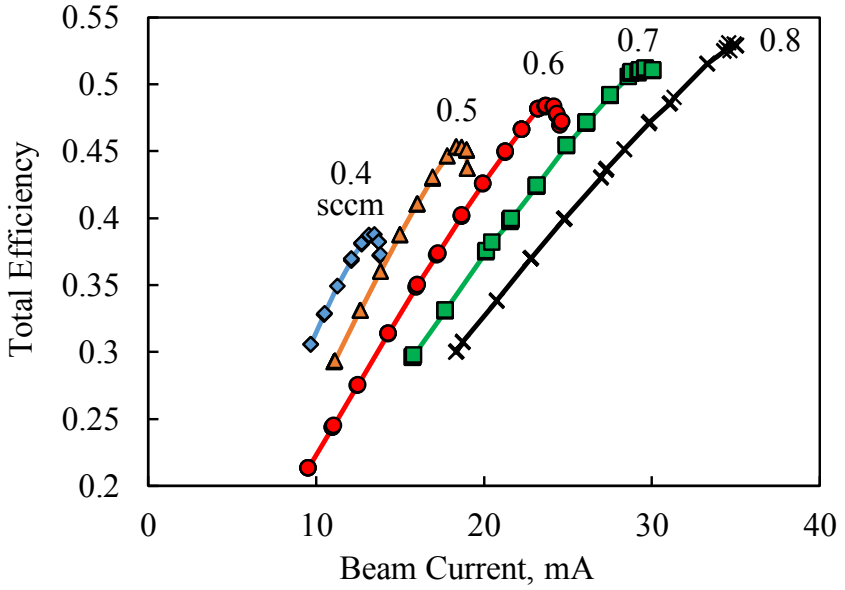

(b) Total Efficiency

Figure 4.8: Performance plots for varying input propellant flow rate. The 0.4 sccm case deviates at low utilization because of an altered electrode configuration due to operating instability. Total efficiency is calculated with a 1 kV beam voltage.

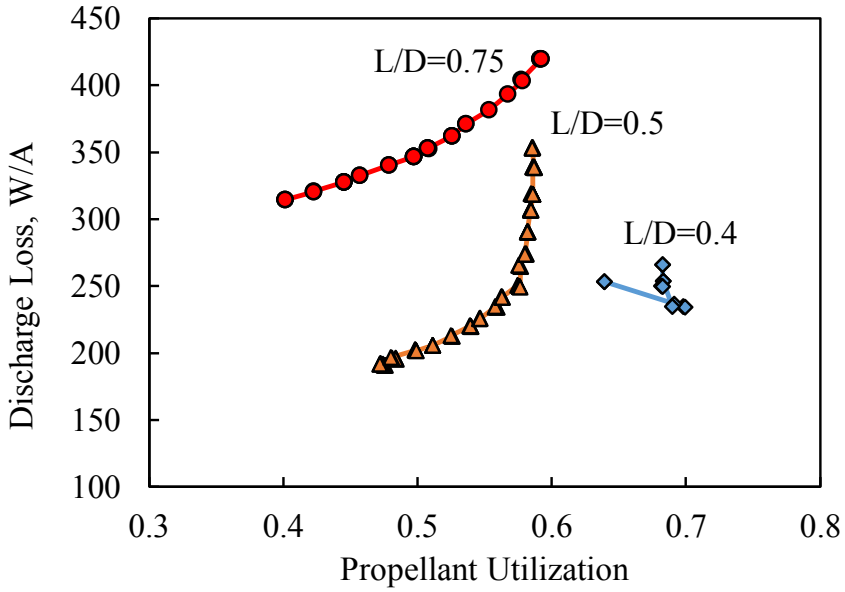

(a) Discharge Loss

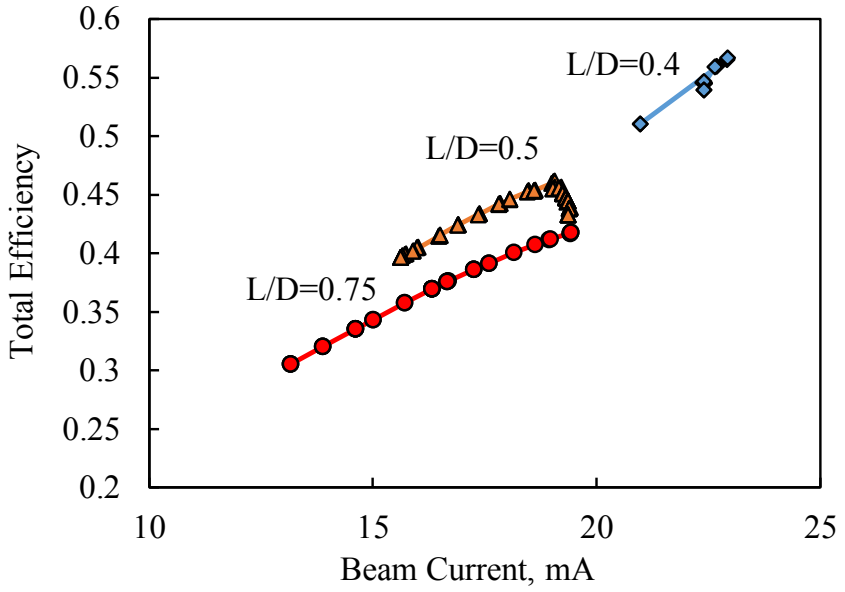

(b) Total Efficiency

Figure 4.9: Performance plots for varying anode aspect ratios, with diameter held constant. Data taken at 0.5 sccm, thermal steady state, and 25 V discharge voltage.

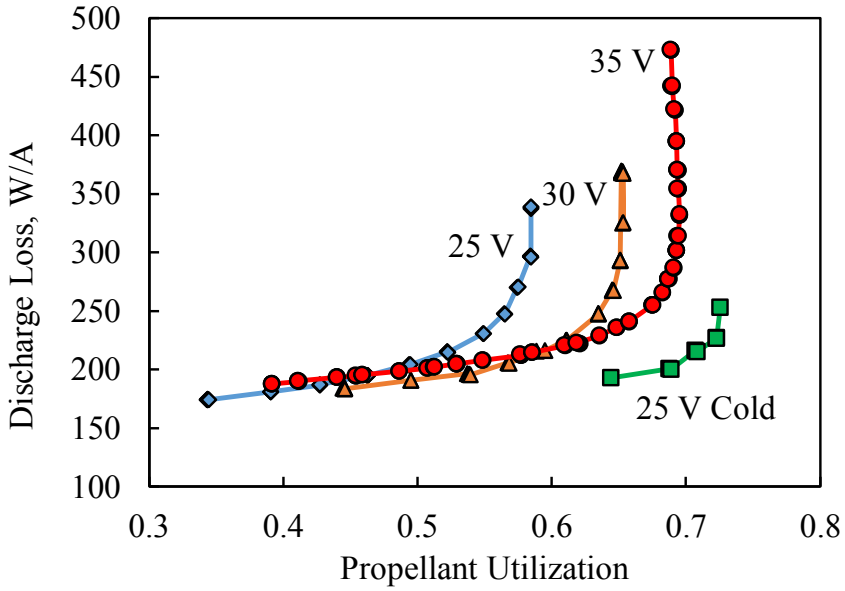

(a) Discharge Loss

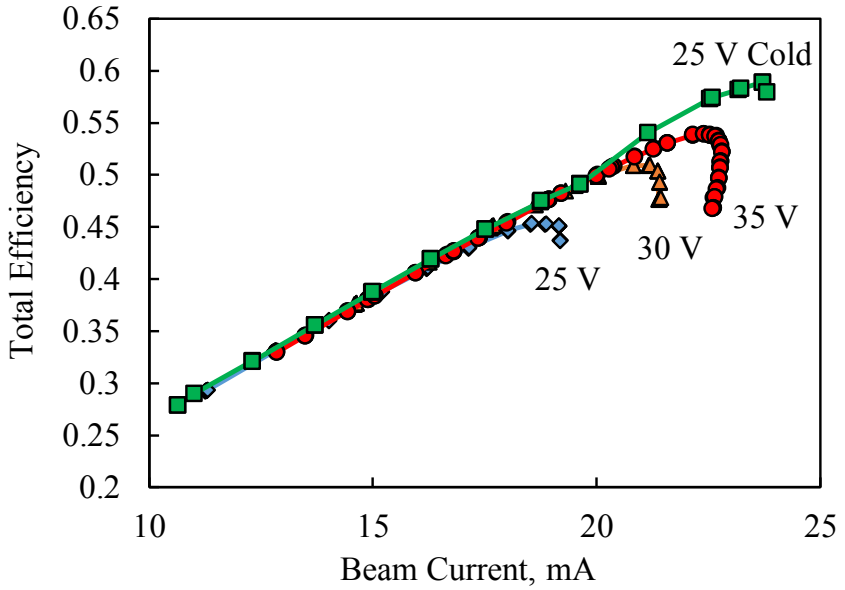

(b) Total Efficiency

Figure 4.10: Performance plots for varying discharge voltages. Data taken with aspect ratio of 0.5, 0.5 sccm input flow, and thermal steady state. Data from 25 V cold case is also shown.

4.4 Analytical Modeling of MiXI(ARCH)

The single-cell model as described in Section 2.3 was used to investigate trends observed during the performance testing. The MiXI geometry and magnetic fields were used as inputs. All cusps in the MiXI(ARCH) configuration are cathode-terminating, but some fraction of primaries incident to these cusps were assumed to be lost. This fraction, along with an assumed neutral leak rate, were used as fitting parameters to fit the resulting curve to the experimentally measured 0.5 sccm, 0.5 aspect ratio, thermal steady state performance data. A leak rate was assumed to account for uneven plasma profile at the grid plane, a possible leak path from the rear plenum circumventing the discharge chamber, and the flow path between the grids circumventing the accelerator grid. These resulting parameters were then used across all cases to investigate trends seen in the data.

4.4.1 Comparison with Measured Data

As shown in Figure 4.11, the single-cell model returns a trend of improved performance with increasing flow, similar to the experimentally measured trend. From 0.5 sccm to 0.8 sccm there is a predicted increase in total efficiency from 45% to 57%, compared with the measured increase of 45% to 53%. The beam current at which peak efficiency is achieved is also similar between model and experiment.

The model does not fully capture the trend seen in the aspect ratio study, as shown in Figure 4.12. The model returns a decrease in efficiency from aspect ratio of 0.5 to 0.75, but the magnitude of the change is significantly different than experimental data. The trend of increasing total achievable beam current with decreasing aspect ratio seen in experiments was not captured by the model. Decreasing efficiency with increasing aspect ratio is due to increasing anode area and chamber volume, which increases power losses to the anode and to excitation, both phenomena captured by the model. The increase in total achievable current for the L/D=0.4 case may be due to structural changes in the plasma which are not

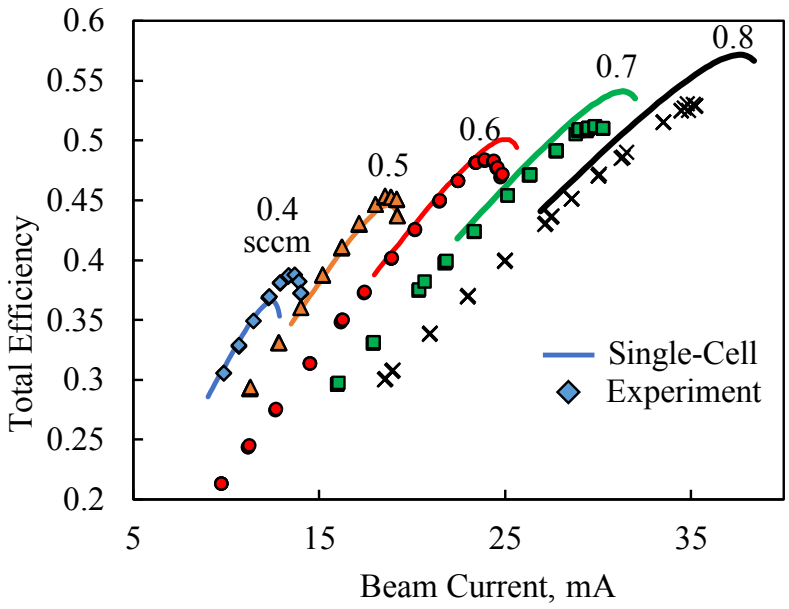

Figure 4.11: Flow study data from Figure 4.8(b) with results from single-cell model. Model parameters were taken from MiXI geometry and measured values. Primary reflection coefficient and neutral leak rate were fitted to the 0.5 sccm case and held constant for all other cases.

captured by a single-cell model, but may be captured using a spatial plasma model such as DC-ION [55]. As previously noted, the 0.4 case was characterized by unstable operation, with the thruster discharge regularly dying. This may be due to two factors: a decrease in anode area, which increases efficiency while simultaneously decreasing sheath potential, and an increase in average magnetic field with decreasing chamber height (due to the magnets being located at the read end of the chamber), which has the same effect. A discussion on the effect of increasing average B-field strength on efficiency and stability is found in Sec. 4.4.3.

The trend of increasing maximum achievable beam current with increasing discharge voltage as observed in Figure 4.10 was also not captured by the model, which simply predicted a 1% increase in maximum efficiency from 25 V to 35 V (shown in Figure 4.13). Because the propellant utilization at the peak efficiency point of the discharge curve increases with

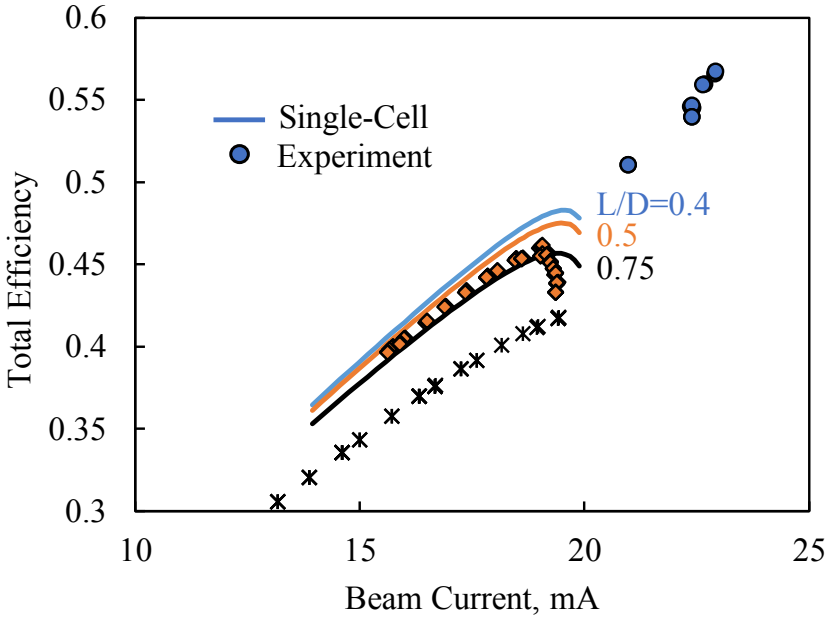

Figure 4.12: Flow study data from Figure 4.9(b) with results from single-cell model. Model parameters were taken from MiXI geometry and measured values. Primary reflection coefficient and neutral leak rate were fitted to 0.5 sccm case, and held constant for all other cases.

increasing voltage in experiment but not the single-cell model, the previously assumed leak rate may partly result from plasma structure effects such as uneven grid-plane plasma density. Future measurements will explore this by recording internal plasma parameter maps as a function of propellant utilization.

4.4.2 Internal MiXI Parameters and Loss Mechanisms

Plots for the internal plasma parameters of the MiXI thruster as calculated by the single-cell model are shown in Figure 4.14. Plasma density remains relatively constant with increasing propellant utilization until the knee of the discharge curve where it begins to decrease rapidly. Primary electron density and electron temperature both exhibit the $\eta_p/(1-\eta_p)$ behavior first reported by Brophy [54]. Sheath potential also tracks electron temperature, remaining at approximately $T_e/2$. One interesting note is that for constant gas flow operation, because the

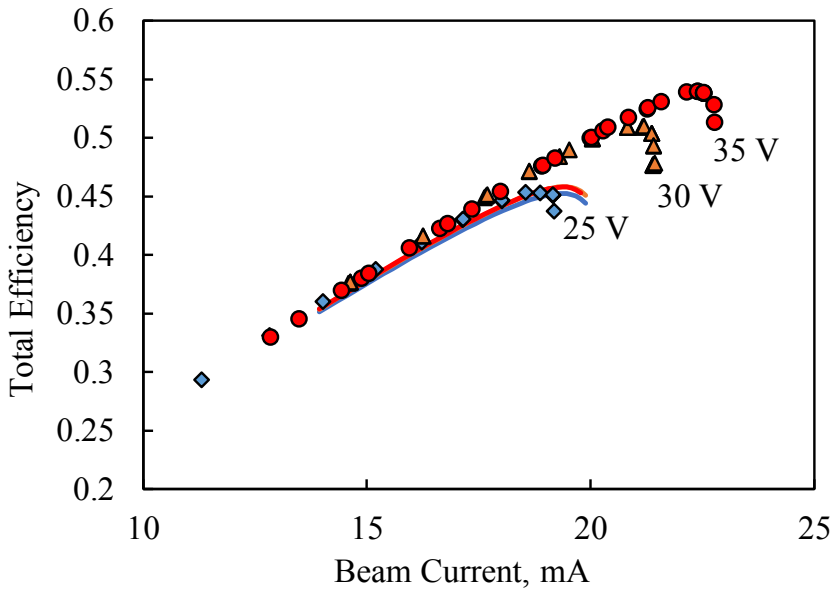

Figure 4.13: Discharge voltage study data from Figure 4.9(b) with results from single-cell model. Model parameters were taken from MiXI geometry and measured values. Primary reflection coefficient and neutral leak rate were fitted to 0.5 sccm case, and held constant for all other cases.

beam current is assumed to be Bohm current to the grids, the increase in beam current with increasing propellant utilization is primarily due to an increase in electron temperature rather than an increase in plasma density. As seen in Figure 4.15, the majority of ion generation is due to primary electrons, however plasma electrons also contribute to ionization indicating good confinement and transfer of energy from primaries to the bulk.

Loss mechanisms are presented in Figure 4.16. The dominant loss factors are ionization, excitation, and electron current to the anode. Increasing propellant utilization increases discharge loss as seen in Figure 4.7(a). Electron temperature and sheath potential both increase exponentially and are related to anode power loss through Equation 2.48. This could be mitigated by increasing magnetic field strength, but increased magnetic field strength decreases stability due to impedance shift instabilities [2]. Current to the rear backplate and intercusp ring were minimal in the single-cell calculation, and backplate current was measured to be

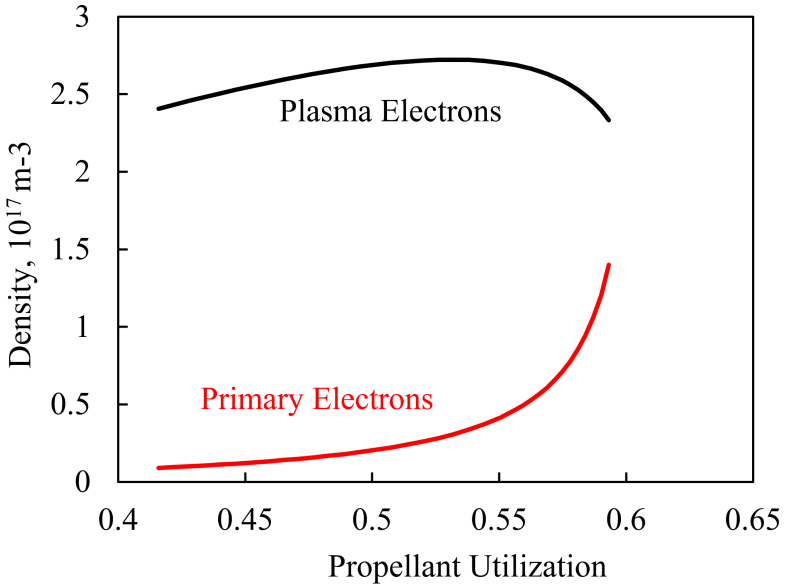

(a) Discharge Loss

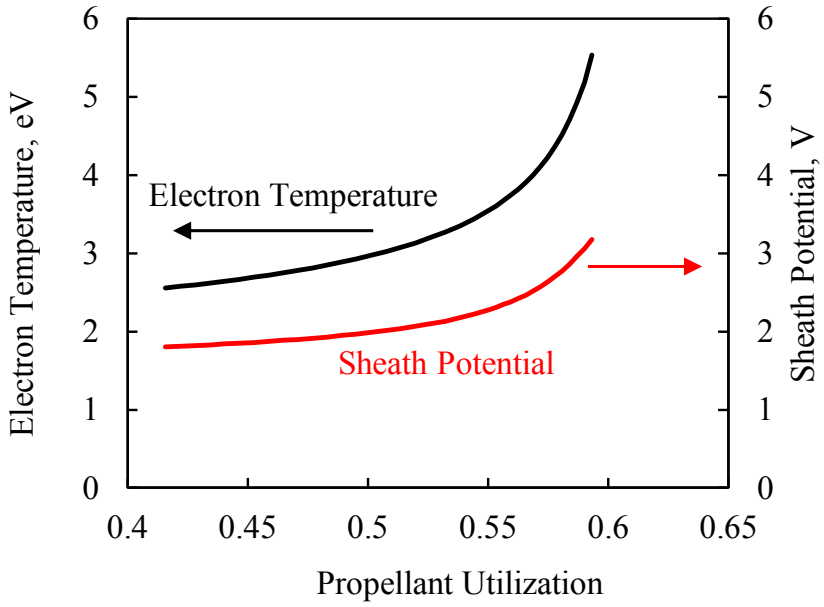

(b) Total Efficiency

Figure 4.14: Single-cell calculated internal plasma parameters for MiXI(ARCH) thruster as tested with L/D=0.5 anode, 0.5 sccm flow, and thermal steady state.

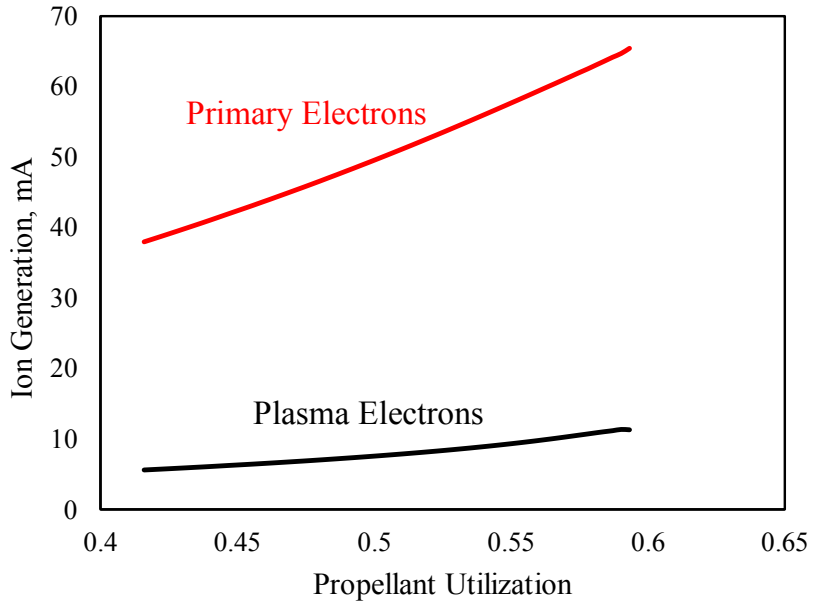

Figure 4.15: Ion generation rate due to ionization by primary electrons and plasma electrons. The bulk of ionization is caused by primary electrons, however plasma electrons do contribute to ionization due to their high temperature.

minimal during testing. These single-cell results give insight into the internal processes of the MiXI thruster during operation and give important information as to potential avenues for further improvement.

4.4.2.1 Predicting Hollow Cathode Performance Using Cathode Drop V_c

Future efforts will include integration of hollow cathodes in the discharge. Here we discuss considerations of the effects of the hollow cathode on the discharge and the overall performance. Measurements of the insert plasma potential inside hollow cathodes [56] have indicated a range of plasma potentials at the orifice from 6 - 10 V relative to cathode common for the NSTAR discharge cathode depending on throttle level. Measurements on a separate BaO cathode [57] with a 2.75 mm diameter orifice exhibited plasma potentials at the orifice of between 10 and 24 V for cathode flow rates ranging from 5.5 to 10 sccm of xenon and currents of 10 to 25 A. To predict the effect of cathode voltage drop V_c on total thruster per-

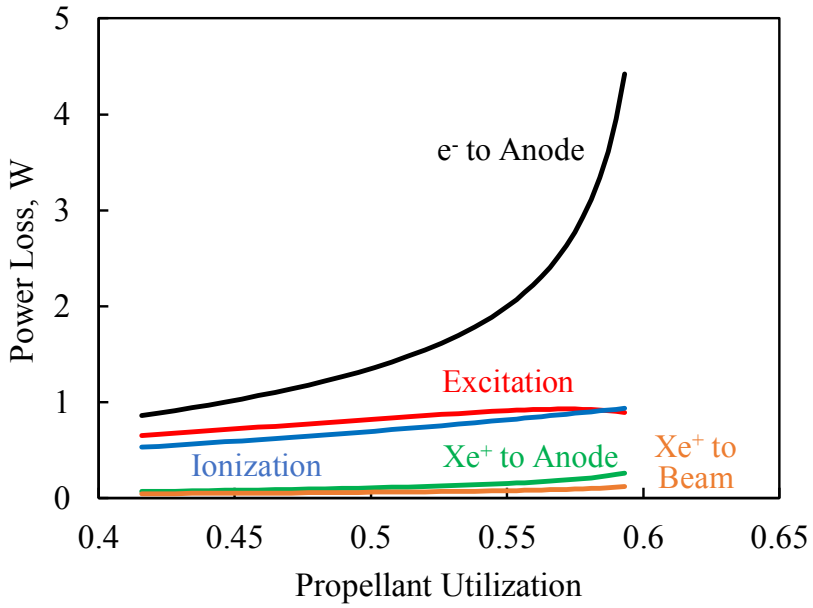

Figure 4.16: Power dissipation in the MiXI(ARCH) configuration. Ionization and excitation are loss mechanisms due to plasma properties and independent of geometry. Power deposition to electrodes is the power loss minimized by magnetic shielding, but increasing shielding increases the risk of instabilities generated through sheath inversion [2].

formance, the standard 0.5 and 0.8 sccm single-cell cases were run with the cathode voltage drop swept from 4 to 12 V. This assumes identical geometry to the MiXI(ARCH) thruster, but with no neutral leakage at the grids. Discharge loss curves for constant gas flow of 0.5 sccm and 0.8 sccm are shown in Figure 4.17. As expected, increasing cathode voltage drop increases discharge loss, and decreases the propellant utilization associated with the knee of the curve. This increase in discharge loss is predominantly due to a decrease in primary electron energy, which decreases the ionization rate due to the primary electrons. Increasing the flow from 0.5 sccm to 0.8 sccm slightly lessens this increase in discharge loss. At 0.5 sccm, increasing the cathode drop from 4 V to 10 V results in the discharge loss at the knee increasing from 259 to 380 W/A, an increase of 47%, while at 0.8 sccm the discharge loss is increased from 243 to 351 W/A, an increase of 44%. Based on these results, in forthcoming hollow cathode design and integration efforts we aim to operate at lower values of cathode

drop V_c to yield desirable discharge performance.

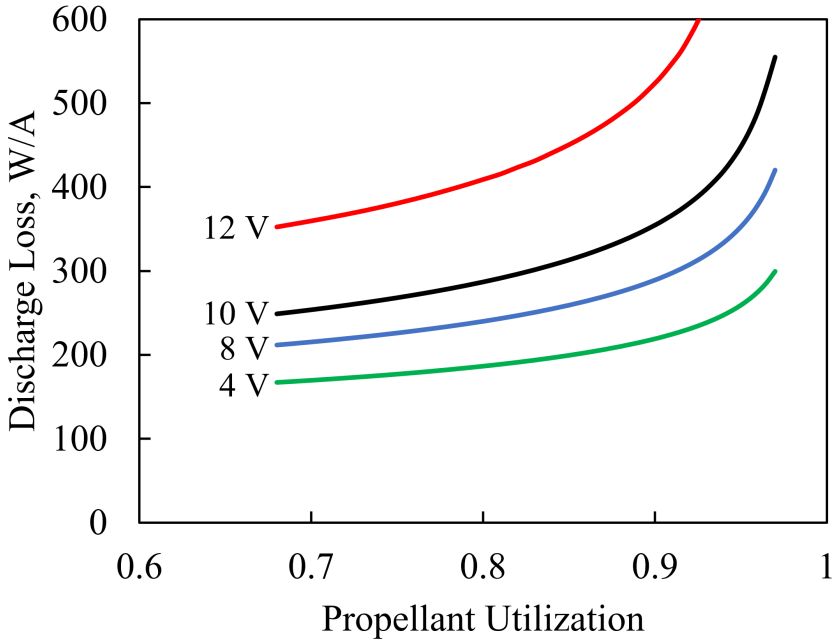

(a) 0.5 sccm

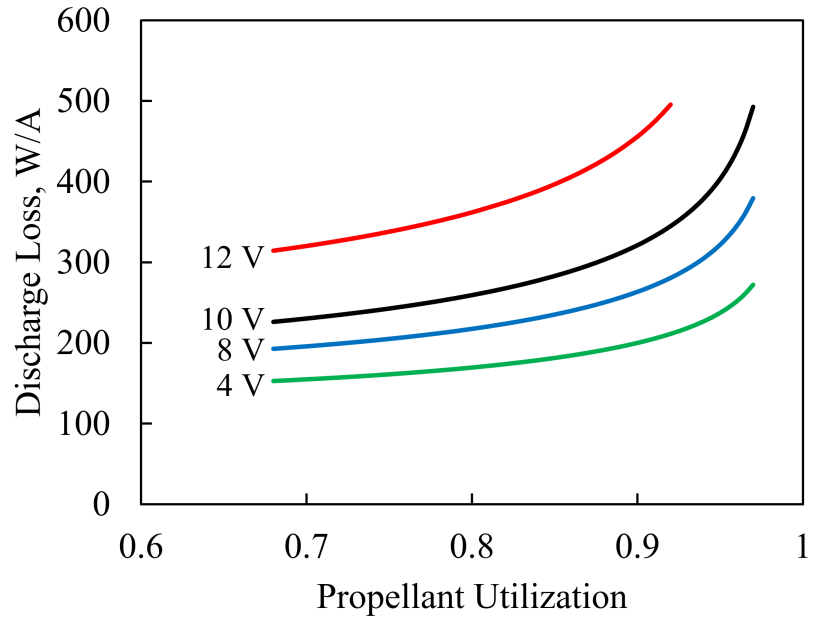

(b) 0.8 sccm

Figure 4.17: Single-cell calculated discharge loss plots for increasing cathode voltage drop at both 0.5 sccm and 0.8 sccm input propellant flow. The increase in discharge loss is only slightly lessened by increase in propellant flow.

4.4.3 Magnetic Overconfinment and Performance with Varying B Fields

Because one of the main loss mechanisms in ion thrusters is electron current to the anode, it is tempting to simply "crank up" the magnetic field to more completely confine the plasma and increase efficiency. While increased magnetic fields at the anode do improve performance by more fully confining primary electrons and plasma to a point, there is a point at which the plasma will become "overconfined", and undergo an impedance shift instability where the sheath potential goes negative. This instability is due to an insufficient anode area for a given current and plasma density, in order to drive more current into the anode, the sheath can become inverted, creating a potential structure which accelerates electrons into the anode rather than repelling them. A diagram of the resulting voltages is shown in Figure 4.18. To understand this phenomena in MiXI(ARCH), the single-cell model was run with the input magnetic field being some varying multiple of the measured magnetic field. Plots of the sheath potential ϕ are given in Figure 4.19. With increasing magnetic field, the sheath potential over the span of propellant utilization drops, and at some point becomes negative. Because the model was formulated assuming a positive sheath, no conclusions can be made about values below zero other than that they are below zero. At the measured magnetic field in MiXI(ARCH), the model predicts that the thruster is at the edge of stability, where some values of propellant utilization push the sheath potential negative. Increasing the magnetic field any higher than this results in an unstable thruster, and decreasing the magnetic field decreases efficiency. This prediction of low to near-zero sheath voltage in MiXI(ARCH) is corroborated by internal probing performed by Dankongkakul and Wirz [52] which showed a plasma potential very close to the discharge voltage.

This implies that further increases in discharge efficiency through globally increasing magnetic field strength may not come to fruition, as stronger magnetic fields will decrease thruster stability. This does not, however, preclude any and all efficiency increases in the discharges. There are several routes which can be explored for further efficiency improvements. Tailored B-field tweaks, which affect only certain regions of the field may improve primary

confinement while maintaining the necessary plasma current to the anode. Operating at higher neutral gas density and higher beam current have been shown to increase efficiency, although increase the total power of the thruster. As shown in Figure 4.17, improvements in discharge cathode performance have a strong effect on discharge efficiency, and are currently the primary candidate for improving MiXI performance. Geometric tweaks, as investigated in [5], may have 2D/3D effects that improve discharge performance as well as beam flatness and plume properties. In all, there are several routes for further improvement in discharge efficiency without sacrificing thruster stability. Several are open to investigation using 0D tools such as the control volume method described here, while others require 2D or 3D computational codes or experimental analysis.

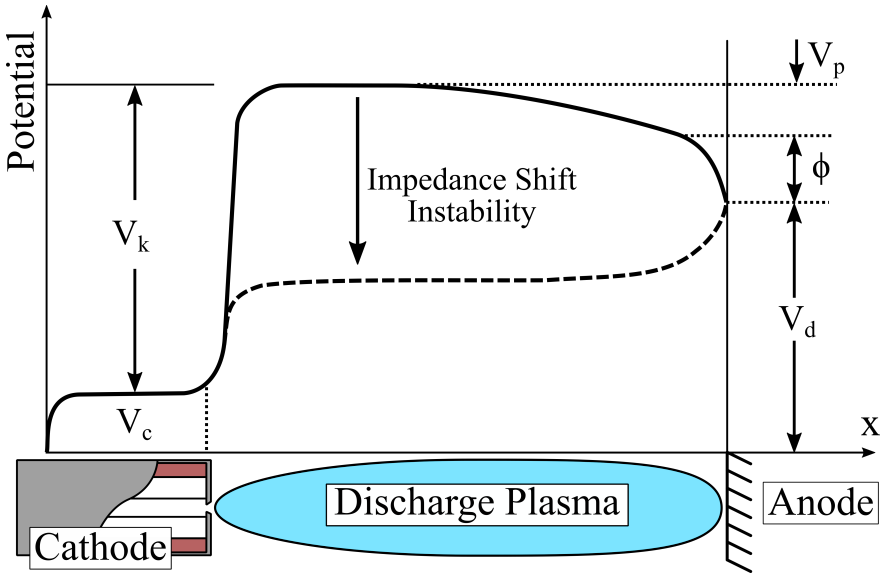

Figure 4.18: Voltages within an ion thruster discharge, with a sheath inversion event. The sheath potential phi goes negative, resulting in a plasma potential below that of the discharge voltage.

4.4.4 Limitations of an Analytical Model for Small Ion Thrusters

The use of a single-cell model requires several assumptions of the discharge plasma and thruster which warrant discussion. The primary assumption is that of spatially averaged

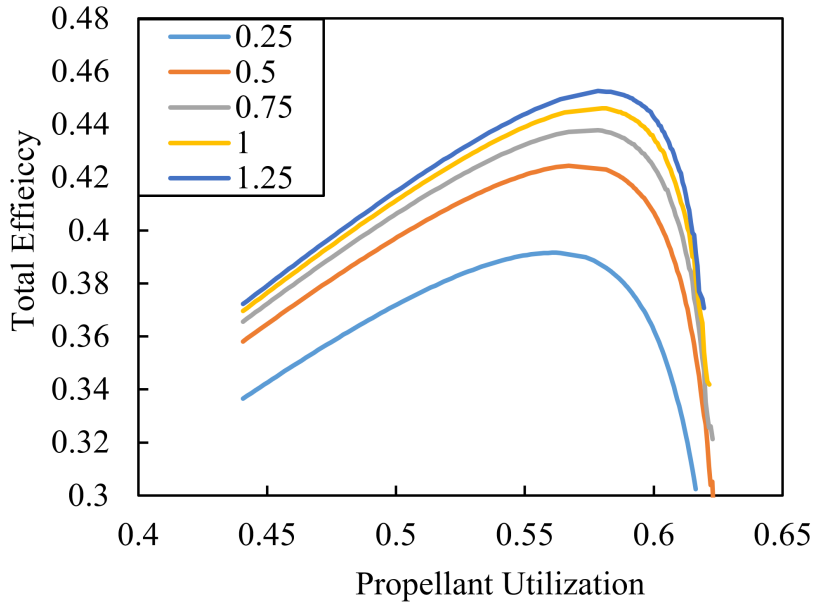

(a) Total Efficiency

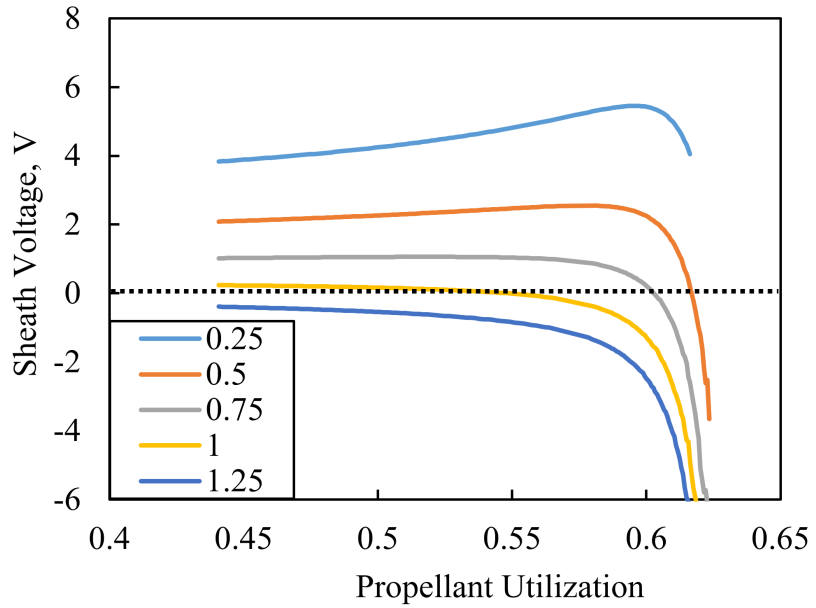

(b) Sheath Potential

Figure 4.19: Control volume analysis results of sheath potential with varying B-field. Legend is magnetic field strength multiplier applied on the measured value.

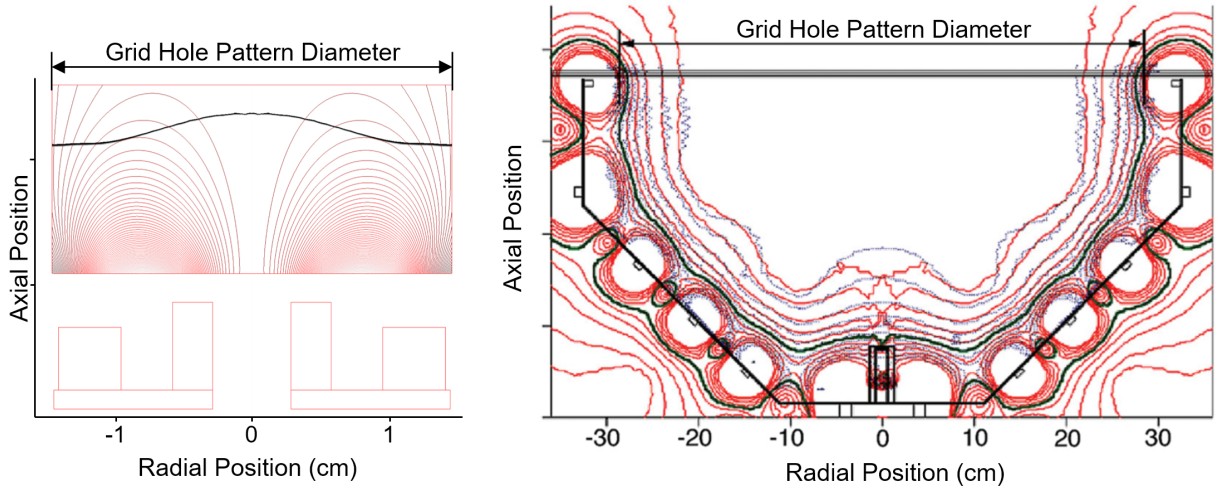

Figure 4.20: Magnetic field lines for MiXI(ARCH) (left) and NEXIS (right). NEXIS plot taken from [3]. A 60 G contour is shown for both, indicating that the majority of MiXI volume is high magnetic field strength, while the majority of NEXIS can be considered "field-free".

plasma properties, that the bulk plasma region can be treated as a single homogeneous plasma slab with some set properties. This assumption is typically made for large ion thrusters with large field-free regions, which result in large volumes of relatively unmagnetized plasma. Although MiXI has been shown to have a relatively uniform central bulk region near the grids [52], it has a smaller low-field region because the discharge chamber diameter and length are much smaller, resulting in a stronger, more structured B-field than that of larger thrusters. This is illustrated in Figure 4.20. Assumptions are also made when calculating wall fluxes. In the NEXIS analytical model presented by Goebel, Wirz, and Katz [3], electron flux to the walls is entirely carried through cusps, either through thermal diffusion to a hybrid loss area for the plasma electrons or through scaling arguments for the primaries. In MiXI, there are no anode-terminating cusps, thus requiring the assumption of cross-field diffusion for plasma electron current to the anode. An averaged field strength was used, but this ignores the nonlinear relationship between field strength and electron diffusion, and the presence of other diffusion mechanisms such as Simon short-circuiting [58] from regions with lower field strength. Due to the uncertainties regarding these assumptions,

analytical models of miniature ion thrusters such as MiXI may be best suited for post-test interrogation of measured data rather than for use as predictive tools during design.

4.5 Conclusion

A low-power, high efficiency miniature ion thruster, the MiXI thruster, was integrated with an ARCH discharge and operated with beam extraction and filament cathodes, yielding a total discharge efficiency of 59% neglecting cathode losses. This corresponded to a propellant utilization of 72% and discharge loss of 226 W/A. Maximum achievable efficiency increased with increasing flow rate, although this required an increased power level. Increased discharge voltage and decreased temperature also increased maximum achievable efficiency by increasing the propellant utilization at the knee of the discharge curve. Decreasing aspect ratio was shown to increase efficiency to the detriment of stability. These results suggest that further improvement in efficiency are possible through slightly higher power operation and further optimization of anode geometry and magnetic fields. An analytical control volume model was developed to investigate internal processes occurring with these trends. The model captured the effect of increasing flow on performance but did not fully capture changes with aspect ratio or discharge voltage. Model results indicate that the dominant loss mechanism is plasma electron current to the anode and show exponentially increasing electron temperature and primary density with propellant utilization, in line with previous works. The model reproduces the phenomena of the impedance shift instability, indicating that it is a 0D effect, and may cause unstable behavior when the magnetic fields increase above a certain strength. Cathode voltage drop, modeled within the control volume analysis as a reduction in the primary electron energy, has an inverse relationship with discharge efficiency. MiIXI(ARCH) operates most efficiently and stably at higher flow rates and power levels than MiXI(3-Ring), indicating that it may be better suited as a higher-power alternative to MiXI(3-Ring).

The Miniature Xenon Ion thruster has been successfully operated with beam extraction, demonstrating performance useful for primary CubeSat and SmallSat propulsion applications and for attitude control on larger missions.

CHAPTER 5

MiXI Plume Diagnostics

5.1 Introduction

This chapter covers the development of a small plume diagnostics suite consisting of ExB, Faraday, and emissive probes, along with measurements taken of the MiXI(ARCH) plume using the suite. Previous analyses [23, 1, 43] have assumed that the thrust correction factor $\gamma = 1$ for simplicity when calculating thruster performance parameters. While this is a useful assumption for comparison, the thrust correction factor needs to be measured for an accurate estimate of on-orbit performance. For example, a generic thruster with a divergence angle of 5° and a doubles ratio of 0.1, using Equation 2.7, has its total thrust reduced by 6% due to these factors. While MiXI(ARCH)'s flat grids likely cause low plume divergence, the relatively high electron temperature as measured by Dankongkakul and Wirz [17] may cause an appreciable double ion population to form. Additionally, DC-ION computational results by Li and Wirz [5] indicate that hollow cathode operation may cause a strongly peaked beam profile, shown in Figure 5.2. Increased centerline confinement of primaries reduces the expected plasma density and beam current on the wings for some cathode positions, while simultaneously increasing the peak beam current. Computational results for spatially resolved primary and plasma density are shown in Figure 5.3. The peak density region for the filament case shows the characteristic arch which gave the discharge its name, with a diffuse primary electron population spread out between the cusps. In the hollow cathode case, however, the primary electrons are mostly confined to the centerline which leads to a center-heavy plasma profile and peaked beam. A peaked beam profile has detrimental

implications for lifetime of the thruster. Ion and current density plume measurements of the MiXI(3-Ring) configuration with a filament discharge cathode and a previous iteration of the MiXI grids were performed by Wirz et. al.[4], shown in Figure 5.1, which indicated a beam flatness of 0.60 and a negligible beam divergence for the two axial locations measured. To fully characterize the thrust correction factor and beam flatness of the MiXI thruster in its current configurations, and to understand how these parameters change with operational and physical design changes, a plume diagnostics package is needed.

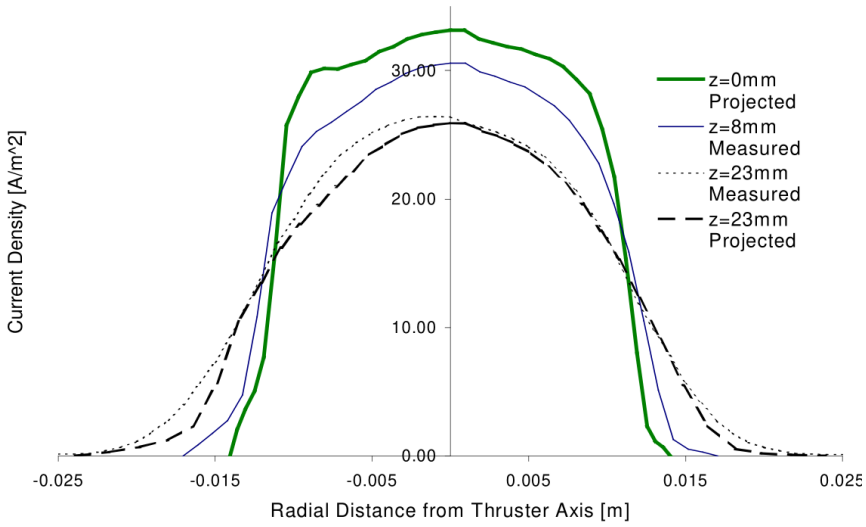

Figure 5.1: Beam current profiles for MiXI(3Ring) with modified grids. Taken from [4].

To address the unknowns with the MiXI plume profile and content, a small diagnostics suite was developed to perform a characterization similar to the one performed for the NEXT thruster [59]. This suite includes an ExB probe to measure the doubles ratio, a Faraday probe to obtain the beam profile, and an emissive probe to measure the plasma potential in the beam. The Plasma Experiment Spatio-Temporal Observation (PESTO) probe is shown in Figure 5.4.

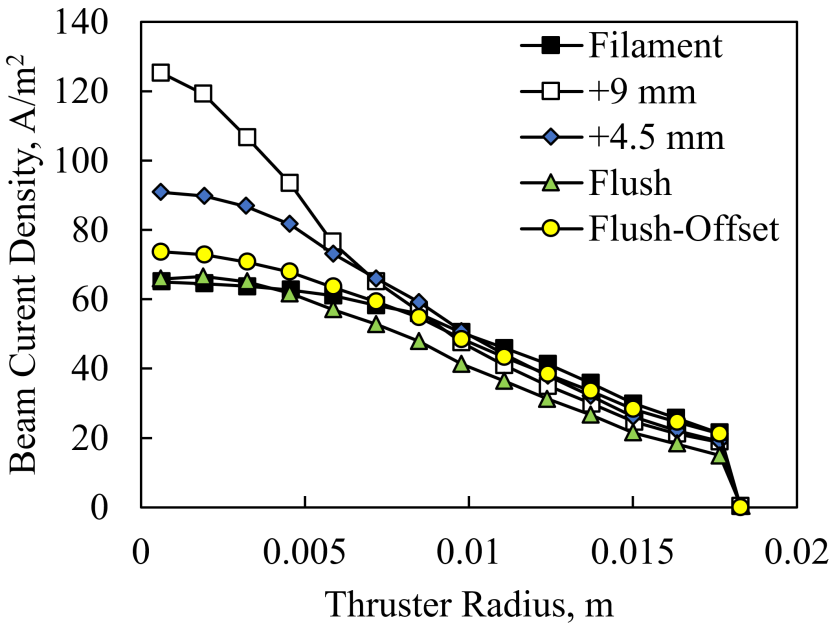

Figure 5.2: Beam current profiles for MiXI(ARCH) with a hollow cathode in different positions as predicted by DC-ION. Numerical values indicate the hollow cathode tip position relative to the backplate. Taken from [5].

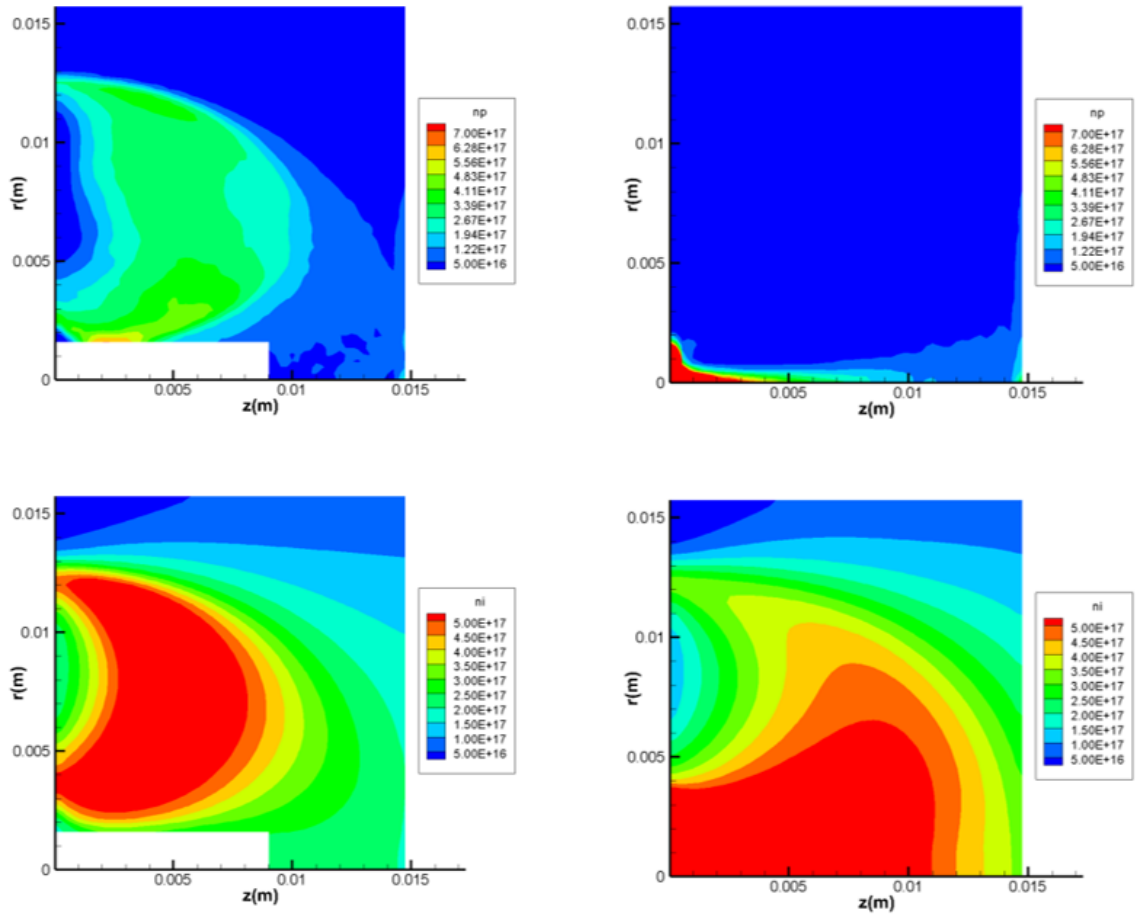

(a) Filament (b) Hollow Cathode

Figure 5.3: DC-ION computed primary electron (top) and plasma electron (bottom) density profiles for a filament cathode (a) and hollow cathode (b). Taken from [5].

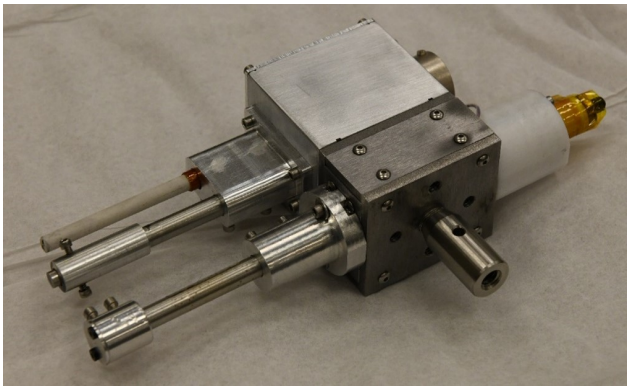

Figure 5.4: The PESTO suite, consisting of an ExB, Faraday, and emissive probe.

5.2 Design of a Small Probe Diagnostics Suite

5.2.1 The ExB Probe

The overall design goal for the ExB probe was to measure the doubles ratio of the beam as a function of radius from the thruster centerline. To do this, the relations in Section 2.4 along with COMSOL were used to design the properties of a small ExB probe, pictured in Figure 5.5. The probe was designed to have distinctive flat-top sections for the Xe^{+} and Xe^{++} peaks at 30 and 42 V, and fit within the small confines of the MiXI Bell Jar Chamber. The analytical model assumes a uniform magnetic field within the deflection section, and zero magnetic field before and after in the collimator and drift tube. To understand the effect of fringing fields at the edges of this domain, a CAD model was constructed in COMSOL and particle tracking simulations were run to generate a plot of current to the collector as a function of electrode voltage. The deflected beams of singly and doubly charged ions within the geometry can be seen in Figure 5.6. A comparison between the analytical model and COMSOL for the probe with a 2" collimator and an assumed Xe^{++}/Xe^{+} ratio of 0.1 is shown in Figure 5.7. The curve between the end of the flat top and the edge of the signal for each species is calculated by calculating the area between two intersecting circles: the screening orifice and the ion beam. Both models agree well, with a shift likely due to a slight difference in average magnetic field between the two.

In operation the body of the probe is grounded, and the collector is biased negatively to -18 V. Current to the collector is measured using a Keithley Picoammeter, and recorded using an oscilloscope. The electrodes are biased symmetrically around ground using a floated power supply. A diagram of this is shown in Figure 5.8. Blue ions come in from the left and are first collimated to some acceptance angle, and then deflected based on their velocity. Deflected ions are then screened out by the screening orifice at the back of the drift tube, and undeflected ions are captured by the collector.

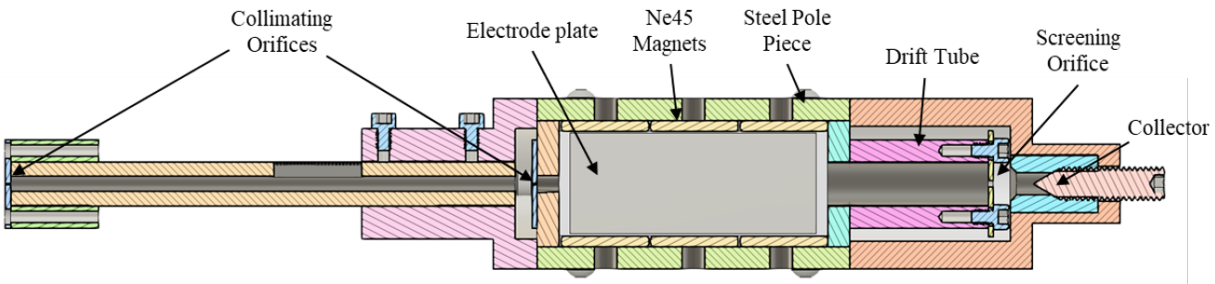

Figure 5.5: Small ExB Probe

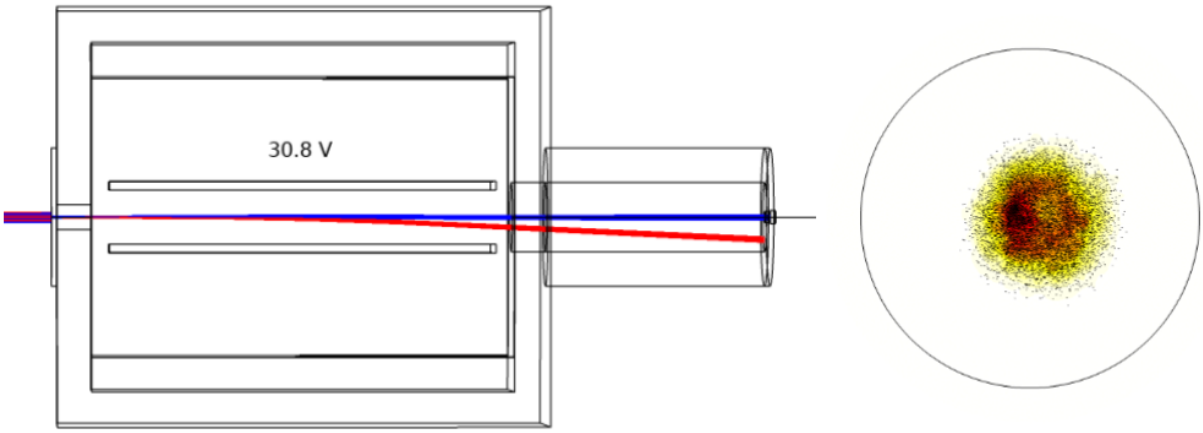

Figure 5.6: COMSOL Simulation of singly (blue) and doubly (red) charged xenon particles accelerated to 1 kV and deflected within an ExB probe. Right circle shows individual particles striking the collector.

5.2.2 Faraday Probe

The current density of the thruster plume as a function of radius has implications on thruster efficiency (beam divergence) and lifetime (beam flatness). To measure these properties, a small guarded Faraday probe was built, with a stainless steel central electrode of 0.55 mm diameter, a gap of 0.05 mm, and a overall guard outer diameter (OD) of 5 mm. The central electrode and guard ring are biased to -18 V, with the current to the electrode measured by a low current ammeter (CurrentRanger), and the resulting signal recorded on an oscilloscope. A diagram of the electrical setup is shown in Figure 5.9. The measured current (I_f) is divided

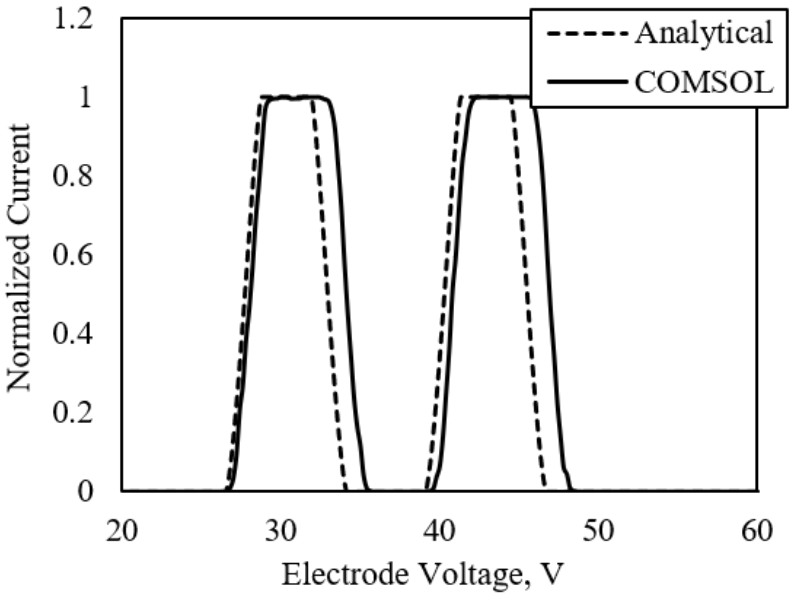

Figure 5.7: Comparison between analytical ExB trace generated using the relations given in Sec. 2.4 and a COMSOL particle tracking simulation.

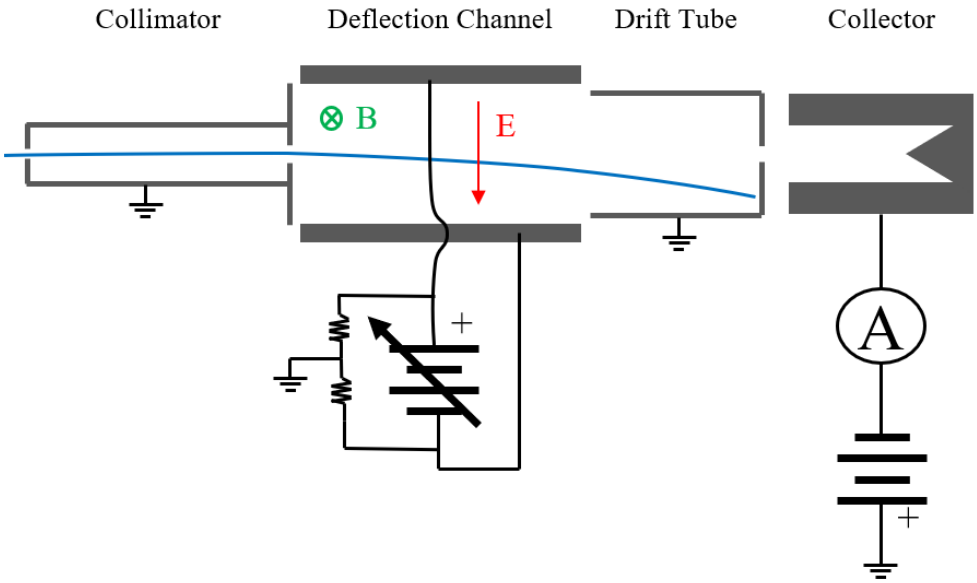

Figure 5.8: ExB probe electrical diagram with E and B vectors and blue ion trajectory.

by the area of the central electrode (A_f) to get local beam density $j_b(r, z)$:

$$j_b(r, z) = I_f(r, z)/A_f \tag{5.1}$$

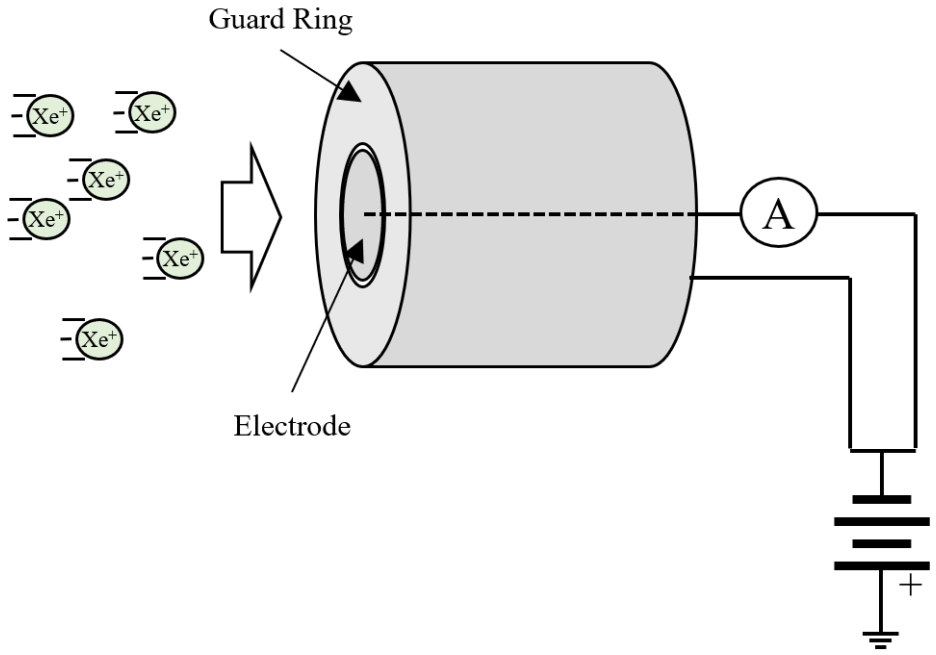

Figure 5.9: A Small Faraday Probe

The current density at the exit of the grids can be used to calculate the beam flatness, a measure of the peak beam current to the average current, and to verify direct measurements of beam current:

$$f_b = \frac{2\int_0^R j_b(r)rdr}{max(j_b)R^2} \tag{5.2}$$

5.2.3 Emissive Probe

Emissive probes are a very simple diagnostic consisting of a looped wire, heated to emissive temperatures via a floated current supply. A length of wire is heated such that it freely emits

electrons in the presence of a potential difference, and will either emit or absorb electrons until the probe potential (V_e, assumed to be at the midpoint of the probe) floats to around one electron temperature below the plasma potential V_p. As such, it is said that emissive probes give a measurement of the local plasma potential:

$$V_p \simeq V_e + T_e \tag{5.3}$$

The true acceleration potential of ions coming out of the thruster is the plasma potential of the ions (roughly the anode potential) relative to the local plasma potential. As such, if the neutralizer common line floats down to significantly below the local plasma potential (due to poor coupling of the neutraliser cathode), the thruster's efficiency will be decreased. This is the motivating need for plume potential measurements on MiXI.

5.3 Probe Study of the Miniature Xenon Ion Thruster

The PESTO suite was mounted above the MIXI(ARCH) thruster on an R-Z stage along with a small pan-tilt stage for adjusting the pointing direction of the probe. A photo of the setup is shown in Figure 5.10. The ExB probe was modified to use a 3" collimator, to increase orifice area without significantly increasing acceptance angle. The MiXI(ARCH) thruster with filament cathodes was operated at 1 kV beam potential and 20 mA beam current. This operating point corresponded to a discharge voltage of 30 V, discharge current of 200 mA, and xenon flow rate of 0.42 sccm. The PESTO suite was positioned in the center of the plume and tilted back and forth to maximize the measured ExB signal at the expected Xe^+ voltage. The maximum current measured at the center of the plume was approximately 1% of the expected average current density. The probe was swept radially across the plume at 125 mm from the grid, with data points taken at 3 mm intervals. Each datapoint consisted of approximately 3 cycles of a trianglewave with period of 20 s. The resulting ExB data for each data point was trimmed for recycle events, filtered with a 60 Hz notch filter, and smoothed

using a moving average filter. To take the Faraday and emissive probe measurements, the probe was swept in a rastered pattern across the plume at 150, 125, 100, and 75 mm from the grids. Measurements were taken continuously on an oscilloscope, trimmed for any recycle events, and smoothed using a moving average filter. The Faraday probe data was corrected for an expected iSEE yield of 0.1 for 1 keV xenon ions impinging on stainless steel [60]. The emissive probe was not corrected for electron temperature, as T_e is not measured.

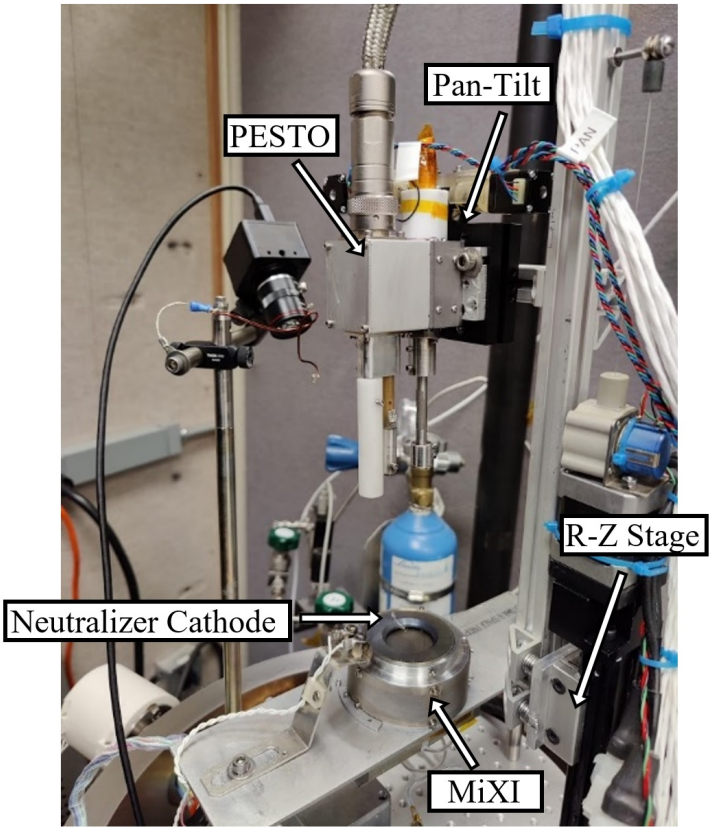

Figure 5.10: The PESTO suite installed in the MiXI chamber. The emissive probe is covered during installation with a protective PTFE tube.

The entirety of the ExB data taken for this sweep is given in Figure 5.11. While there was a distinct Xe^{+} peak along the sweep, there was no evidence of Xe^{++} in the plume. A comparison between the centerline measurement and the analytical prediction is given in Figure 5.12. The magnetic field strength and geometric properties in the analytical model

are as measured. It is clear that the model accurately captures the peak location and total signal width, but the signal peak is not a flat-top, but rather significantly rounded at the edges. These values are normalized, but as previously stated, measured current was less than 1% of local beam current density times the collimator orifice area. The peak Xe^{+} signal as a function of radius is given in Figure 5.13. The full-width half-max is less than the grid diameter, indicating that the collimator is indeed blocking off-axis ions.

The lack of a Xe^{++} signal suggests that the thruster, at this operating point, is not generating significant double ion populations. The propellant utilization at 0.42 sccm and 20 mA beam current is 0.66. While the single-cell results in Figure 4.14 indicate that at this point there is likely a high primary electron population (which will give rise to doubly-charged ions), this is not very close to the typical operating points of thrusters with hollow cathodes (MiXI(ARCH) is limited to 0.7 utilization with filament cathodes). The model, which assumes a propellant leak rate to more accurately match measured data, may be overpredicting the primary population at this operating point.

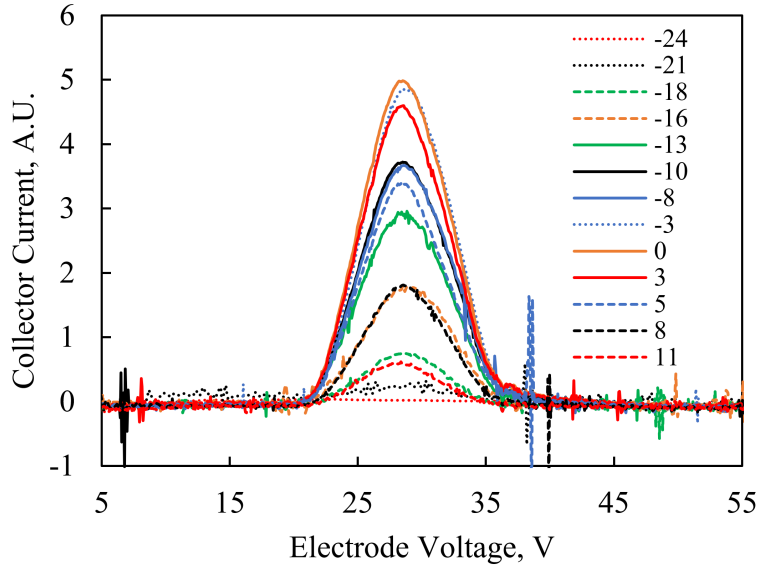

Figure 5.11: Data from ExB sweep of MiXI(ARCH) with filament cathodes. Legend is r-value in mm.

The beam current density as measured by the Faraday probe is given in Figure 5.14. The

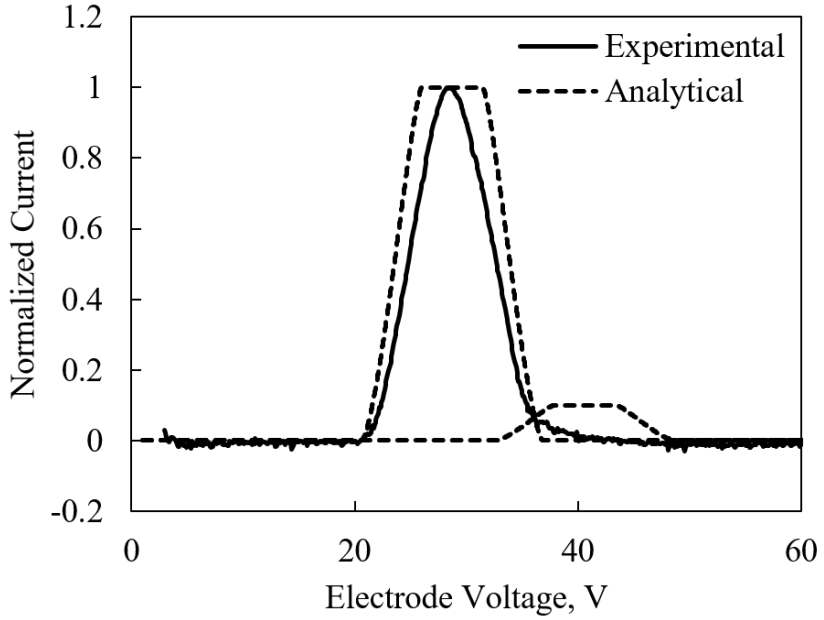

Figure 5.12: Comparison between analytical ExB model and experimental measurement at r=0 for MiXI(ARCH).

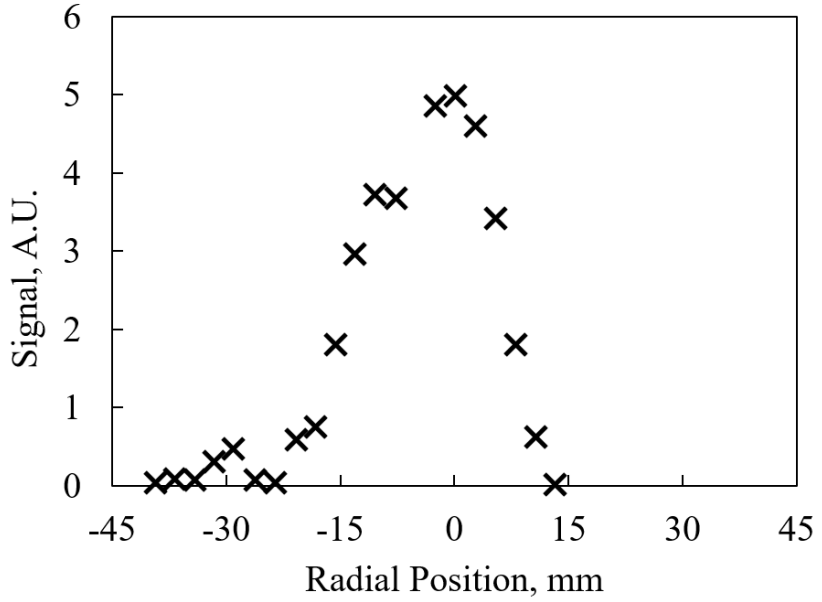

Figure 5.13: Peak Xe^{+} signal as a function of radius from centerline for a small ExB probe and MiXI(ARCH).

current density profiles are fairly symmetric, with increasing peak density and a tightening profile as the probe gets closer to the thruster grids. The FWHM of each axial location can be fit to a line, giving a plume divergence angle of around 5°. The flatness of the beam at the closest point to the thruster as given by Eq.5.2 is calculated to be 0.57, similar to that measured for the MiXI(3-Ring) configuration by Wirz[4]. This value is for an axial location of 75 mm, and would likely change if measured closer to the grids. The peak current density nearer to the grids is $70 A/m^2$, where the expected current density of the thruster at this operating point is $28 A/m^2$. Selecting the peak point, averaging the two sides together, and integrating the result yields 25, 25, 23, and 22 mA beam current for 75, 100, 125, and 150 mm respectively. These measurements are sensitive to the outer bound of integration, implying that there is a significant current density at the fringes of the plume. This can be a real ion population from the beam, or more likely, background plasma in the chamber that is being measured as beam ions. To counteract this, future iterations of PESTO will replace the Faraday probe with a Retarding Potential Analyzer, which can reject lower energy ions and measure only the high-speed beam population.

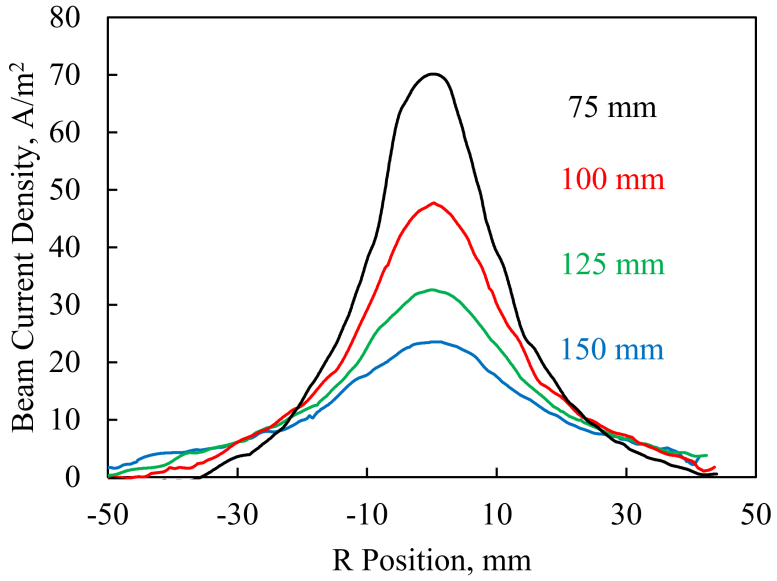

Figure 5.14: Plume current density as measured by the PESTO Faraday probe on MiXI(ARCH) running on filament cathodes.

The plasma potential as measured by the emissive probe for the same positions as the Faraday probe are given in Figure 5.15. The flat region in the center corresponds to the region where the bulk of the current density is located. The measured plasma potential is 4 - 4.5 V at the closest measurement point to the grids, and increases slightly to 5 V further away. To the left of the center point there is an asymmetric structure likely caused by the placement of the filament neutralizer cathode. Because standard emissive probe theory assumes a non-flowing plasma, it is likely that there are some ram effects occurring due to the high velocity ions streaming from the thruster, which may modify the results in the plume region.

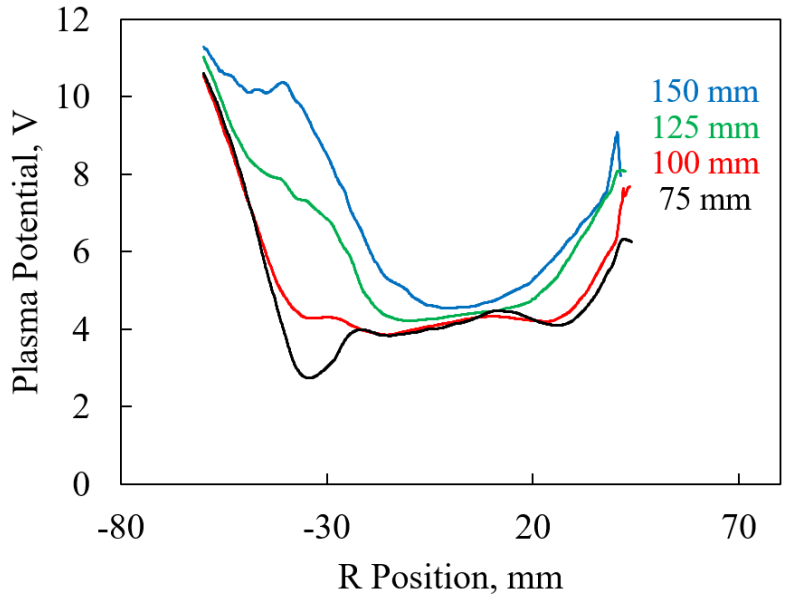

Figure 5.15: Plume plasma potential relative to facility ground as measured by the PESTO emissive probe on MiXI(ARCH) running on filament cathodes. No electron temperature correction has been applied.

5.4 Conclusion

To further build the infrastructure for future MiXI development and characterization, a small probe suite was designed to provide measurements of the plume doubles ratio, current density, and divergence. These measurements have important implications for the efficiency and lifetime of the thruster. The suite was developed using a combination of analytical and computational tools, manufactured, and used to measure the MiXI(ARCH) plume in a single operating point, resulting in a beam flatness of 0.6, a divergence angle of 5°, and a negligible doubles ratio for that particular operating point. These measurements were taken with filament cathodes, and as such, must be taken as validation of the probe design and analysis methods, rather than actionable data about the MiXI thruster. Future hollow cathode integration and throttle table characterization will identify trends in the measurements, and include plume measurements for more accurate predictions of on-orbit performance.

CHAPTER 6

Cathode Development and Testing

6.1 Introduction

Two hollow cathodes are required for operating the MiXI thruster: one for the discharge which provides 100 - 500 mA discharge current and 0.15 - 1 sccm flow (depending on the MiXI configuration), and one as the neutralizer which provides 10 - 50 mA current to neutralize the beam. This chapter initially covers current progress on integrating hollow cathodes into the discharges of MiXI(ARCH) and MiXI(3-Ring), and then basic characterization of a potential MiXI neutralizer hollow cathode. Development principles and efforts to design improved hollow cathode electron sources for the MiXI thruster are then presented, along with a proposed design for a new 1/8" MiXI LaB_6 cathode.

6.2 Initial Efforts Towards Discharge Hollow Cathode Integration

Most of the previous development, testing, and characterization efforts on the MiXI thruster have utilized tungsten filament cathodes for both discharge and neutralizer for simplicity [17, 8, 61, 43]. While filament cathodes are commonly used for ease of testing in lieu of hollow cathodes, hollow cathodes are more appropriate for flight due to their typically longer life and superior mechanical robustness. As such, further maturation of the MiXI thruster requires the incorporation of hollow cathodes for discharge and neutralizer. A conventionally-sized hollow cathode was previously integrated into MiXI(3-Ring) as discharge cathode by Mao, Wirz, and Goebel[62] for internal plasma probing with simulated beam extraction, but this

analysis focused on internal plasma structure and not performance characterization. No performance data has been published with miniature hollow cathodes[12, 63, 64] and hollow cathodes have not been used as neutralizer in a thrust-generating configuration. However, while the MiXI(3-Ring) configuration has operated with a hollow cathode, the higher power MiXI(ARCH) configuration has not been run with hollow cathodes.

Following the successful beam extraction of MiXI(ARCH) with filament cathodes, work was done to integrate hollow cathodes within the MiXI thruster. While filament cathodes are chemically resilient to poisoning, simple to operate, and result in favorable plasma emission, hollow cathodes have been shown to be more efficient, have longer lifetimes, and are more mechanically robust for space applications. DC ion thrusters almost exclusively use hollow cathodes, with the alternative being microwave or RF-generated plasma rather than filaments. Additionally, previous analyses assumed self-heated cathodes in calculations for total efficiency. The use of filament cathodes for flight would cause a significant reduction in system performance as filament heater power is typically on the order of 20 W for MiXI testing. As such, it is critical to integrate and characterize the MiXI thruster with hollow cathodes to both further develop the system for flight and to more accurately determine performance values.

6.2.1 Experimental Setup

As with the filament cathode testing in Section 4.3, testing occurred at the Plasma and Space Propulsion Laboratory, in the same MiXI bell-jar. The power and control rack was reconfigured to include a keeper power supply, diodes for discharge protection, and constant-current operation for the discharge power supply. A diagram of the system is shown in Figure 6.1.

The MiXI hollow cathodes consist of four small cathodes developed by Wirz at JPL [12]. They are small BaO type A cathodes, with various orifice geometries sized for different applications. Prior to this effort, the largest cathode was damaged and the orifice plugged

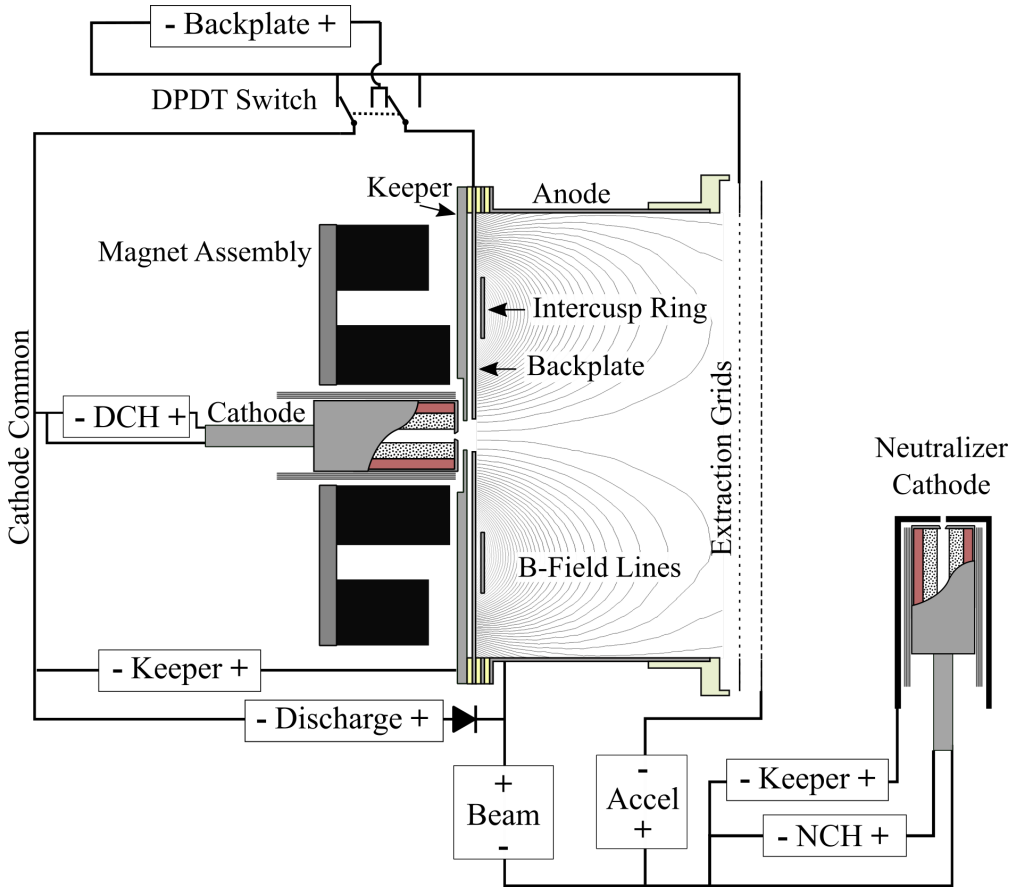

Figure 6.1: MiXI electrical connections for hollow cathode operation. Keeper supplies, discharge diode, and discharge constant current control have been added from the performance studies with filament cathodes.

with stainless steel, and has not been operated within the thruster. The two cathodes of relevance to this effort are referred to as the neutralizer cathode (which was actually used as the discharge cathode for MiXI(3-Ring)) and the discharge cathode. The cathodes use the tube body as the return line for the heater, with the body and orifice at cathode common. The orifice diameter of the hollow cathode affects the current density in the orifice for a set current, and the pressure in the insert for a given propellant flow rate.

Figure 6.2: MiXI mini cathodes next to a US dime. Cathodes use a BaO insert and have various orifice geometries for discharge and neutralizer operation.

6.2.2 Cathode Ignition and Initial Operation

Prior to installation into the MiXI thruster, the discharge cathode was installed in a triode configuration with a wire keeper and plate anode to condition and develop ignition procedures. The cathode was under vacuum of 1e-6 Torr for 24 hours, underwent a 0.1 sccm xenon purge of 99.9999% purity for two hours, and then was slowly ramped up to full 15 W heater power over a period of four hours. The keeper supply was set to a current of 120 mA and voltage of 1.5 kV. The propellant flow valve was shut for 30 seconds with flow of 5 sccm, and then rapidly opened to burst the cathode flow. The cathode lit reliably using this procedure, and was able to operate down to 1 sccm, 0.5 A discharge, self-heated in diode mode. Operation of the neutralizer cathode used this same procedure.

6.2.3 Initial Triode Characterization of the Neutralizer Hollow Cathode

To determine cathode regions of stable operation and the applicability of the neutralizer hollow cathode, the smallest cathode was characterized in triode mode over a range of gas

flow and heater currents. The cathode was set up in triode mode with a graphite keeper with orifice 1 mm diameter, 1 mm from the orifice. The cathode was wrapped with 10 layers of tantalum foil along the entire length of the cathode head and stem. Later thermal modeling suggested that this is not the ideal heat shield length, and that shielding only the head results in less heat loss. The cathode was conditioned per the procedure detailed in Section 6.2.2, and operated in a range of flow rates and discharge powers to determine the minimum flow and power possible with the cathode. Representative Current-Voltage sweeps of the cathode at 0.3 sccm xenon flow are given in Figure 6.4(a). As seen in Figure 6.4(b), required keeper power decreases as discharge current and heater power increase. Plume mode onset was investigated by changing flow rate with a set discharge current of 30 mA, keeper current of 150 mA, and heater power of 14 W. Results are presented in Figure 6.5, which show the minimum flow rate before large keeper voltage swings is 0.1 sccm, although the cathode still operated at 0.03 sccm. Interestingly, the keeper also became unstable at flow levels above 1 sccm. Note that because the keeper was pulling current, the "peak-to-peak" value includes power supply oscillations, which for high voltage supplies can be significant. The cathode operating point of 0.1 sccm and 15 W power is plotted in Figure 6.6 on the contour plot of burn time and wet mass as a function of neutralizer cathode properties generated for the 6U CubeSat study in Section 3.4. The required power effectively doubles the required burn duration for a 3 km/s maneuver, while the required flow increases the craft wet mass by $\sim 8\%$.

6.2.4 Initial Results for MiXI(ARCH) Hollow Cathode Operation

The discharge hollow cathode was installed in MiXI(ARCH), and the thruster was operated with beam extraction and a filament neutralizer cathode. The discharge cathode was operated with 0.75 sccm gas flow, ∼10 W heater power, and ∼2.4 W keeper power. The thruster operated with accelerator voltage of 75 V, 1 kV beam potential, backplate 10 V below cathode common, and screen grid at cathode common. The initial testing took place without

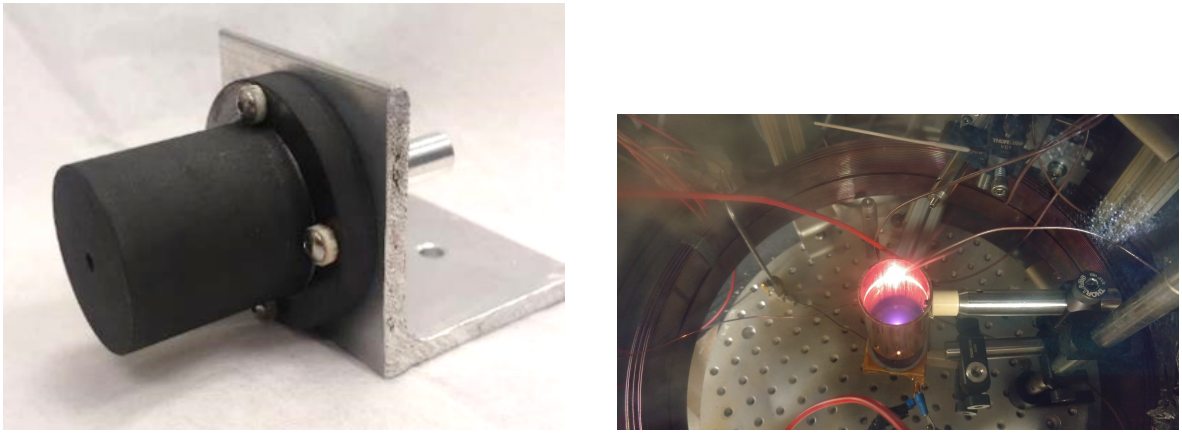

(a) Triode Mode Keeper (b) Neutralizer Cathode Operating

Figure 6.3: Photos of the keeper for the triode characterization of the miniature hollow cathode neutralizer, and the cathode in operation.

a discharge supply protection diode, and recycling of the system damaged the discharge voltage divider circuit (beam potential across the voltage divider burnt out the resistor, a protection diode and TVS diodes were installed as a remedy), without being noticed before testing. As such discharge voltage is assumed to be a constant 27 V, as it was visually noted to be during testing. Results are presented in Figure 6.7. The discharge loss plot does not include the 12 W required for the cathode heater and keeper, and shows decreasing discharge loss with increasing propellant utilization. This trend of a negative-going discharge curve has been seen before in predictions for the 50 ks I_{sp} lithium thruster by Brophy and Goebel [65]. At the peak point of efficiency for this particular operating point (excluding the outlier), the thruster was operating at 75 W, 850 W/A discharge loss, 43% total efficiency at 1 kV, (including discharge cathode losses, but not neutralizer), and 39 mA beam current. Excluding discharge heater and keeper losses (which may be reasonably assumed to be significantly reduced with cathode design iterations), the peak efficiency is 52% at 60 W discharge + beam power. This value does not include impacts due to thrust correction factors, or the neutralizer cathode heater and keeper power. Because cathode operation has not been optimized, and later operation identified that keeper current may be significantly reduced without significant effect, these values should be treated as a lower limit for efficiency, and

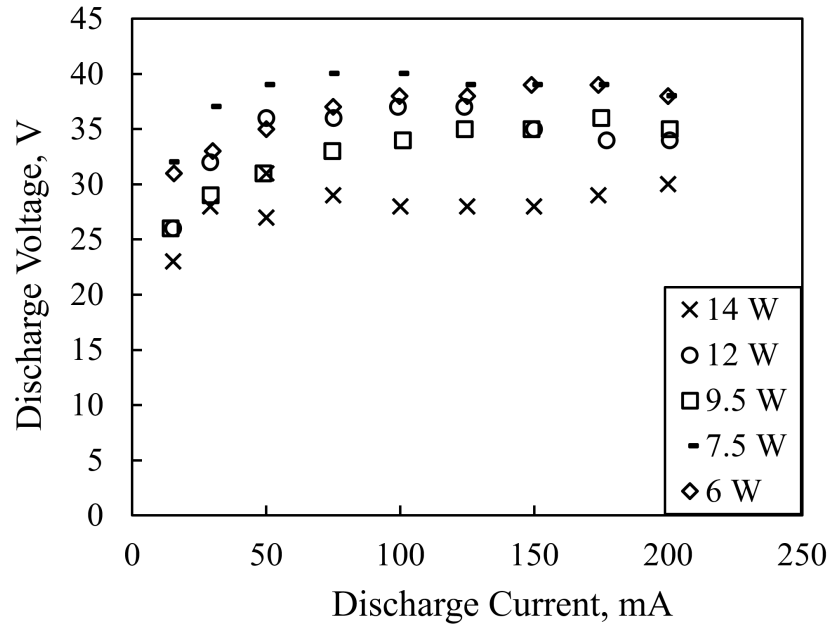

(a) I-V Plot

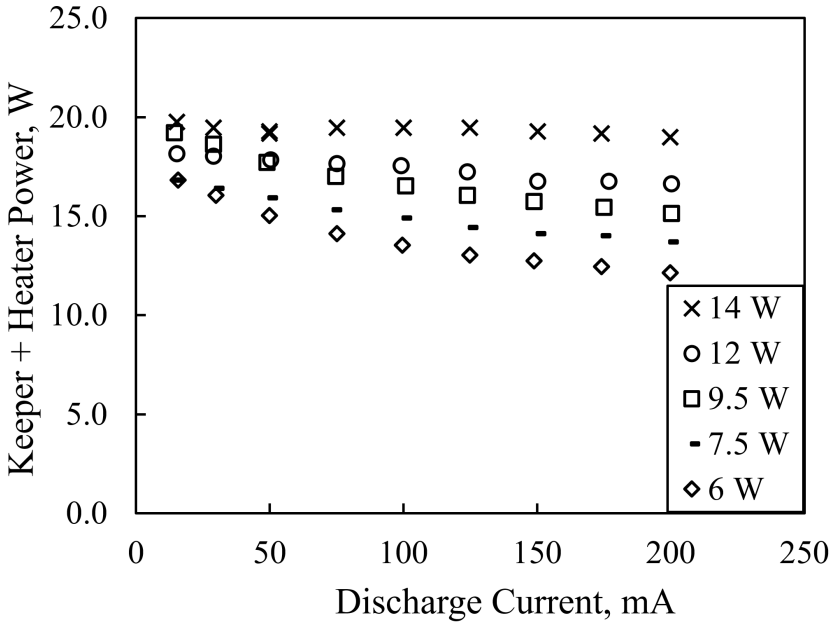

(b) Keeper Power

Figure 6.4: Characterization data for the neutralizer hollow cathode at 0.3 sccm flow in triode mode. Keeper current is 150 mA for all cases. Legend is heater power.

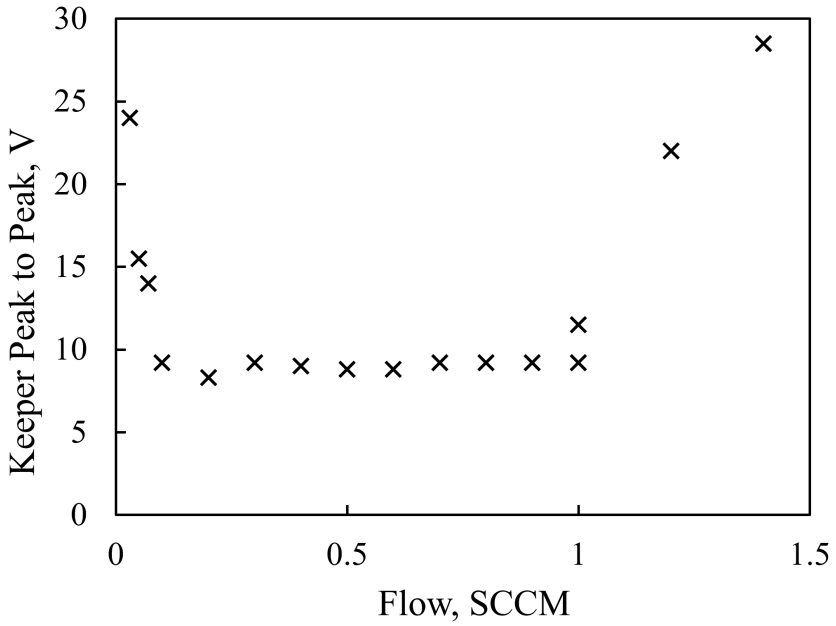

Figure 6.5: Neutralizer cathode keeper peak-to-peak voltage swing for a variety of flow rates. Data taken with 30 mA discharge current, 150 mA keeper current, 14 W heater power. Because keeper was biased and pulling current rather than floating, the 9 V keeper peak-to-peak floor may be due to the power supply rather than the cathode.

further characterization of the thruster, optimization of the cathodes, and tweaking of the discharge properties will likely increase performance further.

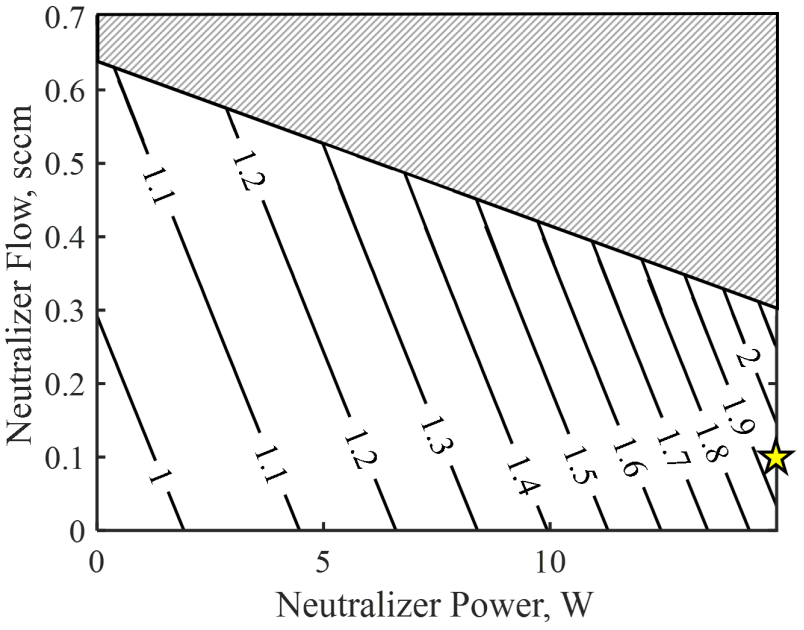

(a) Burn Duration

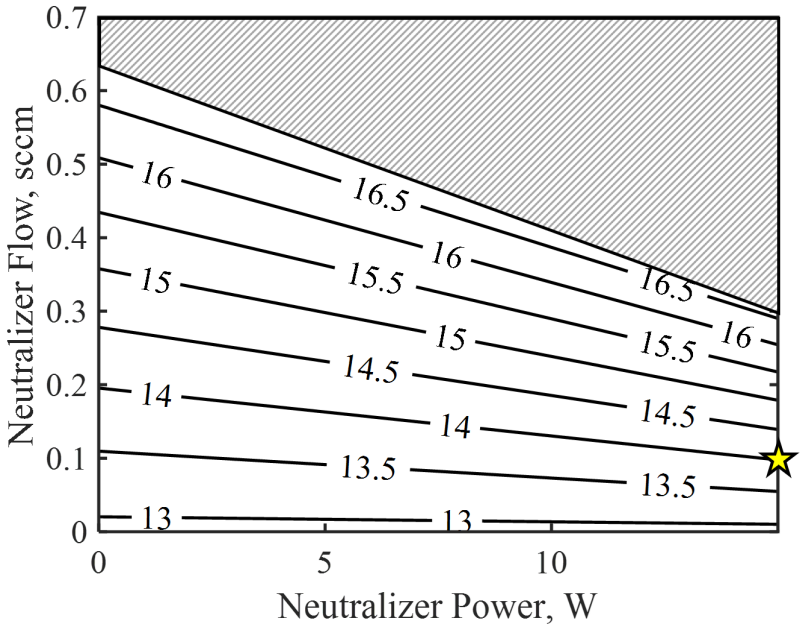

(b) Craft Wet Mass

Figure 6.6: Figure 3.9 from the 6U MiXI CubeSat study for a 3 km/s ΔV maneuver, with the characterized cathode plotted.

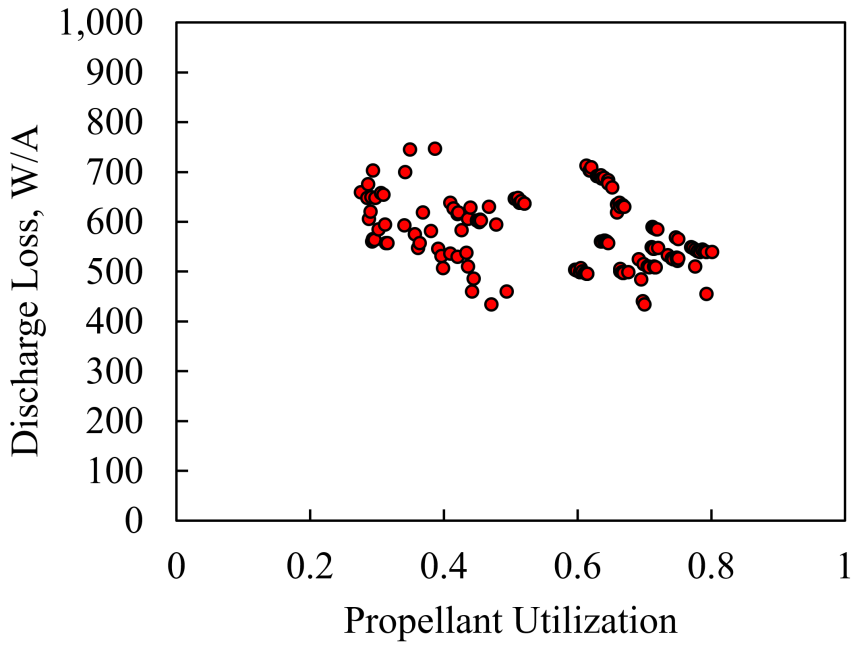

Figure 6.7: Run data for MiXI(ARCH) with a mini BaO hollow cathode. **These values should be seen as lower bounds for MiXI(ARCH) performance at this particular operating point because this is not using high-efficiency cathode design or operation. Improvements in cathode operation and future cathode and thruster optimizations will only increase discharge efficiency.**

6.3 Motivations for Cathode Improvement

The discharge and neutralizer cathodes play different roles for the thruster, and have different impacts on thruster performance. The neutralizer cathode has three main properties which affect the thruster: neutralizer coupling voltage, power, and flow rate. Neutralizer coupling voltage is the voltage that the neutralizer common differs from space potential, such that the accelerating potential that ions experience is $V_b - V_{nc}$. This decreases the effective power going into thrust for a given input power. The calculation for electrical efficiency of the thruster is then changed from Eq. 2.5 to:

$$\eta_e = \frac{I_b(V_b - V_{nc})}{\sum P} \tag{6.1}$$

The I_{sp} is also reduced because of the reduced acceleration potential:

$$I_{sp,new} = I_{sp,ideal}\sqrt{\frac{V_b - V_{nc}}{V_b}} \tag{6.2}$$

Because the beam voltage V_b is typically a large value on the order of 1 kV, only a large V_{nc} will have much effect. V_{nc} is the required virtual anode voltage to extract a neutralization current equivalent to the beam current from the neutralizer cathode, so it is a function of cathode performance and operating point. A better performing cathode will have a lower V_{nc}. Required neutralizer flow and power do not affect thruster physics, but instead are simply parasitic values which are tacked onto the system as a whole. A higher neutralizer power or flow will increase the system power and flow requirements without affecting the thruster head properties. This in turn will decrease system I_{sp} and electrical efficiency. The effect of neutralizer properties on a MiXI CubeSat mission is explored in Section 3.5.4.

The discharge cathode directly affects the discharge plasma properties through the cathode voltage drop V_c. This is the plasma potential at the orifice of the cathode, and decreases the energy of primary electrons entering the discharge chamber. Analytical modeling of the effect of cathode voltage drop was performed in Section 4.4.2.1, and showed that increasing V_c can significantly increase discharge loss. Assuming that some fraction k of the ohmic power loss in the cathode is used to heat the cathode, the power balance on the cathode can be written as:

$$P_l = kI_dV_c \tag{6.3}$$

where P_l is the thermal heat loss of the cathode, k is some unknown function, I_d is current emitted by the cathode, and V_c is the plasma potential at the exit of the cathode orifice. For a given value of I_d and k, with increasing power loss the cathode voltage drop will increase to compensate. Minimizing the power loss from the cathode is then by this simple argument expected to decrease the cathode voltage drop.

6.4 Development of Miniature Cathodes

6.4.1 Thermal Analysis of Small Cathodes

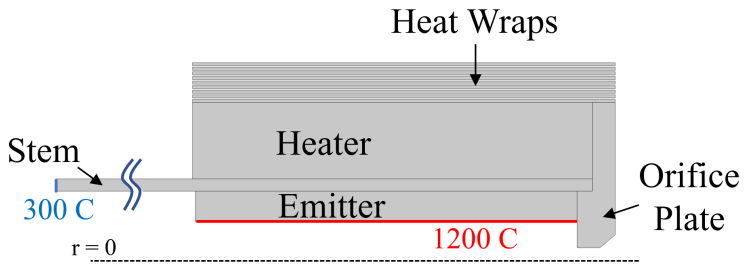

Figure 6.8: Diagram of the COMSOL cathode model.

A thermal simulation of the cathode characterized in Section 6.2.3 was performed to assess heat loss mechanisms. The COMSOL heat transfer module was used for calculation, and a parametric model was generated using the internal CAD package to allow for parametric sweeping of geometry and material properties. The inner surface of the insert was held at 1200 C, an approximate typical operating temperature of BaO. The base of the cathode stem was held to 300 C, the temperature measured at the outer flange of the thruster head during operation. A diagram of the setup is shown in Figure 6.8. The simulation was set up to include realistic thermal contacts between the insert and stem, and a bonded thermal contact between the stem and orifice plate, and heater to everything it touches. All surfaces are assumed to be radiating with emissivities set by the material properties. It is assumed that all heat flux lost to the boundaries (radiated and conducted) is required to be deposited by a combination of keeper and heater power, so by conservation of energy, "Required Operating Power" is measured as the heat flux into the system at the emitter boundary condition. An image of the resulting temperature profile is given in Figure 6.9. The entire head of the cathode is nearly isothermal, with the majority of the thermal gradient in the cathode stem. The 10 layers of heat shields effectively prevent the outer surface of the cathode head from radiating heat. The power lost to the end of the cathode stem was 5.9 W, with 3.6 W

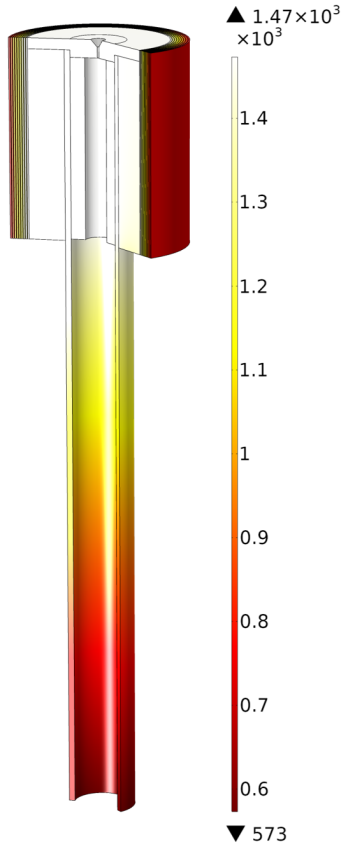

Figure 6.9: Temperature distribution of the BaO cathode. Reported temperature is in Kelvin.

additionally lost via radiation for a total of 9.5 W heat lost. This is about half of the 20 W needed for operation at low discharge currents, as shown in Figure 6.4. This discrepancy may be explained by lower boundary condition temperatures for the far-field (for radiation) and the cathode stem (for conduction), incorrect material properties, the crinkled heat wrap performing poorer in the test than simulation, and slightly different geometry in the model vs reality. Regardless, the simulation suggests that a majority of heat is lost to the stem via conduction, and that a significant portion of the total power is radiated by the top orifice plate.

Three modified designs were generated and analysed in a similar manner to understand

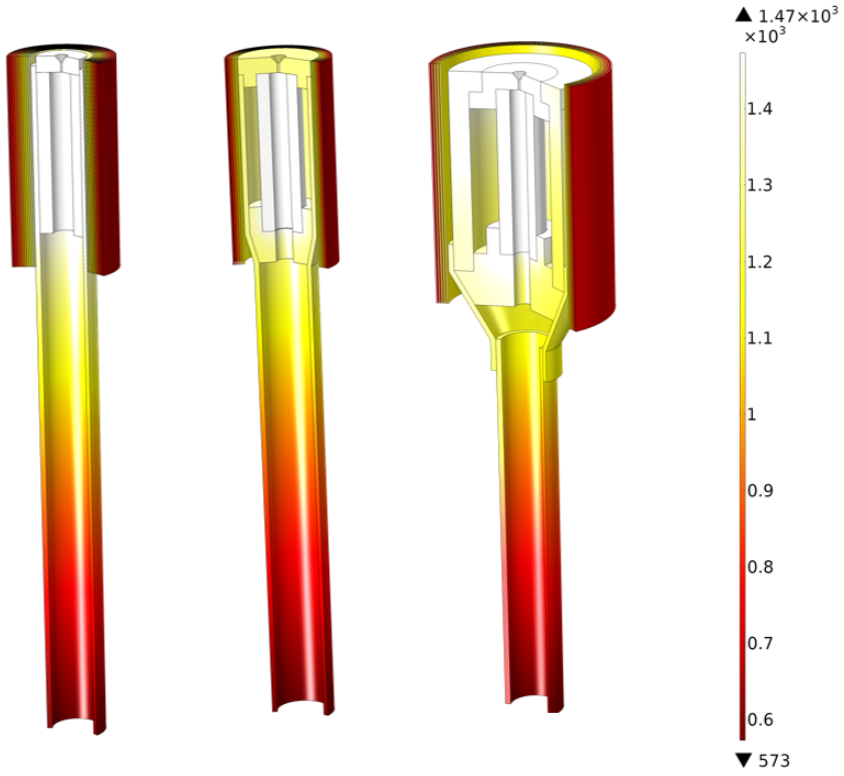

Figure 6.10: Temperature distribution of three candidate cathode designs. Reported temperature is in Kelvin.

Table 6.1: Mini Hollow Cathode Thermal Simulation

Cathode	Total Power, W	Conducted, W	Radiated, W
Original BaO	9.4	5.9	3.5
KISS	4.4	3	1.4
Sleeve	4.9	2.6	2.3
Uber	4.1	0.43	3.67

potential improvements to the thermal design. The first derivative design, dubbed the "KISS" cathode, swapped the stem material out for a lower conductivity high temperature alloy and eliminated the heater to decrease both conduction and radiation losses. The second, the "Sleeve" cathode, attempts to increase the thermal path length from the orifice and insert by creating a vacuum gap between the outer edge of the insert and the stem, as well as a zirconia ceramic seat to minimize heat transfer from the bottom of the insert to the

stem. The third, called the "Uber" cathode, attempts to further reduce thermal conductivity by replacing the upper stem portion of the cathode head with a zirconia ceramic shell which further reduces the conductivity from the orifice plate to the base. Temperature profiles of the three cathodes are presented in Figure 6.10, and the resulting thermal power loss is given in Table 6.1. By virtue of a complicated thermal path through thermally resistive materials, the "Uber" cathode significantly reduces conduction losses, although the large top face (with a significant surface area of high-emissivity material) allows for large radiated losses. While this cathode design is slightly more efficient than the other two, it is significantly more complicated to manufacture, and likely more fragile than the more traditional KISS cathode. As such, the simple insert-in-tube design was selected for further development. To simplify ignition, a LaB_6 insert was also selected. To understand the heat loss of the cathode as a function of cathode and heat wrap length, a parametric sweep was performed in COMSOL, assuming 1700 C as the insert boundary condition. The total heat loss is shown in Figure 6.11. Increasing the heat shield coverage from 0.5" to 1" decreases the power loss by 15% at the original cathode length, and almost 30% for 2" long cathodes. Increasing the cathode length also decreases power loss, as would be expected by the definition of thermal conduction P = k*dT/dx. Increasing the "dx" term, which decreases the thermal gradient, decreases the conduction down the stem. Using a simple ball-on-stick model, the natural frequency of the cathode at 2" is expected to be over 1 kHz, and showed structural significant margins when simulated with 50 G radial loads.

6.4.2 Insert Design

The heaterless cathode design was selected because it was shown that a smaller surface area decreases the amount of radiated power loss. Heaterless cathodes have been demonstrated in the past, and to reduce complications surrounding the use of BaO, a LaB_6 emitter was selected. LaB_6 is a bulk sintered crystal, while BaO is a tungsten foam that has been impregnated with a mix of barium and other oxides. The insert geometry must be designed

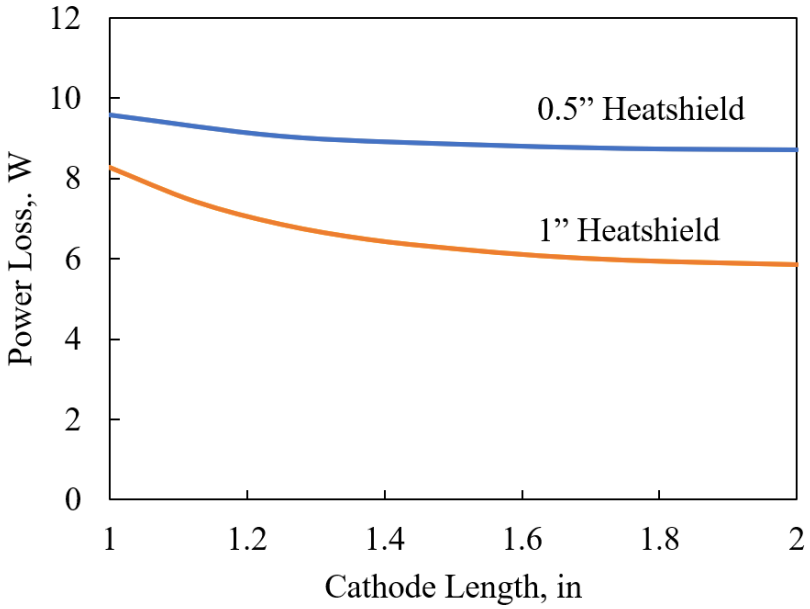

Figure 6.11: Heat loss for a small LaB_6 cathode as a function of cathode length for two heat wrap lengths.

with considerations for the resulting insert plasma as well as lifetime. While some analytical cathode plasma models exist, they are typically inaccurate or require inputs from 2D computational codes or experiments. As such, the insert will be designed primarily to meet a lifetime constraint. The cathode lifetime was predicted for a given geometry using an evaporative lifetime model [66, 67] which assumes no sputtering of the insert, no redeposition, and a uniform temperature.

The total current emitted by the cathode is a combination of the discharge current J_d, the keeper current J_k, and the return current J_r. The return current is due to electrons born in the insert plasma overcoming the sheath potential and striking the insert surface. Because the insert plasma electron temperature is typically quite low compared to the plasma potential, this is a relatively small current. The emission surface area is the inner radius of the insert times some plasma attachment length, typically estimated from internal cathode probing or computational models. The Richardson-Dushman equation describes thermionic

emission from cathode materials:

$$J = AT^2 e^{\frac{-e\phi}{kT}} \tag{6.4}$$

Where J is the emission current density, A is a universal constant of $120 A/cm^2 - K^2$, ϕ is the material work function, and T is the material temperature. A temperature dependence of ϕ leads to a modified equation with a material-specific constant instead of the universal:

$$J = BT^2 e^{\frac{-e\phi}{kT}} \tag{6.5}$$

Where B is the material-specific constant. For LaB_6, the value is given as 110 for a work function of 2.87 eV [68]. For a given emitted current and surface area, the required surface temperature may be calculated. The resulting evaporation rate may be calculated by an experimental relation given by Lafferty [69]:

$$W = \frac{10^{C-B/T}}{\sqrt{T}} \tag{6.6}$$

Where W is the evaporation rate in $gm/(cm^2 \cdot s)$, B and C are experimentally determined constants which are 36,850 K and 13 respectively, and T is the material temperature in Kelvin. The rate of change of the insert inner diameter is then given as:

$$\dot{d} = \frac{W(J)}{\rho} \tag{6.7}$$

The density of the material is ρ (which must be the as-sintered bulk material density rather than the theoretical crystal density), and l is the plasma attachment length. From some initial conditions, Eqs. 6.5 - 6.7 can be integrated in time to determine the insert inner diameter and temperature at any time. The lifetime is considered to be the time until the insert wall thickness gets below some minimum structural value. The main inputs

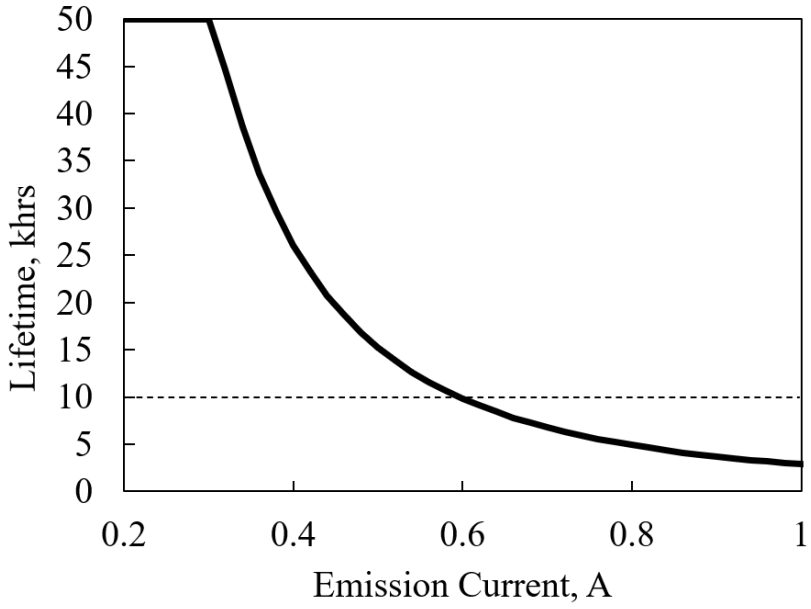

Figure 6.12: Predicted evaporative lifetime for a LaB_6 insert with the same geometry as the original MiXI cathode. "Lifetime" is defined as the time until the emitter wall thickness reaches 0.3 mm. The dashed line corresponds to a 10khr lifetime.

to the model are: attachment length (which is an empirically or computationally-derived value), insert inner diameter (ID) and outer diameter (OD), and emission current. The insert attachment length is determined by scaling previous, unpublished internal probing results of similar small cathodes by insert ID and emission current using relations given in [22]. The expected lifetime as a function of emitted current for a LaB_6 insert with the same geometry as the original BaO Mixi cathode insert is given in Figure 6.12.

For any current below 0.6 A, the expected insert lifetime is over 10 khrs, and rapidly increases with decreasing current. This is due to the strong relationship between evaporation rate, insert temperature, and emitted current density. To explore the sensitivity of lifetime to emitter geometry, parametric sweeps for ID, OD, and emitted current were performed. These results are shown in Figures 6.13 and 6.14. As may be intuitive, increasing the emitter wall thickness by either decreasing the ID or increasing the OD increases lifetime. Decreasing the emitted current also increases lifetime, as with previous results. There is a much stronger

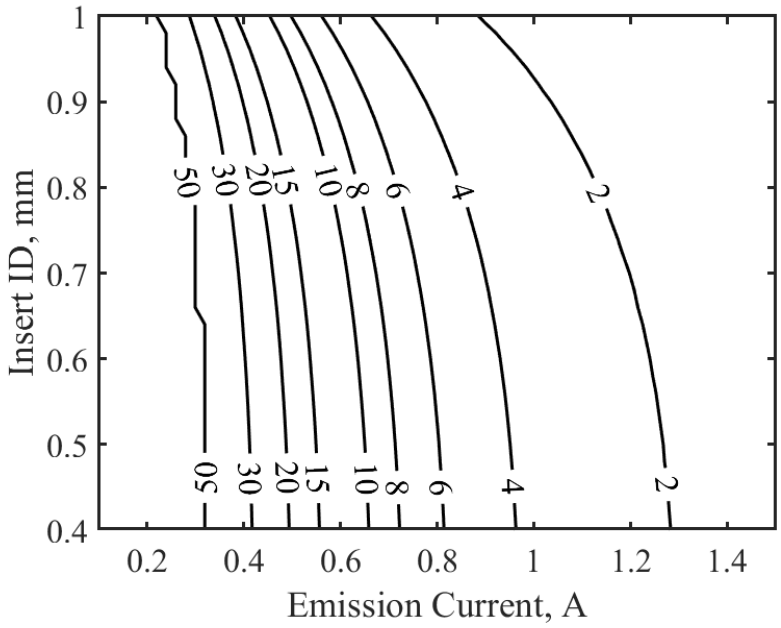

Figure 6.13: Predicted evaporative lifetime in khrs for a LaB_6 insert with the same OD as the original MiXI cathode as a function of emitted current and ID.

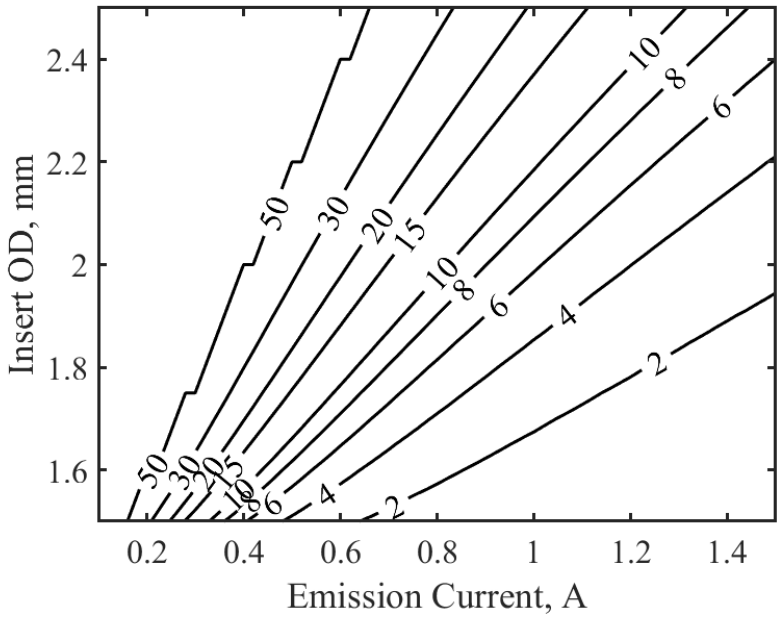

Figure 6.14: Predicted evaporative lifetime in khrs for a LaB_6 insert with the same ID as the original MiXI cathode as a function of emitted current and OD.

dependence of lifetime on emission current than either of the geometric diameters.

6.4.3 Orifice Design

The orifice of a Type-A cathode provides a restriction for neutral flow which increases the gas pressure of the insert region, and pinches down the cathode orifice plasma which provides the main source of heating for the cathode. Cathode orifices may be designed using empirical relations derived from experiment or computational codes. One commonly cited guideline is that of Kaufman, who compiled a list of several mercury hollow cathodes and observed that of those cathodes, a current density of greater than 12 A / mm diameter was a predictor of significant orifice erosion. [15] This is plotted in Figure 6.15. It is readily apparent that for the expected MiXI currents of 0 - 0.5 A, any reasonably sized orifice will not exceed the Kaufman criterion. For a 1 A current, the cathode is at 1 kA/cm^2 with a diameter of 0.014". At a more realistic 0.3 A, a 0.008" orifice provides a current density of slightly less than 1 kA/cm^2.

One other potential method for orifice sizing is to match the internal pressure of the insert to previously characterized cathodes. Several authors have developed cathode models, however few are accurate on multiple cathodes and operating conditions. [70] One common method [22, 18] is to calculate the internal pressure due to the neutral gas alone, with some assumed temperature. This assumes continuum flow, which is likely valid in the insert and upstream cathode orifice areas. From basic flow calculations, the Knudsen number in the cathode is expected to vary between 0.001 and 0.1 at different operating conditions, while the Reynolds number in the insert is near unity. The exit of the orifice is assumed to be choked flow:

$$\dot{m} = C_d \frac{A p_{or}}{\sqrt{T_t}} \sqrt{\frac{\gamma}{R}} \left(\frac{\gamma+1}{2}\right)^{-\frac{\gamma+1}{2(\gamma-1)}} \tag{6.8}$$

$\dot{m}$ is the mass flow through the orifice, C_d is an empirically determined discharge coef-

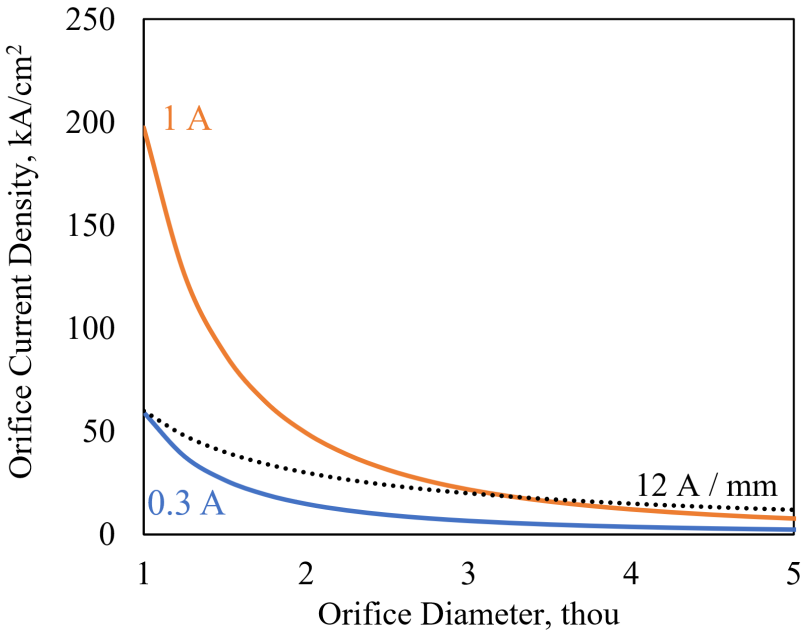

Figure 6.15: Orifice current density for various cathode currents as well as the Kaufman 12 A / mm criterion.

ficient, A is the orifice area, p_{or} and T_t are the total pressure and temperature at the end of the orifice, and γ and R are the gas-specific specific-heat ratio and gas constants. The pressure at the beginning of the orifice is then calculated assuming compressible Poiseuille flow:

$$P_{insert} = \sqrt{\dot{m}\frac{16\mu}{\pi r_0^4}RT_0L_0 + P_{or}} \tag{6.9}$$

Domonkos includes a correction factor for the restriction at the sharp transition from the insert region into the orifice:

$$P_{insert} = \sqrt{\dot{m}\frac{16\mu}{\pi r_0^4}RT_0L_0 + P_{or}} + \frac{1}{2}\rho u^2(1 + C_d) \tag{6.10}$$

Because the correction factor is a function of ρ and u the density and velocity just

upstream of the orifice, the equation must be solved iteratively. However, it is typically a small factor at cathode flow rates. Because the insert is typically much larger ID than the orifice, the pressure just upstream of the orifice is taken as the insert pressure. The insert pressure as a function of flow rate for a small cathode with similar geometry to the original MiXI BaO cathodes was calculated for various orifice diameters, shown in Figure 6.16. This calculation is geared towards a neutralizer cathode, with minimal flow and power. The dashed line corresponds to 145 Torr, the internal pressure measured for the NSTAR neutralizer cathode at TH15. [71]. For a desired flow rate of 0.1 sccm, an orifice size of 0.003" would match the TH15 pressure, however the pressure is very sensitive to orifice diameter, and any erosion or tolerances in manufacturing will quickly drop the pressure.

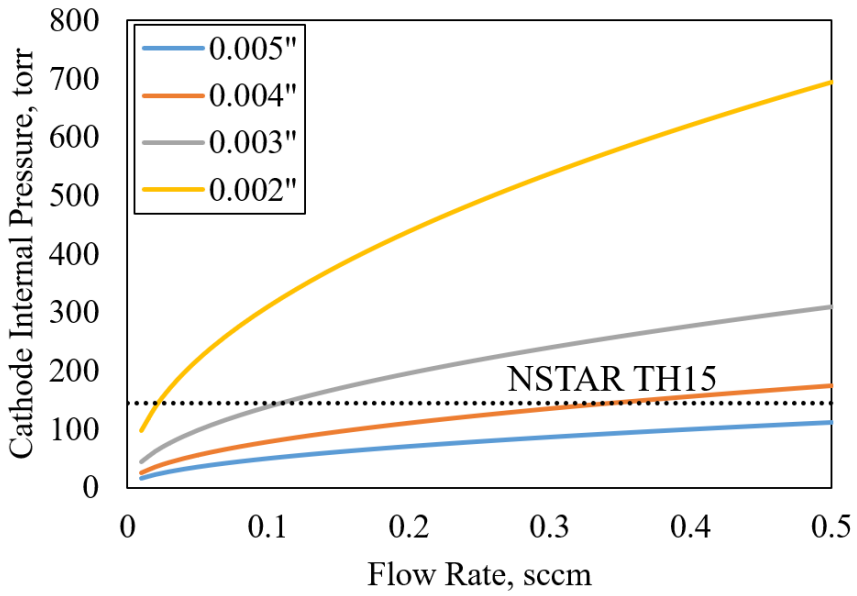

Figure 6.16: Insert pressure as a function of flow rate for a few different orifice diameters for small neutralizer cathode.

6.4.4 Development of Low-cost Test Cathodes

To experimentally test the trends elucidated in previous sections, a simple cathode was designed as a cheap vehicle for exploring variations in performance with cathode length, orifice size, heat wrap length, etc. A series of closed-end stainless steel tubes were manufactured to be used with small BaO inserts. The melting temperature of 304 stainless steel is around 1400 C, while the inserts were expected to operate around 1200 C. The cathode was set up with a high voltage power supply with a large ballast resistor to ignite and sustain the keeper discharge at a low current, with a lower voltage constant-current power supply in parallel for additional current control. This setup is shown in Figure 6.17. One cathode with a 0.008" ID x 0.025" L drilled orifice was successfully ignited but melted shut after being shut off approximately one minute later. Images of the cathode design and operation are shown in Figure 6.18. After several issues with ignition, a more traditional cathode design was pursued. Future low-cost cathodes of this type may be manufactured from tantalum (i.e. thermocouple protection tubes), but the more desirable molyrhenium requires advanced welding techniques to close one end off.

6.4.5 Development Efforts Towards an Improved MiXI cathode

An improved cathode was designed using the methodology laid out in previous sections. This cathode is designed to be readily disassembled to swap out the insert and keeper, however the orifice plate is welded on. The cathode is designed to test both heaterless and heatered ignition, different insert chemistries and geometries, and keeper geometries. The cathode, shown in Figure 6.19, is currently being manufactured by component suppliers.

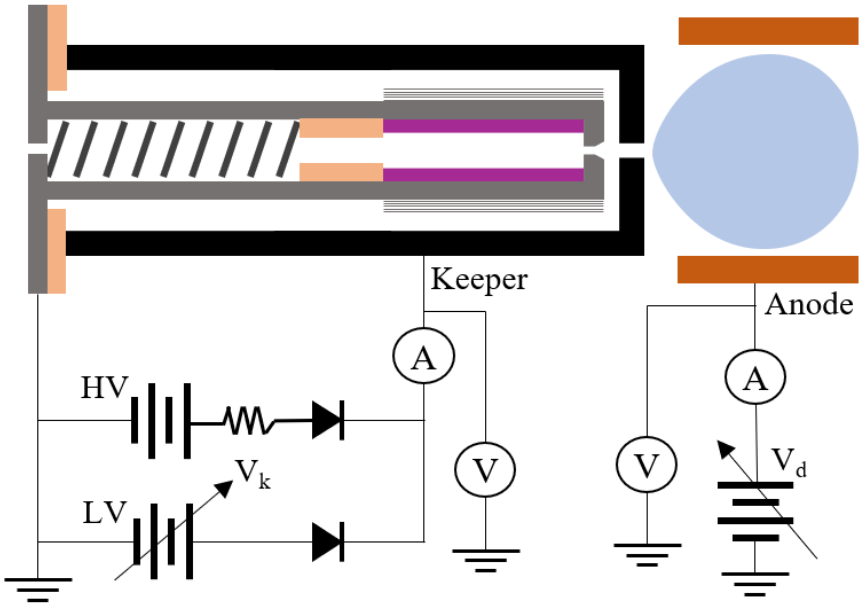

Figure 6.17: Electrical diagram for operating heaterless hollow cathodes.

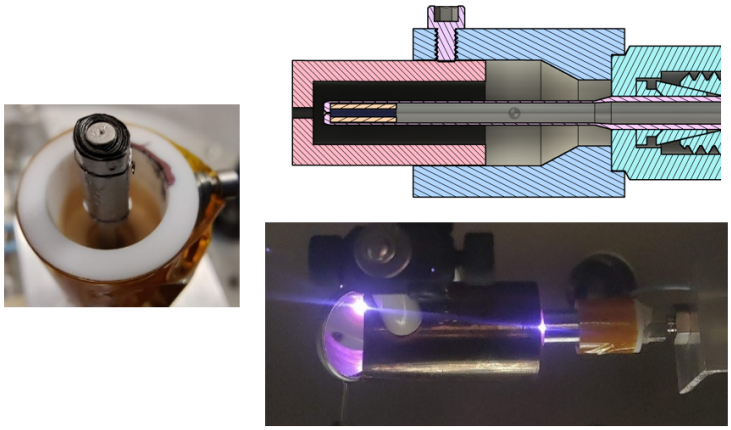

Figure 6.18: Left: Stainless steel cathode before ignition. Top right: CAD model of cathode. A BaO insert is crimped into a stainless closed-end tube and then swaged into a standard Swagelok fitting. Bottom right: Cathode operating in triode mode with a copper tube anode.

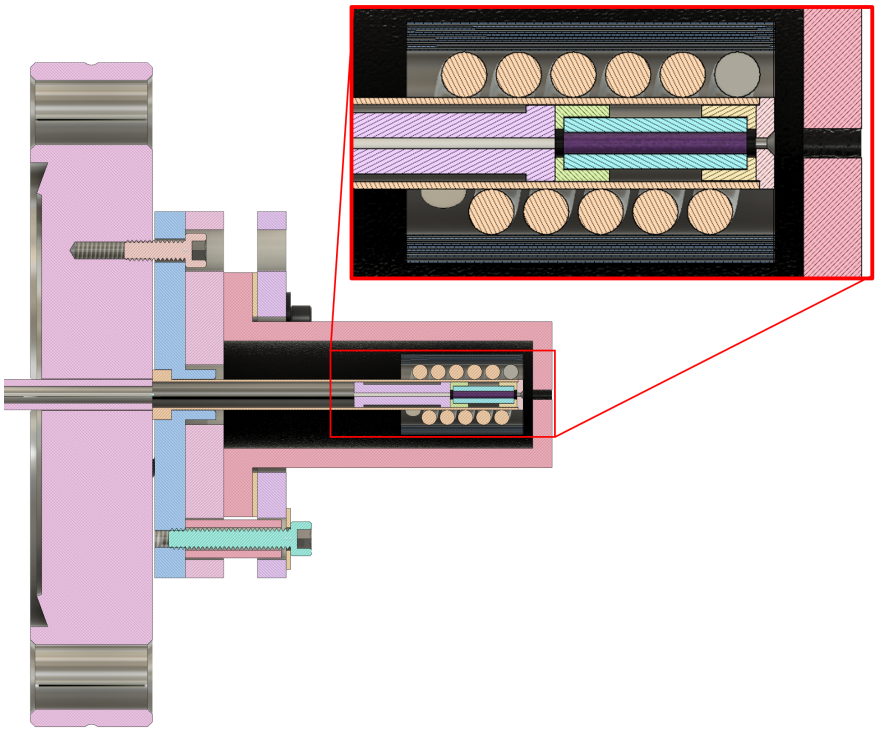

Figure 6.19: CAD design for a modular 1/8" LaB_6 cathode.

6.5 Conclusion

A miniature hollow cathode previously developed by Wirz were integrated with the MiXI(ARCH) configuration and characterized in a limited operating space with beam extraction. Data showed good performance, and points to further improvements with further characterization and cathode optimization. A small miniature BaO hollow cathode was also characterized in triode mode, which indicated that the cathode was capable of operating down to the 20 mA discharge current and 0.1 sccm flow required as a MiXI neutralizer, while requiring 15-20 W in combined keeper and heater power. A development effort was initiated to understand thermal loss mechanisms within these miniature hollow cathodes, and improve performance through new cathode designs. This effort culminated in the design for a small lab-model of a 1/8" LaB_6 cathode sized for MiXI operation.

CHAPTER 7

Summary, Conclusions, and Future Work

7.1 Summary of Conclusions

This body of work covers the first implementation of beam extraction for the MiXI(ARCH) thruster, characterization of the thruster with beam extraction, and analysis of the plume properties of the MiXI(ARCH) thruster via a comprehensive miniaturized plume diagnostics suite. This work also presents a physics-based computational model for understanding trends within the performance data for both MiXI(3-Ring) and MiXI(ARCH), investigates space mission performance for these thrusters, and characterizes and identifies pathways for improved performance for the MiXI thruster, in particular through identification of critical pathways towards high-efficiency miniature hollow cathode sources. The conclusions from this overall research effort identify and investigate promising performance trends and pathways towards improved thruster and mission performance particularly related to cathode design and operation as summarized in Sections 3.6, 4.5, 5.4, and 6.5. Following is a brief summary of these efforts and overarching conclusions.

Mission studies for a high impulse 6 U CubeSat showed that highly efficient, high I_{sp} micropropulsion such as MiXI enables a wealth of mission classes with ΔVs of multiple km/s and payloads up to several kg in a CubeSat formfactor. This study explored the relationship between mission capabilities (payload volume, craft wet mass, required burn duration) and important mission parameters such as payload mass, total required ΔV, and thruster properties. Conclusions from this study indicated that there are significant operational benefits

to having a MiXI throttle table consisting of both high I_{sp} and high thrust-to-power levels, and that mission performance is strongly affected by neutralizer cathode performance when MiXI is used for primary propulsion but less so for secondary propulsion applications where neutralizer duties can be shared across many thrusters.

In an effort to experimentally assess the performance of the thruster, the Axial Ring-Cusp Hybrid (ARCH) discharge was integrated into the MiXI thruster and characterized with beam extraction at 1 kV. Trends were assessed with input gas flow rate, anode temperature, discharge voltage, and discharge chamber aspect ratio. A non-ideal analytical control volume model of the discharge was developed and presented, which captured several global trends, although it did not fully capture trends which are believed to be caused by 3D effects. The model agreed with data from the present work as well as previous internal probing data of MiXI(ARCH), showed that the thruster is near the sweet-spot which balances stability with efficiency, and suggests that cathode performance, in the form of the cathode voltage drop, has a significant effect on thruster efficiency by reducing the primary electron energy. Control volume model and experimental results also agree with ideal thruster scaling relationships derived in this work, which dictate that peak thruster efficiency increases with the thruster current density. In conclusion, experimental characterization and analytical modeling has resulted in a better understanding of the internal physics within the MiXI thruster, as well as potential paths forward for further improving the plasma discharge performance, as discussed in Sections 3.6 and 4.5.

To more accurately characterize the expected in-flight thruster performance and ascertain the thrust correction factor for MiXI, a small plume diagnostics suite was developed to measure the current density, doubles ratio, and plasma potential within the plume. The Plasma Experiment SpatioTemporal Observation (PESTO) suite was developed and manufactured via analytical equations for predicting ExB probe performance along with computational modeling of the device with realistic geometry. Development goals included miniaturizing the device relative to commercial offerings while maintaining appropriate performance in

measuring plume properties and discriminating between ion populations. The probe was tested and verified by making measurements of the MiXI(ARCH) plume at one throttle point (with filament cathodes), which match analytical and computational predictions of probe performance. Conclusions from the results of the PESTO suite data collected in this study show that the MiXI plume has a negligible doubles population and a small beam divergence of around 5°. Additionally, the PESTO suite development and verification represents a new capability for future MiXI work, enabling rapid plume characterization of future thruster iterations.

A miniature BaO hollow cathode was integrated with the MiXI(ARCH) thruster as the discharge cathode, which was then characterized with beam extraction. Measurements showed good performance at the characterized operating point, and point to further improvements through further characterization and cathode optimization. One of a set of miniature hollow cathodes intended to be used with MiXI as a neutralizer cathode was also characterized to understand the typical minimum operating power needed for this cathode design. Thermal modeling agreed with data, and suggests that the bulk of power lost by the cathode is via conduction through the stem rather than radiation. Several candidate cathodes were designed via a combination of thermal and structural modeling to reduce this power requirement, and the simplest design was baselined due to its manufacturing simplicity and the only marginal improvements gained from greatly increasing complexity. Material choice as well as an accurate accounting of thermal loss paths were important to reduce cathode power requirement. Finally, LaB6 emitter lifetime and neutral flow modeling were used to fully design a simple cathode architecture for future experimentation and development. In conclusion, cathodes are critical components for DC ion thrusters, and this work builds further understanding of miniature cathode operation within the MiXI thruster, as well as of the important relationships between cathode properties and thruster (and the resulting mission) performance.

7.2 Future Work

This work has covered the integration and characterization of the ARCH discharge into the MiXI thruster, as well as preliminary thruster plume characterization and cathode design and operation. The overall goal of any thruster work is to develop an operational and flight-ready thruster which can be flown and operated in space. As such, there are several future efforts of technical development for the MiXI thruster ahead of a flight mission, the nearer term of which can be categorized into "Performance Enhancement" and "TRL Advancement", both of which are covered separately in the upcoming Sections 7.2.1 and 7.2.2, respectively.

7.2.1 Performance Enhancement

Performance enhancement includes improving the efficiency of the thruster to improve performance and operational flexibility, making the thruster more attractive and useful for a wide range of missions from the perspectives of key thruster metrics such as delivered ΔV and thrust range. There are several routes that have been identified which may increase the efficiency of the MiXI thruster. These include further improvements to the stability and efficiency of the discharge plasma, 7.2.1.1, and thermal performance improvements, 7.2.1.2, in particular for the discharge cathode.

7.2.1.1 Discharge Plasma Improvements

The control volume model detailed in Section 2.3 examined global plasma behavior as a function of operating parameters and design inputs. While this treatment elucidated plasma processes within the discharge which affect discharge loss and stability, little work was done to utilize this model as a design tool and optimize discharge performance or examine the available design space from a 0D view. The DC-ION code has also been used in the past to investigate the MiXI(ARCH) discharge, however there are several suggestions which came out of modeling which have not been experimentally verified or implemented [5].

As shown in Sec 4.4.2.1, the properties of the input primary electrons have a strong effect on the stability and efficiency of the thruster. The shape of the cathode plume may also have an effect, as identified by previous DC-ION modeling. Cathode effects on the plasma discharge is a topic ripe for investigation and have high impact on the overall understanding and performance of both MiXI discharge approaches, 3-Ring or ARCH. This can take place via examination of thruster operation, and investigating the relationship between thruster performance and cathode performance. Cathode performance may be altered for a hollow cathode by increasing or decreasing the total heat input into the cathode (via heater + keeper power) as detailed in the following section, or for a filament cathode by increasing and decreasing the discharge voltage. These provide control over the input primary electron population, such that the relationship between cathode and thruster performance may be improved. More basic investigations via internal plasma probing will also be fruitful and can explore a few different topics: primary electron population properties (the EEDF) and plasma properties (electron temperature, sheath potential) as a function of cathode performance, the difference in plasma structure between a filament and hollow cathode, and changes to the plasma structure with beam extraction. Therefore, along these lines, a combined experimental and computational (either 0D semi-analytical or 2D computational) investigation would help improve the understanding and performance of the plasma discharge.

7.2.1.2 Thermal Performance

Increased overall thruster temperature indicates unwanted power loss and decreases discharge and propellant efficiency by increasing the neutral gas temperature. As such, thermal losses into the thruster should be reduced, and paths must be designed for proper management of the thruster's thermal loads. The cathode performs better when heat is retained in the insert region and not lost to the discharge. Therefore, modification of thruster and cathode geometry and materials can be used to improve the thermal isolation of the cathode and heat

rejection of the thruster, which will improve performance by decreasing neutral temperature and decreasing the cathode voltage drop.

7.2.2 TRL Advancement

TRL advancement is the act of taking the current thruster and maturing it into a more flight-like model, fully characterized and able to withstand the rigors of launch and operation in space. In order for the thruster to be more ready for a flight mission, it must be matured through lab, engineering, and flight models which progressively enhance and characterize the design to be capable of surviving launch loads and operating for long periods in space with a known, regular performance. The next step in MiXI's development would be the development and characterization of an enhanced lab model with an integrated flight-like hollow cathode design. This will require the further development of the miniature hollow cathode detailed in Section 6.4 as a discharge and possibly neutralizer cathode, characterization of MiXI with the cathodes integrated, and then further improvement of the MiXI thruster head to improve repeatability and high voltage operation. TRL maturation of the thruster head and discharge cathode may occur independently from the neutralizer cathode. For mission applications where MiXI will be used in clusters for attitude control rather than primary propulsion, the performance of the neutralizer will be much less critical because a single, larger neutralizer cathode may be shared between thrusters. Sharing the neutralizer cathode across several thrusters will reduce efficiency impacts [64], and could allow for use of current COTS hollow cathodes. Previous characterization of MiXI(3-Ring) [72] demonstrated a small impulse bit of 1 μN·s via pulse-width modulation of the beam voltage, which lends itself to use as high precision attitude control. Such a capability is attractive for MiXI's use as secondary propulsion for attitude and formation control such as the previously proposed TPF-EMMA mission [6].

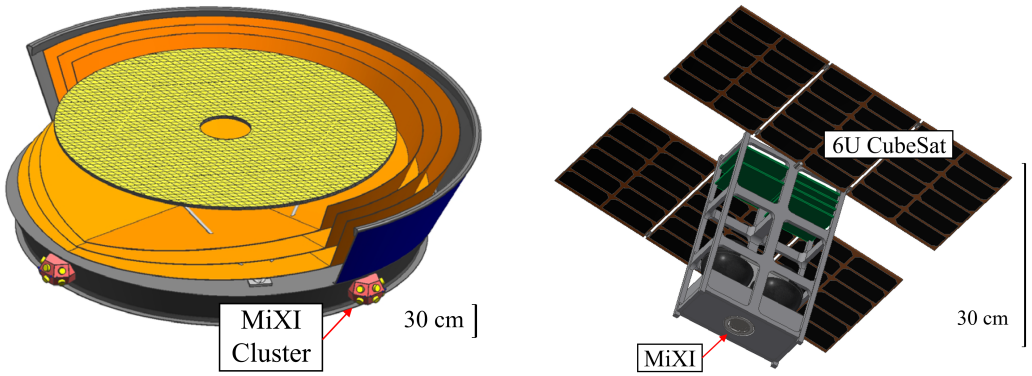

(a) Secondary Propulsion (b) Primary Propulsion

Figure 7.1: Example mission applications for MiXI: (a) secondary propulsion for high-precision attitude control and formation flying (e.g TPF-EMMA), and (b) primary propulsion for high ΔV CubeSat missions. (a) adapted from [6]

7.2.2.1 Cathode Development

Section 6 covers the basic design of a small hollow cathode along with initial efforts to operate a lower-cost cathode to validate model physics, however, the originally designed cathode needs to be fully manufactured and integrated with the thruster for full-up testing to advance the overall MiXI TRL via integrating hollow cathodes. For example, neutralizer and discharge cathodes could be designed, manufactured, and characterized based on Figure 6.19. The heater is considered to be the most common element to fail in a hollow cathode assembly, spurring development into heaterless hollow cathodes. Therefore, the mini cathode should consider heaterless ignition, which can be achieved in one of two ways: using a current-limited high voltage power supply at a fixed flow, or by using a current-limited fixed voltage keeper supply with a gas burp to ignite the cathode. With the former option, the cathode will likely require an elevated flow rate for ready ignition, necessitating a more complex flow system in the eventual space application. In the latter option, a fixed volume release system may be used to significantly simplify the system. [66, 73]

The current MiXI discharge cathode can operate in a 0.4 - 1 sccm flow, which is readily achievable by current cathodes, as shown in Sec. 6.2.3. The neutralizer cathode, however,

should reduce required flow to reduce the parasitic effect on the thruster. To determine this, the cathodes should be characterized for plume margin, i.e. the flow rate at which cathode oscillations begin as a function of discharge current.

Finally, the discharge voltage of a cathode gives a measure of the cathode's performance over its current extraction range. As such, the cathodes should be characterized with I-V curves as a function of flow, keeper current, and heater current, similarly to Fig 6.4(a).

In summary, it is recommended that the proposed cathodes should be manufactured and characterized with the following tests:

- Required ignition voltage as a function of fixed flow rate and keeper geometry
- Required gas pulse properties (peak flow, total mass, pressure, etc) to ignite the cathode as a function of keeper voltage and geometry
- Heater performance testing (thermionic emission as a function of heater power, and time)
- Plume margin as a function of discharge current
- I-V curves as a function of heater and keeper powers

7.2.2.2 MiXI Characterization

In this work, the MiXI thruster underwent only a preliminary characterization. Future work should include neutralizer integration with the thruster and characterization of the thruster in a "full-up" configuration, with hollow cathodes for both the discharge and neutralizer.

7.2.2.3 Hollow Cathode Performance

With hollow cathodes integrated as both the discharge cathode and the neutralizer cathode, the MiXI thruster should be characterized to determine stable operating points and perfor-

mance. The discharge loss curves should be measured at a variety of beam currents, and used to determine optimal operating points at various power levels. This can then be used to establish a throttle table for the thruster.

7.2.2.4 Plume Characterization

In Section 5, the PESTO probe was used to examine the MiXI(ARCH) plume at a single operating point and with filament cathodes. Hollow cathode integration into the discharge may change the internal plasma structure, resulting in an altered beam flatness and doubles ratio. In addition, a neutralizer hollow cathode will affect the neutralizer coupling voltage and plume structure. The thruster must then be characterized with the PESTO suite in the "full-up" configuration to determine the thrust correction factor and other plume properties over the newly established throttle table. If the beam current profile is significantly different than that assumed for the initial MiXI(3-Ring) grid design, additional calculations may be needed to assess grid lifetime and perveance limit. This and any further development of the grids may be performed with grid performance and life modeling. Once the grid lifetime has been computationally investigated, the model should be validated through a short wear test. The model can be used to predict the erosion pattern and magnitude after 1000 hours, and then a short wear test may be conducted and the resulting erosion quantified through profiliometry and compared to the model. If there is good agreement, then the model may be extrapolated to predict lifetime.

7.3 Overall Summary

In all, this work advances the state of MiXI development, explores the physics and underlying mechanisms driving miniature plasma discharge operation and scaling, builds tools and processes for future MiXI thruster efforts, and lays a path forward for improvement and maturation of the MiXI thruster. Through experimental and analytical investigations, discharge

analysis and modeling, and mission studies, this work shows that the MiXI thruster is an attractive propulsion option for high efficiency, high specific impulse micropropulsion.

Bibliography

[1] R. E. Wirz, "Discharge plasma processes of ring-cusp ion thrusters," Ph.D. Dissertation, Cal Tech, 2005.

[2] D. M. Goebel, "Ion source discharge performance and stability," *The Physics of Fluids*, vol. 25, no. 6, pp. 1093–1102, 1982, doi:10.1063/1.863842.

[3] D. M. Goebel, R. E. Wirz, and I. Katz, "Analytical ion thruster discharge performance model," *Journal of Propulsion and Power*, vol. 23, no. 5, pp. 1055–1067, 2007, doi:10.2514/1.26404.

[4] R. Wirz, J. Polk, C. Marrese, and J. Mueller, "Experimental and computational investigation of the performance of a micro-ion thruster," in *AIAA/ASME/SAE/ASEE Joint Propulsion Conference and Exhibit*, 2002, doi:10.2514/6.2002-3835.

[5] G. Z. Li, C. Huerta, and R. E. Wirz, "Computational modeling of an axial ring cusp hybrid discharge for the mixi thruster," in *AIAA/ASME/SAE/ASEE Joint Propulsion Conference and Exhibit*, 2018, p. 4814, doi:10.2514/6.2018-4814.

[6] S. R. Martin, D. Scharf, R. Wirz, O. Lay, D. McKinstry, B. Mennesson, G. Purcell, J. Rodriguez, L. Scherr, J. R. Smith *et al.*, "Tpf-emma: concept study of a planet finding space interferometer," in *Techniques and Instrumentation for Detection of Exoplanets III*, vol. 6693. International Society for Optics and Photonics, 2007, p. 669309.

[7] R. E. Wirz, J. E. Polk, C. M. Marrese, J. Mueller, J. Escobedo, and P. Sheehan, "Development and testing of a 3 cm electron bombardment micro-ion thruster," in *International Electric Propulsion Conference*, 2001.

[8] R. Wirz and I. Katz, "Plasma processes of dc ion thruster discharge chambers," in *AIAA/ASME/SAE/ASEE Joint Propulsion Conference and Exhibit*, 2005, p. 3690, doi:10.2514/6.2005-3690.

[9] R. Wirz and I. Katz, "A preliminary 2-d computational model of an ion thruster discharge chamber," in *AIAA/ASME/SAE/ASEE Joint Propulsion Conference and Exhibit*, 2003, p. 5163, doi:10.2514/6.2003-5163.

[10] R. Wirz and I. Katz, "2-d discharge chamber model for ion thrusters," in *AIAA/ ASME/SAE/ASEE Joint Propulsion Conference and Exhibit*, 2004, doi:10.2514/6.2004-4107.

[11] R. Wirz, "Computational modeling of a miniature ion thruster discharge," in *AIAA/ASME/SAE/ASEE Joint Propulsion Conference and Exhibit*, 2005, doi:10.2514/6.2005-3887.

[12] R. Wirz, R. Sullivan, J. Przybylowski, and M. Silva, "Hollow cathode and low-thrust extraction grid analysis for a miniature ion thruster," *International Journal of Plasma Science and Engineering*, vol. 2008, 2008, doi:10.1155/2008/693825.

[13] S. Araki and R. E. Wirz, "Magnetic field aligned mesh for ring-cusp discharge chambers," in *AIAA/ASME/SAE/ASEE Joint Propulsion Conference and Exhibit*, 2014, p. 3830, doi:10.2514/6.2014-3830.

[14] C. E. Huerta and R. E. Wirz, "Dc-ion model validation and convergence studies," in *AIAA/ASME/SAE/ASEE Joint Propulsion Conference and Exhibit*, 2018, p. 4813, doi:10.2514/6.2018-4813.

[15] H. R. Kaufman, "Technology of electron-bombardment ion thrusters," ser. Advances in Electronics and Electron Physics, L. Marton, Ed. Academic Press, 1975, vol. 36, pp. 265 – 373.

[16] R. Moore, "Magneto-electrostatically contained plasma ion thruster," in *7th International Electric Propulsion Conference*. American Institute of Aeronautics and Astronautics, 1969, Book Section.

[17] B. Dankongkakul and R. E. Wirz, "Axial ring-cusp hybrid (arch) plasma discharge: an approach to highly efficient miniature-scale ion sources," *Plasma Sources Science and Technology*, vol. 27, no. 12, p. 125001, 2018, doi:10.1088/1361-6595/aae63c.

[18] M. T. Domonkos, "Evaluation of low-current orificed hollow cathodes," Ph.D. dissertation, University of Michigan, 1999.

[19] P. Puchkov, "The low-current cathode for a small power electric propulsion," in *7th European Conference for Aeronautics and Space Sciences*, 07 2017, doi:10.13009/EUCASS2017-138.

[20] G. Becatti, R. W. Conversano, and D. M. Goebel, "Demonstration of 25,000 ignitions on a proto-flight compact heaterless lanthanum hexaboride hollow cathode," *Acta Astronautica*, vol. 178, pp. 181–191, 2021. [Online]. Available: https://www.sciencedirect.com/science/article/pii/S0094576520305543

[21] D. Pedrini, C. Ducci, U. Cesari, T. Misuri, and M. Andrenucci, "Sitael hc1 low-current hollow cathode," *Aerospace*, vol. 7, no. 7, 2020. [Online]. Available: https://www.mdpi.com/2226-4310/7/7/96

[22] D. M. Goebel and I. Katz, *Fundamentals of Electric Propulsion: Ion and Hall Thrusters*, ser. JPL Space Science and Technology Series. John Wiley & Sons, nov 2008.

[23] B. Dankongkakul and R. E. Wirz, "Miniature ion thruster ring-cusp discharge performance and behavior," *Journal of Applied Physics*, vol. 122, no. 24, p. 243303, 2017, doi:10.1063/1.4995638.

[24] A. Sengupta, "Magnetic confinement in a ring-cusp ion thruster discharge plasma," *Journal of Applied Physics*, vol. 105, no. 9, p. 093303, 2009.

[25] L. Spitzer, *Physics of Fully Ionized Gases*, ser. Interscience tracts on physics

and astronomy, 3. Interscience Publishers, 1956. [Online]. Available: https://books.google.com/books?id=Cb8EAAAAMAAJ

[26] D. Rapp and P. Englander-Golden, "Total cross sections for ionization and attachment in gases by electron impact. i. positive ionization," *The Journal of Chemical Physics*, vol. 43, no. 5, pp. 1464–1479, 1965, doi:10.1063/1.1696957.

[27] W. Wien, "Untersuchungen uber die elektrische entladung in verdunnten gasen," *Annalen der Physik*, vol. 313, no. 6, pp. 244–266, 1902.

[28] H. Heidt, J. Puig-Suari, A. Moore, S. Nakasuka, and R. Twiggs, "Cubesat: A new generation of picosatellite for education and industry low-cost space experimentation," in *14th Annual USU Conference on Small Satellites*, 2000.

[29] NASA CubeSat Launch Initiative, "Cubesat 101: Basic concepts and processes for first-time cubesat developers," *San Luis Obispo, USA*, 2017.

[30] C. P. S. The CubeSat Program, "Cubesat design specification, rev. 13," 2014.

[31] L. Johnson, B. Cohen, L. McNutt, and J. Castillo-Rogez, "Nea scout and lunar flashlight: two near-term interplanetary solar sail missions," 2015.

[32] C. Boshuizen, J. Mason, P. Klupar, and S. Spanhake, "Results from the planet labs flock constellation," 2014.

[33] A. Poghosyan and A. Golkar, "Cubesat evolution: Analyzing cubesat capabilities for conducting science missions," *Progress in Aerospace Sciences*, vol. 88, pp. 59–83, 2017.

[34] G. Mingotti, F. Topputo, and F. Bernelli-Zazzera, "Efficient invariant-manifold, low-thrust planar trajectories to the moon," *Communications in Nonlinear Science and Numerical Simulation*, vol. 17, no. 2, pp. 817–831, 2012.

[35] C. Russell and C. Raymond, "The dawn mission to vesta and ceres," in *The Dawn Mission to Minor Planets 4 Vesta and 1 Ceres*. Springer, 2011, pp. 3–23.

[36] R. Wirz, J. Mueller, M. Gale, and C. Marrese, "Miniature ion thruster for precision formation flying," in *AIAA/ASME/SAE/ASEE Joint Propulsion Conference and Exhibit*, 2004, p. 4115, doi:10.2514/6.2004-4115.

[37] R. W. Conversano and R. E. Wirz, "Mission capability assessment of cubesats using a miniature ion thruster," *Journal of Spacecraft and Rockets*, vol. 50, no. 5, pp. 1035–1046, 2013, doi:10.2514/1.A32435.

[38] W. J. Larson and J. R. Wertz, "Space mission analysis and design," Torrance, CA (United States); Microcosm, Inc., Tech. Rep., 1992.

[39] J. Sheehan, T. A. Collard, F. H. Ebersohn, and B. W. Longmier, "Initial operation of the cubesat ambipolar thruster," in *2015 IEEE International Conference on Plasma Sciences (ICOPS)*, 2015, doi:10.1109/PLASMA.2015.7179981.

[40] M. M. E.W. Lemmon and D. Friend, *NIST Chemistry WebBook, NIST Standard Reference Database Number 69*. Gaithersburg MD, 20899: National Institute of Standards and Technology, ch. Thermophysical Properties of Fluid Systems.

[41] NASA Small Spacecraft Systems Virtual Institute. (2018) State of the art of small spacecraft technology: Propulsion. [Online]. Available: https://sst-soa.arc.nasa.gov/04-propulsion

[42] P. Clark, B. Malphrus, D. Reuter, R. MacDowall, D. Folta, T. Hurford, C. Brambora, and W. Farrell, "Lunar ice cube: Birches payload and the search for volatiles with a first generation deep space cubesat," 2016.

[43] S. Samples, G. Z. Li, and R. E. Wirz, "Performance testing and development of the mixi thruster with the arch discharge," in *AIAA/ASME/SAE/ASEE Joint Propulsion Conference and Exhibit*, ser. AIAA Propulsion and Energy Forum. American Institute of Aeronautics and Astronautics, 2018, Book Section, doi:10.2514/6.2018-4648.

[44] T. Collard, J. Sheehan, and A. Gallimore, "Pressurized xenon propellant management system for the cubesat ambipolar thruster," 07 2015.

[45] MMA Design, *eHawk Solar Array*, http://mmadesignllc.com/products/ehawk-solar-array/ (Accessed April 20, 2018).

[46] Innovative Solutions in Space, *6-Unit CubeSat Structure*, https://www.isispace.nl/product/6-unit-cubesat-structure/ (Accessed April 20, 2018).

[47] Honeybee Robotics Spacecraft Mechanisms Corporation, *Honeybee Robotics CubeSat SADA*, https://www.honeybeerobotics.com/wp-content/uploads/2013/12/Honeybee-Robotics-CubeSat-SADA.pdf/ (Accessed September 20, 2018).

[48] Innovative Solutions in Space, *VHF downlink/UHF uplink full duplex transceiver - ISIS*, https://www.isispace.nl/product/vhf-downlink-uhf-uplink-full-duplex-transceiver/ (Accessed April 20, 2018).

[49] Innovative Solutions in Space, *ISIS On Board Computer*, https://www.isispace.nl/product/on-board-computer/(Accessed April 20, 2018).

[50] T. Tsuru, S. Kondo, N. Yamamoto, and H. Nakashima, "Development of miniature microwave discharge neutralizer for miniature ion thruster," *Transactions of the Japan Society for Aeronautical and Space Sciences, Space Technology Japan*, vol. 7, no. 26, pp. 163–167, 2009.

[51] W. Kerslake, "Preliminary operation of oxide-coated brush cathodes in electron-bombardment ion thrustors," National Aeronautics and Space Administration, Cleveland, Ohio. Lewis Research Center, Tech. Rep., 1965.

[52] B. Dankongkakul and R. E. Wirz, "Axial ring-cusp hybrid (arch) plasma discharge: an

approach to highly efficient miniature-scale ion sources," *Plasma Sources Science and Technology*, vol. 27, no. 12, p. 125001, 2018.

[53] G. Li, C. Huerta, and R. Wirz, "Computational modeling of an axial ring cusp hybrid discharge for the mixi thruster," in *AIAA/ASME/SAE/ASEE Joint Propulsion Conference and Exhibit*. American Institute of Aeronautics and Astronautics, 2018, Book Section.

[54] J. Brophy, "Simulated ion thruster operation without beam extraction," in *21st International Electric Propulsion Conference*, 1990, p. 2655.

[55] C. E. Huerta and R. E. Wirz, *DC-Ion Model Validation and Convergence Studies*, ser. AIAA/ASME/SAE/ASEE Joint Propulsion Conference and Exhibit, 2018, doi:10.2514/6.2018-4813.

[56] D. Goebel, I. Katz, R. Watkins, and K. Jameson, *Hollow Cathode and Keeper-Region Plasma Measurements Using Ultra-Fast Miniature Scanning Probes*.

[57] K. Jameson, D. Goebel, and R. Watkins, *Hollow Cathode and Keeper-Region Plasma Measurements*, 10.2514/6.2005-3667.

[58] A. Simon, "Ambipolar diffusion in a magnetic field," *Phys. Rev.*, vol. 98, pp. 317–318, Apr 1955.

[59] J. Pollard, K. Diamant, M. Crofton, M. Patterson, and G. Soulas, "Spatially-resolved beam current and charge-state distributions for the next ion engine," in *AIAA/ASME/SAE/ASEE Joint Propulsion Conference*, 2010, p. 6779.

[60] M. Patino, "Plasma inter-particle and particle-wall interactions," Ph.D. Dissertation, University of California, Los Angeles, 2017.

[61] B. Dankongkakul and R. E. Wirz, "Design of miniature ring-cusp ion thrusters via analysis of discharge eedf and plasma parameter mapping," in *AIAA/ASME/SAE/ASEE Joint Propulsion Conference and Exhibit*, 2016, p. 4545.

[62] H.-S. Mao, R. E. Wirz, and D. M. Goebel, "Plasma structure of miniature ring-cusp ion thruster discharges," *Journal of Propulsion and Power*, vol. 30, no. 3, pp. 628–636, 2014. [Online]. Available: https://doi.org/10.2514/1.B34759

[63] R. Wirz, M. Gamero-Castano, and D. Goebel, "Pulsed operation of an ion accelerator," *NASA Tech Briefs*, p. 3546, 2009. [Online]. Available: https://www.techbriefs.com/component/content/article/tb/pub/techbriefs/physical-sciences/3546

[64] R. Wirz, "Low-contamination high-precision thruster for precision formation flying missions," *Internal JPL Report for Task*, vol. 6, p. 065, 2006.

[65] J. R. Brophy, J. E. Polk, and D. M. Goebel, "Development of a 50,000-s, lithium-fueled, gridded ion thruster," in *International Electric Propulsion Conference*, 2017.

[66] G. Becatti, D. M. Goebel, J. E. Polk, and P. Guerrero, "Life evaluation of a lanthanum hexaboride hollow cathode for high-power hall thruster," *Journal of Propulsion and Power*, vol. 34, no. 4, pp. 893–900, 2018. [Online]. Available: https://doi.org/10.2514/1.B36659

[67] D. M. Goebel, R. M. Watkins, and K. K. Jameson, "Lab6 hollow cathodes for ion and hall thrusters," *Journal of Propulsion and Power*, vol. 23, no. 3, pp. 552–558, 2007. [Online]. Available: https://doi.org/10.2514/1.25475

[68] D. L. Jacobson and E. K. Storms, "Work function measurement of lanthanum - boron compounds," *IEEE Transactions on Plasma Science*, vol. 6, no. 2, pp. 191–199, 1978.

[69] J. M. Lafferty, "Boride cathodes," *Journal of Applied Physics*, vol. 22, no. 3, pp. 299–309, 1951. [Online]. Available: https://doi.org/10.1063/1.1699946

[70] C. J. Wordingham, P.-Y. Taunay, and E. Choueiri, *A Critical Review of Orificed Hollow Cathode Modeling: 0D Models*, 2017. [Online]. Available: https://arc.aiaa.org/doi/abs/10.2514/6.2017-4888

[71] J. Polk, J. Anderson, J. Brophy, V. Rawlin, M. Patterson, J. Sovey, and J. Hamley, *An overview of the results from an 8200 hour wear test of the NSTAR ion thruster*, 1999. [Online]. Available: https://arc.aiaa.org/doi/abs/10.2514/6.1999-2446

[72] R. Wirz, M. Gamero, and D. Goebel, "Pulsed operation of an ion accelerator," NASA Tech Brief, Tech. Rep. NPO44961, Feb 2009.

[73] R. Ham, J. D. Williams, S. J. Hall, G. F. Benavides, and T. R. Verhey, "Characterization of a fixed-volume release system for initiating an arc discharge in a heaterless hollow cathode," in *2019 International Electric Propulsion Conference*, 2019.